

Laser texturing of glass substrates for light in-coupling
in silicon thin-film solar cells

Von der Fakultät für Mathematik und Naturwissenschaften
der Carl von Ossietzky Universität Oldenburg zur Erlangung
des Grades und Titels eines Doktors der Naturwissenschaften
(Dr. rer. nat.)

angenommene Dissertation

von Frau Kambulakwao Chakanga

geboren am 16.04.1983 in Ndola, Sambia

Erstgutachter: Prof. Dr. Carsten Agert
Zweitgutachter: Prof. Dr. Ulrich Teubner
Drittgutachter: Prof. Dr. Jürgen Parisi
Tag der Disputation: 8.12.2015

„It always seems impossible until it's done.“

[Nelson Mandela]

Abstract

Direct picosecond laser-textured glass substrates were investigated for the application in thin-film solar cells. Commercially available aluminoborosilicate glass with alkali (Type I), earth alkali (Type II) and soda-lime (Type III) glass substrates were textured with varying scribing speed and pulse energy. The results showed that the electronic properties of the reference glass substrates influenced the dimensions of the ablated crater. The diameter of the ablated isolated crater decreased with decreasing pulse energy. Decreasing the scribing speed changed the texture from periodic to random.

Highly textured substrates showed broadband light scattering in the UV and NIR region, which reduced the transmission due to the increased surface multi-reflections and absorption. The refractive index of periodically textured Type I and III glass substrates increased and Type II decreased following ablation. Numerical modelling suggested that the refractive index change was higher in highly textured substrates in comparison to periodically textured substrates. Great refractive index change ($\Delta n > 0.05$) increased the reflection at the glass/AZO interface whereas the reduced refractive index change showed a greater impact on the reflection than the increased refractive index.

Raman analysis suggested that the variation in the three- and four-fold rings or Si-O-S linkages in Type II were responsible for the changed refractive index. Elevation and red-shift of the low-frequency region of the Boson peak of highly textured substrates indicated that further physical and structural properties of the glass substrates deteriorated following ablation at low scribing speeds. Furthermore, annealing the highly textured glass substrates at 150-450°C reduced the structural modifications.

The changed glass surface morphology altered the substrate-film interface energy, mismatch and hence AZO growth. The step coverage on rounded textures improved and was assumed to contribute the most to the decreased resistivity, increased charge carrier concentration and Hall mobility observed in AZO films in comparison to reference and highly textured substrates. The amorphous content in the AZO films increased with rising glass texture and assumed to be responsible for the increased band gap. The strain in the films on periodically textured substrates decreased and improved the crystallinity, which possibly reduced the band gap.

The performance of unoptimised solar cells on laser-textured glass (table 6.1) was partly comparable to optimized solar cells reported in literature (table 2.2). Optimizing the deposition conditions for textured substrates is hence expected to improve the solar cell performance significantly. Simulation results showed that reduced TCO thickness to the identified optimal 50 nm reduced parasitic absorption significantly while increasing antireflection behaviour $\lambda < 600$ nm. State of the art ultra-thin solar cells with 50 nm TCO and 150 nm i-aSi:H on highly textured substrates demonstrated a superior performance with the highest J_{ph} (12.5 mA/cm²) in comparison to both the flat and textured reference (table 7.1).

Zusammenfassung

Aluminoborosilikatglas mit Alkali (Typ I), Erdalkali (Typ II) und Natronkalkglas (Typ III) wurden mit einem gepulsten Picosekundenlaser strukturiert und für die Anwendung in Dünnschicht-Solarzellen untersucht. Die Ergebnisse zeigen, dass die elektronischen Eigenschaften der Referenzsubstrate die Dimensionen der ablatierten Krater beeinflusst. Der Durchmesser der Krater und die Periodizität der Oberflächenstruktur nehmen mit abnehmender Pulsenergie bzw. Schreibgeschwindigkeit ab.

Stark strukturierte Substrate zeigen eine breitbandige Streuung im UV und NIR Spektralbereich. Die Mehrfachreflexionen auf der Oberfläche reduzieren die Transmission und erhöhen die Absorption. Periodisch strukturierte Typ I und III zeigen eine erhöhte und Typ II Substrate einen verringerten Brechungsindex im Vergleich zur Referenz. Numerische Modellierungen zeigen, dass die Brechungsindexänderung im Vergleich in stark strukturierten Substraten höher ist als in periodisch strukturierten Substraten. Die Brechungsindexänderung ($\Delta n > 0.05$) erhöht die Reflexion an der Glas/AZO Grenzfläche, wobei ein reduzierter Brechungsindex einen größeren Einfluss hat.

Die Raman Ergebnisse zeigen, dass die Umstrukturierung der Drei- und Vierfachringe oder Si-O-S-Bindungen in Typ II für den geänderten Brechungsindex verantwortlich sind. Eine starke Ablation verursacht eine Erhöhung und Rotverschiebung im Niederfrequenzbereich des Bosonenpeaks, die wiederum ein Hinweis auf einer Verschlechterung der physikalischen und strukturellen Eigenschaften der Glassubstrate ist. Eine Temperaturbehandlung der stark strukturierten Glassubstrate bei 150-450°C verringerte die strukturellen Änderungen.

Die veränderte Glasoberflächenmorphologie ändert außerdem die Glas/AZO Grenzflächenenergie, und damit die Fehlanpassung und das Wachstum der AZO Schichten. Die verbesserte Konformität der Schichten auf gerundeten Texturen ist wahrscheinlich für die verbesserten elektrischen und strukturellen Eigenschaften der AZO Schichten verantwortlich. Der amorphe Gehalt in den Schichten steigt mit der Glassubstratraugigkeit und könnte für die erhöhte Bandlücke verantwortlich sein. Die Schichtspannung auf periodisch strukturierten Substraten ist vermutlich geringer, verbessert die Kristallinität und reduziert möglicherweise die Bandlücke des AZOs.

Die Leistung von unoptimierten Solarzellen auf laser-strukturierten Glassubstraten (Tabelle 2.2) sind zum Teil vergleichbar mit optimierten Solarzellen aus der Literatur (Tabelle 6.1). Es ist daher zu erwarten, dass das Optimieren der Abscheidungsbedingungen für strukturierte Substrate die Leistung der Solarzellenzelle erheblich verbessern wird. Die Simulationsergebnisse zeigen, dass ein reduzierte TCO-Dicke auf 50 nm die parasitäre Absorption signifikant reduziert, während das Antireflexionsverhalten für $\lambda < 600$ nm zunimmt. Ultradünne Solarzellen mit 50 nm TCO und 150 nm i-aSi:H auf strukturierten Substraten zeigen eine hervorragende Leistung mit dem höchsten J_{ph} (12.5 mA/cm^2) im Vergleich zur flachen und strukturierten Referenz (Tabelle 7.1).

Contents

1	Introduction	1
2	Literature review	5
2.1	Silicon thin-film solar cells	5
2.2	Light management	6
2.2.1	Textured TCO substrates	8
2.2.2	Textured glass substrates	8
2.2.3	Highly conducting ultra-thin <200 nm electrodes	10
2.3	Aim and scope	12
3	Experimental details	14
3.1	Sample preparation	14
3.2	Surface morphology	15
3.3	Optical properties	18
3.4	Raman optical properties	20
3.5	Microstructure properties	22
3.5.1	X-Ray Diffraction (XRD) Analysis	22
3.5.2	Williamson-Hall Method	24
3.6	EQE and J-V characteristics	28
4	Glass substrates	30
4.1	Laser texturing of glass substrates	30
4.1.1	Glass structure and properties	30
4.1.2	Laser and dielectric material interaction	32
4.1.3	Surface topology	33
4.1.4	UV-VIS optical properties	41
4.2	Simulation of refractive index variation	44
4.2.1	Simulation domain	44
4.2.2	Optical generation rate profile	46
4.2.3	Simulated reflection	47
4.3	Raman optical properties	49
4.3.1	Band interpretation	49
4.3.2	Pulse energy variation	53
4.3.3	Scribing speed variation	54
4.3.4	Annealing effect	56
5	Aluminium doped zinc oxide	60
5.1	Thin-film growth	60
5.2	Microstructure	64

5.2.1	Grain properties and Strain	65
5.2.2	Impurities and defects in the crystal	66
5.2.3	Lattice and thermal expansion mismatch	68
5.3	Electrical properties	69
5.3.1	Charge carrier concentration and hall mobility	70
5.3.2	Scattering mechanisms	71
5.3.3	Step-coverage	72
5.4	Optical properties	75
6	Silicon thin-film solar cells	78
6.1	Thin-film solar cells	78
6.2	pin aSi:H solar cells	79
6.3	nip aSi:H bifacial solar cells	82
6.4	pin aSi:H / μ cSi:H tandem solar cells	84
7	Optimisation of TCO in pin aSi:H	89
7.1	Numerical Modelling	89
7.1.1	Simulation domain	89
7.1.2	Simulated output	90
7.1.3	Simulation variables	90
7.2	Results and Discussion	91
7.2.1	Textured glass substrate	92
7.2.2	Light scattering	95
7.2.3	Modified glass texture	96
8	Summary and Outlook	99
	References	101
	List of Publications	I
	Acknowledgements	V
	Erklärung	VII
	Curriculum Vitae	IX

1 Introduction

The current world population of 7.2 billion is predicted to increase to 9.6 billion in 2050 [1]. Great challenges are posed by the high energy demand per capita, particularly in Organization for Economic Cooperation and Development (OECD) nations and the strong economic growth of non-OECD nations. The energy consumption is projected to grow by 56% between 2010 and 2040 [1]. Currently, the demand is quenched by almost 80% with fossil fuels [2] which are rapidly depleting. Most importantly, greenhouse gas emissions such as carbon dioxide (CO_2) from fossil fuel combustion have severe environmental impacts. Renewable energy sources and lower energy lifestyles are thus inevitable to mitigate climate changes for a sustainable future.

The most important renewable energies are hydro, wind and photovoltaic (PV) [3]. The PV market is dominated by silicon wafer-based modules with a 90% share and efficiencies as high as 25% for crystalline solar cells [4]. The other 10% belong to thin-film solar cells [5], some based on perovskite [6] which have gained great interest due to the recently developed lead-free manufacturing method [7] and efficiencies around 14% [4]. Cadmium telluride (CdTe) solar cells with efficiencies about 19.6% [4] have also gained attention due to the recent progress in replacing the cadmium chloride (CdCl_2) used in the doping process with a water-soluble, non-toxic and low-cost magnesium chloride MgCl_2 [8] salt also used in Tofu production, thus giving the technology its nickname „Tofu solar cells“ in the media. For these technologies to compete with conventional methods, further reduction in costs and increase in efficiencies is still necessary.

Silicon-based thin-film technology has the potential for low-cost, rapid large-area industrial production and low energy-payback time [9]. The abundance of the raw material silicon and less material required than for conventional wafer silicon solar cells rank among the major advantages of the technology. Examples of silicon thin-film solar cells include hydrogenated amorphous (aSi:H) and microcrystalline ($\mu\text{cSi:H}$) single and multi-junction solar cells. Current solar cell efficiencies are 10.1% for single junction aSi:H in the superstrate configuration (pin) [10], 10.8% for single junction pin $\mu\text{cSi:H}$ [11] and 12.3% for the multi-junction tandem aSi:H/ $\mu\text{cSi:H}$ (micromorph) [4].

One method used to increase the conversion efficiencies in these solar cells is the use of textured interfaces. The incident light is diffuse-scattered into the solar cell to increase internal multi-reflections and the effective optical path [12]. The solar cell absorption is increased and the required effective absorber thickness reduced. This concept of light incoupling is an advantage to reduce production costs. For amorphous silicon thin-film solar cells, thinner absorber layers are also important to decrease the light-induced degradation [13].

Light management is required for spectral regions where the absorber layers have a low absorption coefficient. This is commonly achieved by randomly textured transparent conductive oxide (TCO) [12]. Broadband light scattering is enhanced by double-textures, a superposition of larger and smaller lateral features to increase the scattered spectral range [14]. This can for example be achieved by texturing glass substrates [15] with high lateral dimensions and coating it a TCO ($\approx 1 \mu\text{m}$), which is subsequently textured to obtain a finer texture [16, 17]. One disadvantage of this approach is that the parasitic absorption of the relatively thick TCO film is enhanced.

Alternatively light in-coupling is achieved by introducing an appropriately textured glass surface [18]. One major advantage is that ultra-thin and untexturable electrodes can and must be used to avoid front contact parasitic absorption. However, the reduced TCO thickness influences the optoelectronic properties conversely. Studies demonstrate that optimised TCOs, such hydrogenated indium oxide (IOH), show promise for this application [17]. Alternative electrodes with new and upcoming materials such graphene, a 2D carbon material [19] embedded in amorphous or polycrystalline transparent semiconductor, such as zinc oxide (ZnO), can be investigated for this application. The technological advancements demonstrate that applicable ultra-thin electrodes are available. However, a simple method of effectively texturing the glass surface is still necessary.

The methods used to texture the glass substrates include wet-chemical etching with highly corrosive acids, such as hydrofluoric acid (HF) [16], reactive ion etching (RIE) [20] and lithography [17] using indirect laser patterning [21, 22]. The disadvantages of these methods include the complexity, required resources and toxic waste that requires disposal. From this point of view, direct laser ablation using either single or multi-laser pulse shots to remove material from the substrate surface [23, 24] is a simpler and appealing alternative. Nanosecond laser technology already finds application in thin-film solar cells for the monolithic connecting into modules [25].

Using a picosecond laser for texturing substrates could allow an integration of the texturing step into production line. This could be achieved by integrating ps optics in the system. Given the very-efficient and fast-laser technology, this approach promises to reduce the required time for external substrate processing, toxic waste disposal and thus an added benefit in production efficiency. However, several aspects have to be taken into consideration. The quality of the texture depends on both the target material and the laser parameters. Topological variations following ablation are accompanied by structural modifications, defects or micro-cracks formation. These can have a detrimental impact on the front contact and solar cells stability and performance.

The aim of this work is to investigate the potential of picosecond (ps) laser-textured glass substrates for light management in thin-film solar cells. For this purpose, the morphological changes of the glass substrates following ablation with varying pulse energy and scribing speed were systematically studied. Aluminium doped zinc oxide (AZO)

was deposited on the differently textured glass substrates and the optoelectronic and structural properties were analysed. Finally, single junction pin and nip solar cells and multi-junction solar cells were deposited on the differently textured substrates. The thesis is structured as follows:

1. **Literature review** The principle of thin-film silicon solar cells is shortly outlined to introduce the investigated single junction substrate and superstrate and multi-junction configuration. The essential aim of light in-coupling is discussed with a literature overview of current efficiencies. The scientific advances regarding textured glass substrates for light in-coupling are reviewed to emphasise the contribution of this study.
2. **Experimental details** Characterisation techniques used to quantify the performance of the solar cells are presented. The methods of determining the topology and morphology of textured substrates and the optoelectronic properties of films are outlined. The angular resolved intensity (ADI) measurement technique and data processing used to assess the light scattering capabilities of the textured substrates is described to allow a better understanding and comparison with simulated results.
3. **Glass substrates**
 - (a) **Experiment: Laser texturing of glass substrates** Picosecond laser texturing of multi-component glass is studied. The underlying physics of the interaction between the short-pulsed laser and dielectric material is briefly outlined. The topologies are statistically evaluated to assess the potential for the application in thin-film solar cells configurations. In addition, the optical properties of the substrates are discussed.
 - (b) **Simulation: Refractive index variation** The extent of the refractive index change observed in periodically textured substrates is discussed. Limited characterisation possibilities for optically rough substrates were compensated for numerical modelling. The results are discussed to provide better comprehension of how the hypothetically high refractive index change influences the solar cell performance.
 - (c) **Experiment: Raman optical properties** The structural modifications in the differently textured glass substructures are interpreted from Raman measurements. The analysis aims to identify the structural units most affected by laser texturing. Annealing is studied as a possible method of reducing and reversing the structural modification and the results are presented.
4. **Experiment: Aluminium doped zinc oxide** The optoelectronic and microstructure properties of AZO films deposited on laser-textured glass substrates are dis-

cussed. First, the theoretical growth models are outlined for a better understanding of how the surface texture and chemistry influence thin-film growth.

5. **Experiment: Silicon thin-film solar cells** The performance of pin, nip and tandem solar cells deposited on AZO coated textured substrates are shown. The influence of the differently textured glass substrates on the solar cells performance is outlined.
6. **Simulation: Optimisation of TCO in pin aSi:H** The optimisation of TCO and solar cell deposition are out of scope of this study. Numerical modelling is therefore used as a tool to demonstrate the potential of reducing the TCO thickness. The performance of ultra-thin pin aSi:H solar cells on highly textured glass substrates is illustrated.
7. **Summary and outlook** Finally, the main aspects covered and the results of the thesis are summarized, concluding with the achieved contribution to the scientific community.

2 Literature review

Single junction and multi-junction silicon thin-film solar cells are introduced. The principle of the pin structure is shortly outlined to show how optoelectronic properties of the TCO influence the solar cell operation. The essential aim of light in-coupling and its impact on the solar cells performance are elaborated. Also a literature overview of state-of-the-art of thin-film solar cells efficiencies is given with respect to textured glass substrates and the aim and scope of this study are emphasised.

2.1 Silicon thin-film solar cells

Amorphous silicon (aSi) has a short-range order with a high defect density due to dangling bonds. These act as recombination centres and impend the charge carrier transportation [26]. The high defect density limits the application of aSi as a functional absorber layer in solar cells. This is a negative effect from the perspective of solar cell application and compensated by incorporating hydrogen (aSi:H). Hydrogen passivates the dangling bonds. Increasing the hydrogen content during deposition leads to the transition of the amorphous material to microcrystalline (μ cSi:H) material with long-range order [26].

Optical and electrical properties of aSi:H and μ cSi:H are different. The band gap E_g of aSi:H is ≈ 1.7 eV and is considerably higher than that of μ cSi:H ≈ 1.1 eV [26, 27]. aSi:H thus absorbs light in the UV-VIS range and μ cSi:H in the near infrared (NIR) spectrum. The combination of single junction solar cells to form multi-junction micromorph solar cells is thus advantageous for harvesting a broader solar spectrum [28].

Figure 2.1 shows the different configurations of silicon thin-film solar cells. The superstrate pin structure (2.1a) requires transparent and conducting front contact such as AZO and a highly reflection back contact, either a metal such as Silver (Ag) or a TCO/metal multilayer. Glass as a substrate has the advantage of a wider range of deposition parameters for the front contacts including high temperatures.

The nip configuration (2.1b) on the other hand allows a wide range of substrates ranging from glass to flexible synthetic and metallic foils. However, the application of synthetic substrates limits the deposition parameters. The back contact (BC) must be transparent and the front contact (FC) and substrate can be opaque, respectively. Utilising transparent FC and BC in both pin and nip allows the bifacial application (2.1c) as demonstrated for the nip configuration. This has the advantage that light can enter the solar cell from both sides [29] and the conversion efficiency can be increased from summation of the double-sided gain.

In both configuration and application, the intrinsic silicon layer embedded between

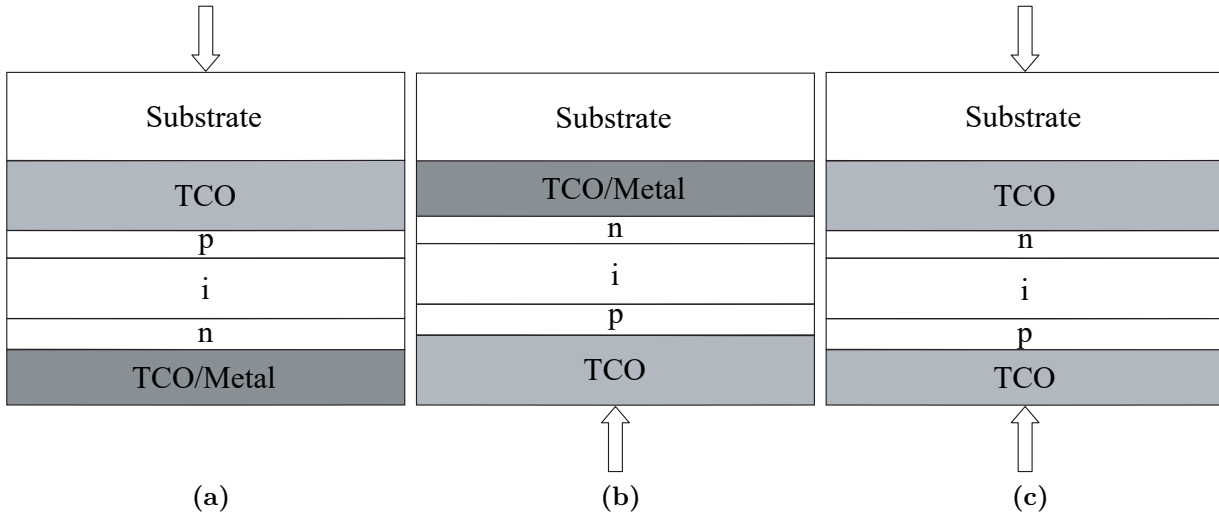


Figure 2.1: Thin-film solar cells in the (2.1a) superstrate and (2.1b) substrate configuration. By using a transparent back contact, both configurations can be operated as bifacial solar cells, as demonstrated for the (2.1c) nip configuration

the positively (p) and negatively (n) doped layers [30] is the functional unit of the solar cell structure. The detailed physics of the solar cells can be found elsewhere [30]. Incident photons with sufficient energy generate electron-hole pairs in the i-layer, which are separated and transported through the doped membranes [30]. The p-doped layer is “selectively permeable” to electrons and the n-layer to holes [30]. Light is intentionally incident through the p-layer because the holes are less mobile than the electrons in the n-layer [26]. Both amorphous and microcrystalline p-layers have a relatively low conductivity [31]. The TCO is used as an additional layer to achieve good lateral conduction with low resistive losses [31].

The optoelectronic properties of the TCO are therefore crucial for the efficiency of the pin and nip configuration [31]. As an example, the TCO film thickness influences the amount of light reaching the absorber material. The TCO resistivity and quality of the TCO/p interface, which is potentially a Schottky pn-junction in the case of AZO, influence the lateral resistivity. These parameters are reflected in the optical and electrical performance of the entire solar cells.

2.2 Light management

Light trapping aims to increase the light absorption in the absorber material and consequently the conversion efficiency. It is achieved by several methods including texturing surfaces. This approach aims to increase the probability of light being reflected at the subsequent layer [12, 14, 28, 31–34], particularly for wavelengths with high penetration depths.

Figure 2.2 shows the light in-coupling concept for thin-film solar cells deposited on

textured TCO (2.2a) and textured glass (2.2b). The texture on the surface is translated into the following interfaces when films are deposited. The geometry on the subsequent layers is changed because aSi:H grows isotropically [35] and $\mu\text{cSi:H}$ anisotropically. The lateral dimensions are extended and the height is reduced [36]. Smaller features disappear and sharp edges are smoothed [37] respectively rounded. Variation in the geometry influences light propagation.

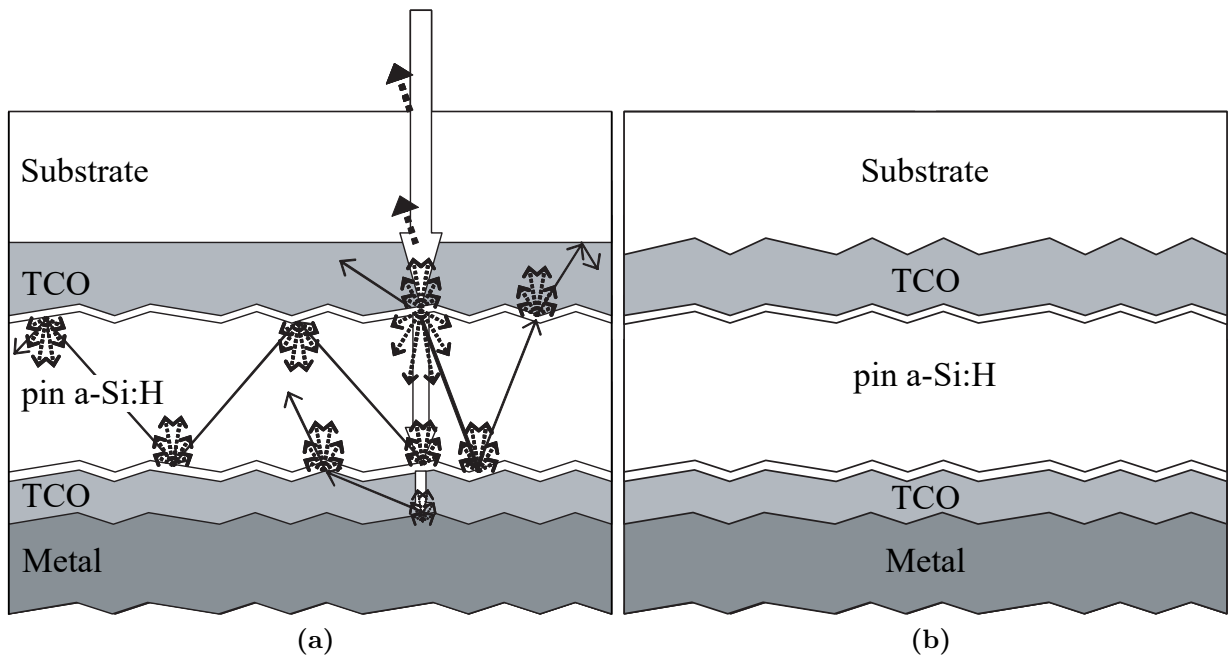


Figure 2.2: Schematic of a pin aSi:H on textured (2.2a) TCO [12] and (2.2b) carrier substrate

The relationship between the lateral dimension of the scattering feature with a lateral dimension D and the wavelength of the incident light determines the scattering regime [38]. For the investigated texture dimensions and wavelengths relevant for silicon thin-film solar cells, the blue region of the spectrum is characterised by the Rayleigh regime $D \ll \lambda$, which shows a high lateral scattering. For $D \approx \lambda$, the Mie scattering results in a partly forward oriented scattering and dominates the green region. Geometric scattering $D \gg \lambda$ is mostly forward oriented and dominates the red spectral region. . Distribution of differently sized features on the surface is advantageous for broadband light scattering. Yablonovitch calculated an upper limit of $4n^2$ for absorption enhancement in transparent mediums with the refractive index n [39].

The texture further reduces the reflection at the TCO/Si interface according to the effective medium approximation [40]. The TCO film also acts as a quarter of the wavelength antireflection layer. With decreasing TCO thickness, the antireflection condition is shifted to the blue region of the spectrum and vice versa for increasing TCO thickness. The antireflection behaviour for high energetic wavelengths requires small and sharp features, while low energetic wavelengths require large features for an effective light scattering [17].

Also, the texture increases the surface area, which increases the volume of absorber material. Reduced reflection, increased optical path and effective absorber material increase the probability of the photons being absorbed.

Research on textured interfaces aims to optimise the topology for efficient light scattering while maintaining good electrical properties [17]. Technological advances made on textured TCO, textured glass and highly conducting electrodes for the application in silicon thin-film solar cells are detailed in the following literature review. The methods used to texture the substrates and the analysed solar cells structures are discussed. This aims to allow a better comparison to the method used in this study, emphasise the simplicity of the texturing technique and highlight the significance of the results achieved (Chapter 6).

2.2.1 Textured TCO substrates

Textured TCO is commonly used to scatter the light at the TCO/Si interfaces. Periodically and randomly textured TCO is obtained from different deposition techniques and texturing methods [10, 12, 14, 16, 26, 28, 31–35, 40–44]. The confirmed efficiencies of silicon solar cells deposited on differently textured TCO using such mechanisms are listed in table 2.1. Moreover, the relationship between the efficiency (η), open circuit voltage (V_{OC}), short circuit current density (J_{SC}) and fill factor (FF) are elaborated in Chapter 3, section 3.6.

Solar Cell	Substrate TCO	η %	V_{OC} mV	J_{SC} mA/cm ²	FF %	
pin aSi:H	LPCVD-ZnO	10.1±0.3	886	16.75	67.8	[10]
nip μ cSi:H	HC-AZO	10.8±0.3	523	28.24	73.2	[11]
pin aSi:H/ μ cSi:H	AZO	12.3±0.3	1365	12.93	69.4	[4]

Table 2.1: Confirmed efficiencies of silicon thin-film solar cells deposited on textured TCO and measured under standard testing conditions

Banagli et al. demonstrate that LPCVD ZnO pyramidal texture as front and back contact improves the efficiency in pin aSi:H [4, 10]. Sai et al. show that periodic Honeycomb (HC) textured substrates with dimensions of 1.5 μ m are advantageous for light in-coupling nip μ cSi:H solar cells [11]. Green et al. review the efficiencies of pin aSi:H/ μ cSi:H deposited on textured AZO [4].

2.2.2 Textured glass substrates

Studies show that textured glass substrates improve the conversion efficiency compared to flat references [16]. Various chemical and physical methods are available to texture the glass substrates from periodic [36, 43, 45–47] to random [15–18, 20, 48–52]. Table 2.2

lists the efficiencies reported for silicon thin-film solar cells deposited on textured glass substrates.

Solar Cell	Substrate Glass	η %	V_{OC} mV	J_{SC} mA/cm ²	FF %	
pin aSi:H	periodic	8.70	833	14.8	70.70	[36]
	random	8.00	860	14.26	65.20	[50]
nip aSi:H	periodic	8.10	886	12.95	71.00	[43]
pin μ cSi:H	random		493	20.00	69.00	[52]
pin aSi:H/ μ cSi:H	Random	10.90	1393	10.90	71.90	[15]
	Random	14.10	1411	28.30	71.50	[17]

Table 2.2: Reported efficiencies of silicon thin-film solar cells deposited on textured glass substrates

Periodic textures have been investigated for both pin and nip solar cells. Isabella et al. investigate pin aSi:H on periodically textured substrates and the observed optimum performance on grating period (P) = 400 nm and height (h) = 300 nm [46]. They obtain the results from simulations of the structure glass, AZO (800 nm), p-aSiC:H (20 nm), i-aSi:H (300 nm), n-aSi:H (20 nm), ZnO (100 nm), with aSiC:H hydrogenated silicon carbide [46]. The experimental validation of a similar solar cell structure on 1D grating shows the best performance on diffraction grating with $P = 600$ nm and $h = 300$ nm [36] (table 2.2).

Naqavi et al. and Söderström et al. report on simulation [47] and experiment [43] of nip deposited on 1D grating substrates. Both investigations study the structure configuration BC, Ag (120 nm), ZnO (60 nm), n-aSi:H (200 nm), aSi:H (17 nm), ITO (65/60 nm) where ITO is indium tin oxide. Naqavi et al. identify the “sawtooth” gratings as the optimal texture and observe a change in antireflection in the short wavelengths with changing grating shape and depth [47]. Söderström et al. obtain the 1D gratings experimentally by UV-nano-imprint lithography [43]. They conclude the 1D gratings are not ideal for light scattering for the application in nip solar cells due to wavelength selectivity and polarization sensitivity [43]. In addition, they attribute the observed absorption enhancement (table 2.2) to the excitation of guided modes [43, 47].

Sahraei et al. show that random textures in the micron range obtained from aluminium-induced glass texturing (AIT) [18] are more suitable. They define the optimum autocorrelation length for AIT glass between 75-150 nm [48] and show that pin aSi:H absorption increases in comparison with the reference. They study the structure configuration glass (texture), AZO (900 nm), p-aSi:H (25 nm), i-aSi:H (117/270 nm), n-aSi:H (20 nm), AZO(100 nm) [18].

An alternative physical texturing method studied by Taniguchi et al. is sandblasting bombardment of SiC fine particles [50]. They show that various textures can be obtained by changing the nozzle-substrate distance, particle size and jet pressure [50]. The performance of the structure glass (texture), ITO, ZnO, p-aSi:H (12 nm), i-aSi:H (200 nm) and

n-aSi:H (30 nm) on sandblast textured substrates is shown in table 2.2.

Etching methods are often used and required in multi-step texturing techniques such as lithography [43]. Hongsingthong et al. investigate reactive ion etching (RIE) using carbon tetrafluoride (CF_4) to texture the glass and additionally wet-chemical etch the AZO with HCl [20]. They obtain double textures with high roughness of $\sigma_{rms}=250$ nm and observe that J_{SC} of pin aSi:H deposited on the textured substrates increases [20]. Also, they investigate the structure in the configuration glass (texture), AZO (1000 nm) (texture), p-aSiO:H (buffer), i-aSi:H (300/400 nm), n-cSiO:H, Ag, Al [20].

Zhang et al. also investigate ion beam etching of glass substrates and obtain topologies comparable to sputtered and post wet-chemical etched AZO by adjusting etching parameters [52]. The surface texture of the glass had crater depths in the range of $h > 500$ nm and roughness $\sigma_{rms} > 115$ nm, respectively. The performance of single junction $\mu\text{cSi:H}$ solar cells (table 2.2) deposited on the highly textured substrates decreased compared to state-of-the-art wet-chemically textured AZO. Furthermore, Zhang et al. observe that the AZO properties deteriorate on highly textured substrates [52]. The structure and thicknesses investigated were glass(texture), AZO (500 nm), pin $\mu\text{cSi:H}$ (1100 nm), AZO (80 nm), Ag (700 nm).

Neubert et.al show that the performance of micromorph pin aSi:H/ $\mu\text{cSi:H}$ solar cells on wet-chemical etched glass substrates is comparable to textured AZO [15]. They employ several steps of etching with inorganic fluorine to texture the glass substrates and obtain lateral feature dimensions of approximately 700 nm. The solar cell structure investigated glass (texture), $\text{SiO}_x:\text{N}_y$ (60 nm), AZO (250 nm) (texture), p- $\mu\text{cSiO}_x:\text{H}$, i-aSi:H (270 nm), n- $\mu\text{cSiO}_x:\text{H}$, n- $\mu\text{cSiO}_x:\text{H}$, i- $\mu\text{cSi:H}$ (1750 nm), n- $\mu\text{cSiO}_x:\text{H}$, Ag, Al showed acceptable performance as shown in table 2.2.

Improved performance of tandem solar cells on textured glass is reported by Boccard et al. [17]. They deposit the solar cells on glass textured by “high-fidelity UV-nil nano-imprint lithography technique” [17]. They investigate the structure consisting of glass (texture), IOH (120 nm), ZnO (1000 nm), $\text{SiO}_x:\text{H}$ (60 nm), pin-aSi:H (290 nm), pin- $\mu\text{cSi:H}$ (2600 nm), ZnO (2400 nm), white paint [17]. The BC was an LPCVD ZnO which was highly doped and had the properties $R_S \approx 50 \Omega$, $N_D = 4 \times 10^{19} \text{ cm}^{-3}$ and $\mu_H = 30 \text{ cm}^2/\text{Vs}$. the ZnO was additionally coated with white dielectric reflector [17]. The performance of the solar cell is shown in table 2.2.

2.2.3 Highly conducting ultra-thin <200 nm electrodes

Another aspect to be taken into consideration is the required and technologically possible properties of the front electrodes deposited on the textured glass substrates. For this application, the electrodes ideally have to be (I) highly transparent to reduce parasitic absorption and (II) highly conducting to reduce the resistivity losses. There is however a trade-off between these properties. Studies have further shown that the electrical proper-

ties of AZO deteriorate with increasing texture on the glass surface [52].

The technological advances made to obtain ultra-thin and highly conducting electrodes aim to investigate alternative materials, optimise the growth and adjust the deposition conditions, respectively [17, 19]. Boccard et al. obtain 120 nm hydrogenated indium oxide (IOH) with a high mobility $\mu_H > 100 \text{ cm}^2/\text{Vs}$, low carrier density $N_D = 1 \times 10^{20} \text{ cm}^{-3}$ and low sheet resistance $R_S < 50 \Omega$ [17]. These films are further highly transparent for a wide spectral range relevant to tandem solar cell operation because the charge carrier density is low [17].

Studies demonstrate that upcoming materials such graphene, a 2D carbon material and nanotubes [19] can be used as an alternative transparent electrode in high efficiency thin-film photovoltaic technologies. Comparable optoelectronic properties are obtained. The technology shows the potential for low-cost and large-area production by chemical vapour deposition (CVD), a technique commonly applied in the thin-film industry [19, 53, 54]. Graphene is however highly absorbing. Hence only mono or double layers embedded in semiconductors such as ZnO [54, 55], which can be exploited as antireflection layers between the carrier substrate (also flexible substrates) and absorber material could be promising candidates. This approach can be beneficial in the search for low-cost front alternative electrodes and absorber materials and find application in a variety of inorganic and organic photovoltaics in either superstrate pin or substrate nip also for bi-facial application configurations.

To summarise, the review shows that a range of electrodes are available and applicable for thin-film solar cells on textured glass substrates. The literature review also shows that textured glass substrates have several advantages, which have been realised experimentally. Efficiencies comparable to state-of-the-art textured AZO (table 2.1) concepts are demonstrated for solar cell on textured glass substrates (table 2.2). However, the chemical etching based methods used to texture the glass substrates are rather complex and often require several processing steps and are thus resource consuming. This is indeed a crucial aspect for production costs. Simple texturing methods would contribute to advancing the concept and form the basis of this work.

Few studies have been dedicated to laser texturing as a method to achieve light in-coupling in thin-film solar cells. Nanosecond lasers are readily used in photovoltaics for monolithic connection of modules [25]. Moore et. al study laser-textured glass for the application as solar cells encapsulation [24]. They however employ very large grooves with 72-947 μm depth and 146-213 μm width [24]. The more commonly found application for ps and fs micro-structured glass is for waveguide scribing [56]. According to the authors' knowledge, a systematic investigation of laser texturing multi-component glass with a ps laser for the application in silicon-thin-film solar cells has not been reported in literature.

2.3 Aim and scope

In this work, multicomponent glass substrates commonly used in photovoltaics are textured with a ps laser. The laser-setup used for the investigation also houses optics for a ns laser, which is used for monolithic connection in modules. Using the same setup has the advantage that no additional materials are required, provided the ps laser optics are integrated. Direct ablation technique promises to be a simple alternative to chemical etching processes because the texturing is achieved in one step using single-pulses. For a better assessment of the cost reduction potential, a life cycle assessment (LCA) from cradle-to-grave would be the best approach to compare the methods. The acquisition, running, maintenance, waste disposing and recycling aspects etc. have to be taken into consideration. This is however out of scope of this work.

An added advantage of using the ps pulsed laser is the possibility to alter the texturing degree and periodicity by changing the scribing speed. Differently textured substrates are expected to alter the light scattering behaviour, which is desired for the application in thin-film solar cells. An important aspect to be taken into consideration is the structural, defect and even micro-crack formation, depending on the pulse energy. The influence of the pulse energy on the quality of the texture is therefore also investigated.

The topology of the textures are statistically analysed to assess their potential for the application in silicon thin-film solar cells. The UV-VIS optical behaviour of the substrates is investigated to assess the potential for light in-coupling. Zhang et al. observe that the AZO properties deteriorate on highly textured substrates and propose pre-processing glass substrates prior AZO deposition [52]. Understanding the nature and cause of undesired topology with high aspect ratios can deliver information on how the ablation process and parameters can be optimized to avoid such textures.

The molecular vibration modes of differently textured Type II substrates are analysed for the structural modifications following ablation. This is an important aspect because (I) it delivers insight on how the modifications can be avoided or mitigated and furthermore (II) delivers an indication on how AZO deposited on the textured glass substrates might be affected. AZO used in silicon thin-film solar cells is deposited at temperatures ranging between 100-450 °C [32]. The glass substrates are preheated before the AZO deposition. Studies show that annealing laser-textured glass substrates reduces the laser-induced modifications [56]. The laser-textured substrates are therefore annealed at the temperatures used for AZO deposition to investigate whether material modifications are observed.

AZO films deposited on the differently textured substrates are investigated. For a better understanding of the impact of the substrate chemistry and topology, theoretical growth models are summarised along with parameters relevant for the different stages during growth. Micro-structural, electrical and optical properties of the AZO films are

analysed. Thin-film solar cells are deposited on the differently textured glass substrates coated with AZO. The performance of the different solar cell configurations on the different textured substrates is analysed. However, the optimisation of AZO and solar cell deposition are out of scope of this study.

To nevertheless demonstrate the effect of optimising the TCO thickness, a numerical modelling approach is taken. The performance of state-of-the-art ultra-thin TCO and pin aSi:H solar cells on highly textured substrates is modelled. First, the experimental details and characterisation techniques used to quantify and compare the textured substrates, AZO and solar cell properties on differently textured substrates are outlined in the following Chapter 3.

3 Experimental details

In this chapter, the sample preparation steps are first summarised. Then the characterisation methods used to assess the quality of textured glass substrates, deposited AZO and silicon thin-film solar cells are outlined. The principles of the methods relevant to understand the results discussed in the following chapters are detailed. These also aim to provide a better understanding of the simulation input and output parameters.

3.1 Sample preparation

Three commercially available glass types, two aluminoborosilicate glass, one containing alkali, the other earth alkali metal, and a soda-lime readily used in photovoltaic research were investigated. (The properties of the glass substrates are discussed in Chapter 4, section 4.1.1). First, the glass substrates were cleaned in a laboratory glassware washer and then characterised. The thickness was taken from material specification (Chapter 4.1.1) and controlled with a digital vernier caliper.

The precise substrate thickness was required to place the surface in the focal point of the laser beam for texturing. (Theory of glass and laser interaction is described Chapter 4, section 4.1.2). The glass substrates were textured with a research and development Lumera Super Rapid 18 W, neodymium-doped yttrium vanadate (Nd:YVO₄) diode-pumped picosecond (ps) solid-state laser (DPSSL) from 3D-Micromac. Gaussian profiled laser beam, with a wavelength of $\lambda_{ps}=1064$ nm and pulse duration $\tau_{ps}=8.5$ ps was used. The scribing was carried out with a galvo-head scanner with a scanning field of 5 cm×5 cm and an objective of 80 mm focal length. Textured and reference substrates were annealed at a temperature variation between 150-450°C for 3600 s.

AZO films were deposited on the later textured, glass substrates by DC magnetron sputtering using a ZnO ceramic target containing 2wt% Al₂O₃. Flat reference was co-deposited with the differently textured glass substrates for a better comparison of the influence of the texture. A series with varying deposition times between 50-1600 nm was carried out at a constant temperature of 350°C. The other deposition parameters were kept constant as well, including the argon and oxygen gas flow at 100.0 and 0.5 sccm, respectively. The target-substrate distance was 70 mm and the power was 1 kW. The base and deposition pressure were kept constant at 5×10^{-6} mbar and 6×10^{-3} mbar, respectively.

The thicknesses of the solar cells and the AZO films were measured with a DEKTAK profilometer. Furthermore, the AZO film thicknesses were used for Hall measurements which were carried out with the ACCENT HL550 setup. The resistivity, carrier concen-

tration and mobility were determined using laser scribed van der Pauw structures. The sheet resistance was determined by four-point probe with the setup from Jandel RM3-AR.

Finally single junction superstrate (pin) aSi:H, substrate (nip) and tandem micro-morph (aSi:/ μ cSi:H) solar cells were deposited on the flat reference and the textured glass substrates coated with AZO. The hydrogenated silicon (Si:H) layers were deposited by plasma-enhanced chemical vapour deposition (PECVD) at substrate temperatures around 220°C using a 13.56 MHz plasma excitation frequency [57]. The intrinsic layers were deposited from SiH₄:H₂ gas mixture and B₂H₆ and PH₃ were added for p- and n-doping, respectively. To avoid contamination of the intrinsic layer, SiO₂ buffer layers were deposited between the intrinsic and the doped layers [57, 58]. The thicknesses of the p and n-layers were 10 nm and 25 nm, respectively. The intrinsic layer thicknesses were 200 nm and 700 nm for the aSi:H and μ cSi:H, respectively. Finally the back contact consisting of 100 nm AZO and 300 Ag was deposited and the solar cells annealed for 30 min at 160 °C.

3.2 Surface morphology

Atomic force microscopy (AFM)

AFM measurements were carried out to visualise the textured surfaces. The measurement technique uses a tip to scan the x- and y-plane and digitize the surface height profile in the z-axis. As the tip is moved closer to the surface and the tip-sample distance is reduced, attraction and repulsion forces occur, respectively. The interaction of the tip with the sample is illustrated in figure 3.1. This interaction forms the solid-state physical principles of the measuring technique. A detailed description of the method can be found elsewhere [59–61].

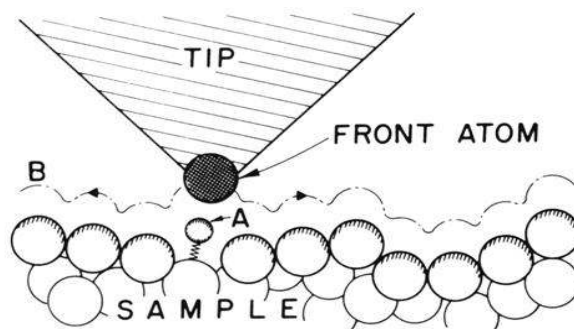


Figure 3.1: Atomic force microscopy (AFM) tip-sample interaction [59].

The measurements were carried out in the phase contrast-tapping mode, where the surface is tapped in discrete points. A reference oscillation with a characteristic phase ($\phi_{reference}$) is obtained by exciting the cantilever (on which the tip is mounted) with a piezo element to oscillate vertically near its resonance frequency far away from the sample. As the tip approaches the sample, the oscillation amplitude is reduced and the

height information at the point is noted once the amplitude reaches a defined damping limit (force). The oscillation phase (ϕ_{actual}) is shifted compared to the reference $\phi_{reference}$ [60, 61]. The difference between the former and the later forms the measured (output) phase ($\phi_{measured}$), which is calculated by

$$\phi_{measured} = 90^\circ \sin(\phi_{actual} - \phi_{reference}) \quad (3.1)$$

This is a significant characterisation tool for laser-textured topologies. The chemical composition of the surface is expected to change following ablation and phase contrast-ing provides a tool of characterising this change as shall be shown in Chapter 4, section 4.1.3. Precaution should nevertheless be taken in interpreting the results, as the measurements are affected by the roughness. For a better comparison with literature, the setup characteristics are detailed.

A Nanosurf Mobile S atomic force microscopy (AFM) was used for the measurements. A negatively doped (N-type) silicon cantilever with the length $L=225\mu\text{m}$, width $W=40\mu\text{m}$, breadth $T=8.5\mu\text{m}$ and a resistivity of $0.01\text{-}0.025\ \Omega/\square$ from AppNano was used. The tip was aluminium coated and had the following specification; radius $<10\text{ nm}$, height $14\text{-}16\ \mu\text{m}$, frequency $f_{cl}=145\text{-}230\text{ kHz}$ and spring constant $k_{sc}=20\text{-}95\text{ N/m}$. The vibrating oscillation amplitude was set to 0.2 V respectively 40% force.

The measurements were carried out on $100\times 100\ \mu\text{m}$ areas with $N_{x,y}=1024$ or $50\times 50\ \mu\text{m}$ with $N_{x,y}=512$ points and lines in the x- and y-direction under slope correction, respectively. Level correction was carried out before further evaluation and visible artefacts were removed. The 3D height profile $z_{i,j}(x_i, y_j)$ is therefore a function of the spatial coordinates x_i and y_j , where i and j are the indices of measurement points per line ($i=1,2,\dots,N_i$) respectively of the line ($j=1,2,\dots,N_j$) [32]. This aspect is used to import AFM data into the simulation tool and to achieve simulations with realistic surfaces (Chapter 7).

The lateral (width) and vertical (height) texture dimensions can be evaluated statistically to obtain the surface height h , auto-correlation length LCA and roughness σ_{rms} . The roughness σ_{rms} is the root mean square (RMS) relative to the centre plan of the structure height and is given by [62].

$$\sigma_{rms}(x_i, y_j) = \sqrt{\frac{1}{N_x N_y} \sum_{i=0}^{N_x-1} \sum_{j=0}^{N_y-1} (z(x_i, y_j))^2} \quad (3.2)$$

A high σ_{rms} indicates a highly textured surface. A homogeneously textured surface can however deliver the same σ_{rms} as a surface with few larger structures respectively deep craters on an otherwise smooth surface.

The spatial frequency is therefore an important surface texture descriptor complementary to the height [63] and is given by the autocorrelation function ACF

$$ACF(\Delta_{x,y}) = \exp\left(-\frac{\Delta_{x,y}}{ACL}\right) \quad (3.3)$$

where $\Delta_{x,y}$ is the spatial separation and ACL the autocorrelation length. ACL is a measure of how quickly the random event decays and is sometimes defined as the distance at which the autocorrelation function drops to $1/e$ respectively 37%. ACL of flat reference approaches infinity, while a rough surface with larger particles has a higher ACL than a surface with smaller particles.

Another parameter used to characterise textured surfaces is the skewness (Ssk) of the height distribution [63].

$$Ssk = \frac{1}{N_y \sigma_{rms}} \sum_{j=0}^{N_y} y_i^3 \quad (3.4)$$

The skewness delivers information on the distribution of valleys and peaks on the surface. This is particularly important for laser-textured substrates because scribing is achieved with varying scribing speeds and laser spot overlap occurs (Chapter 4). Figure 3.2 shows examples of height distributions of differently textured substrates.

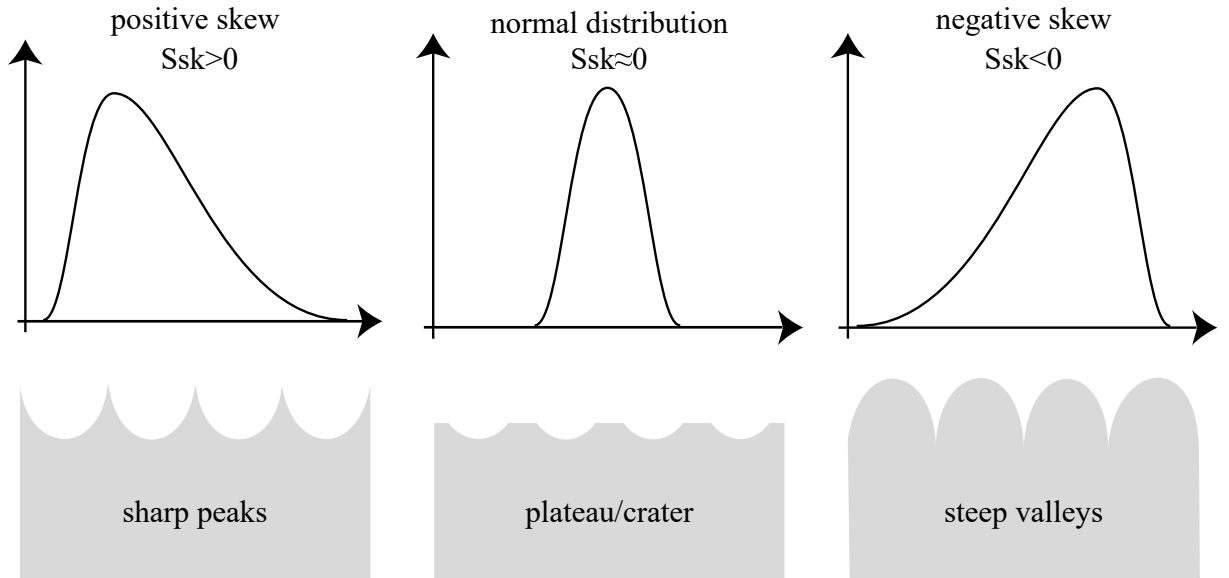


Figure 3.2: Skewness Ssk of differently textured surfaces

The regions with high laser spot overlapping on the surface might result in steep valleys. The ablation of directly neighbouring craters might result in peaks, which might be detrimental for the solar cell performance. An otherwise smooth surface with steep valley would show negative Ssk. A positive Ssk indicates the presence of peaks on a plane. This is an important aspect in classifying the topology achieved by laser scribing in comparison to conventionally used wet chemically textured AZO.

It should however be mentioned that the discrete tapping mode is limited by the resolution. A number of artefacts can occur in the presence of foreign particles on the

surface and wearing of the tip can occur. The resolution can also influence the quality of the measured topology particularly for textures with steep edges. The used parameters must therefore be interpreted with caution. Trends can nevertheless be identified by analysing σ_{rms} , ACL and Ssk together. The software Gwyddion [64] was additionally used to determine the latter parameters and the results are discussed in Chapter 4, Section 4.1.3.

Scanning electron microscopy (SEM)

SEM was utilised as a complementary topology characterisation technique. Details on the principles can be found elsewhere [60]. The fundamental of the technology is a focused electron beam scanning across the surface at an adjustable angle. Electrons reflected on the surface (primary) and in the material (secondary) are detected by two different detectors respectively. The intensity of the electrons is dependent on the material properties which can be displayed as a contrast two-dimension image [60]. Neon 40 ESB SEM from Zeiss was used in this study.

3.3 Optical properties

Photo-spectroscopy

The measurements were carried out for the wavelengths between 200-2500 nm with a double beam Varian Cary 5000 Diffuse Reflection Accessory (DRA) 2500 housing an integrated sphere. The setup uses a Deuterium lamp as UV (200-350 nm) and a Tungsten-halogen lamp as VIS-NIR ($\lambda > 350$ nm) light source. Monochrometers were changed at 800 nm together with the detector from a photomultiplier tube (PMT) for the UV-VIS to a thermostated Lead Sulphide (PbS) detector for the NIR spectrum. This is an important aspect, as it explains slight noise and offset in the signal observed in some measurements at the wavelengths around 800 nm.

The measurements were relative and referenced against a PTFE plate also used for the baseline correction. Total reflection R and transmission T_T measurements were carried out for both sides of the substrates; first with the beam striking the flat glass surface and second with the beam striking the textured side. The absorption A of the samples was calculated by

$$A = 1 - T_T - R. \quad (3.5)$$

The diffuse transmission T_D was measured by removing 6.5° specular intensity, and the deduced haze factor in transmission H_T is given by

$$H_T = \frac{T_D}{T_T} \quad (3.6)$$

describing the fraction of light that is scattered (diffused) compared to the total transmitted intensity. It is therefore a spectral integrated factor and does not give information about the angular dependency of the scattered light.

Angular resolved scattering

This information is obtained from angular resolved measurements, which were carried out with an Absolute Reflection Transmission Analyzer (ARTA) from OMT Solutions. Figure 3.3 shows the measurement setup and analysis principle. Samples were placed with the flat surface facing the beam at a detector-sample distance $d=92$ mm.

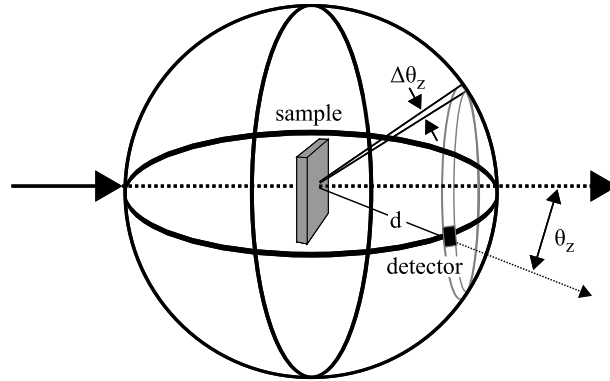


Figure 3.3: Angular resolved measurement setup and data analysis principle, modified from [65]

The detector was moved in plane to collect the scattered intensity at the respective angle. The detector is an integrating sphere made of pressed PTFE and equipped with a photomultiplier for the UV-VIS range and a PbS detector for the NIR range [66]. Rectangular entrance port has a height of 15.5 mm and the width can be adjusted between 0 mm (closed) and 24 mm (wide open) with two adjacent micrometer screws. The resolution of the measurement is given by the detector opening angle. This can be considered to be a solid angle extended by the 92 mm detector-sample distance with a height of 15.5 mm. Steps of the detector during measurement have to correlate with the detector opening. As an example, a detector aperture width of 8.2 mm corresponds to an angle of 5° .

Before the measurements were carried out, 0 and 100% baseline were taken with the detector at 0° . The detector opening was kept at 8.2 mm and moved from -90° to $+90^\circ$ in 5° steps around the sample. At each angle and wavelength, both P and S polarisation were measured and averaged. While the data is measured in one plane (2D), the sample scatters in 3D. For samples scattering isotropically, the averaged intensity can be projected into 3D as detailed in Ref. [65, 67, 68].

Ellipsometer spectroscopy

Ellipsometer measurements were thus carried out with the SENTECH SE850-ST setup using UV-VIS light sources to analyse the modification. The optical constants were fitted

from ellipsometer and photo-spectrometer measurements with the software CODE/SCOUT.

The characterisation method is however only applicable to optically smooth films and surfaces. Thus characterisation of textured glass substrates was limited to periodically textured substrates with crater diameters $\geq 20 \mu\text{m}$ in the range of the light beam diameter. The detailed description of the principles can be found elsewhere [69, 70]. Furthermore, optical constants of reference TCO and silicon films were required and used as simulation input parameters.

3.4 Raman optical properties

Raman measurements were carried out in reflection using a laser monochromatic visible 488 nm excitation source. The measurements were carried out with a Senterra Raman Spectroscope and the laser power was set to 20 mW for an integration time of 60 s for each measurement. Five measurements were made on each sample and a correction of the cosmic spikes was carried out for the spectral range between $41\text{-}1875 \text{ cm}^{-1}$ with a resolution of $3\text{-}5 \text{ cm}^{-1}$.

Raman measurements were carried out on glass substrates to identify which structural units were most affected following laser ablation. This information was used to analyse the structural variation induced by annealing of the laser-textured glass substrates. The crystallinity of the $\mu\text{cSi:H}$ single junction solar cells deposited on differently textured substrates was determined from baseline corrected and deconvoluted Raman spectra. The crystallinity fraction (Φ_c) was calculated from the ratio between the crystalline and sum of crystalline and amorphous peak area [71, 72]. The detailed measurement and data correction procedure for $\mu\text{cSi:H}$ is described elsewhere [72].

While the crystallinity analysis might be a standard procedure, Raman measurements on amorphous glass substrates might not be as familiar in PV research, although it is a standard characterisation technique in glass manufacturing and research. The details of the fundamentals and physics of the technique can be found in literature [73] and are outlined shortly in the following with respect to silicate glass.

Molecular vibration modes and Raman scattering

IR spectroscopy is based on the interaction between an external electromagnetic wave of known energy with the molecular vibrational states of the investigated sample [60, 73, 74]. The incident electromagnetic wave displaces electrons of the atoms in the molecule [73]. A molecular dipole moment is induced which is dependent on the magnitude of the atomic charges and their positions [73]. A molecule with N atoms has $3N$ different (motion in the X, Y, and Z directions) internal degrees of freedom and $3N-6$ non-linear possibilities to vibrate [75]. Some non-linear vibration modes might however have the same resonance frequency as a result of the symmetry of the structural unit [75]. In glass substrates,

the electromagnetic waves interact with structural units such as the tetrahedra SiO_2 or groups/rings of structural units [75] (The chemical composition of glass is discussed Chapter 4). Figure 3.4 shows the four observed (instead of nine) vibration modes for SiO_2 tetrahedra.

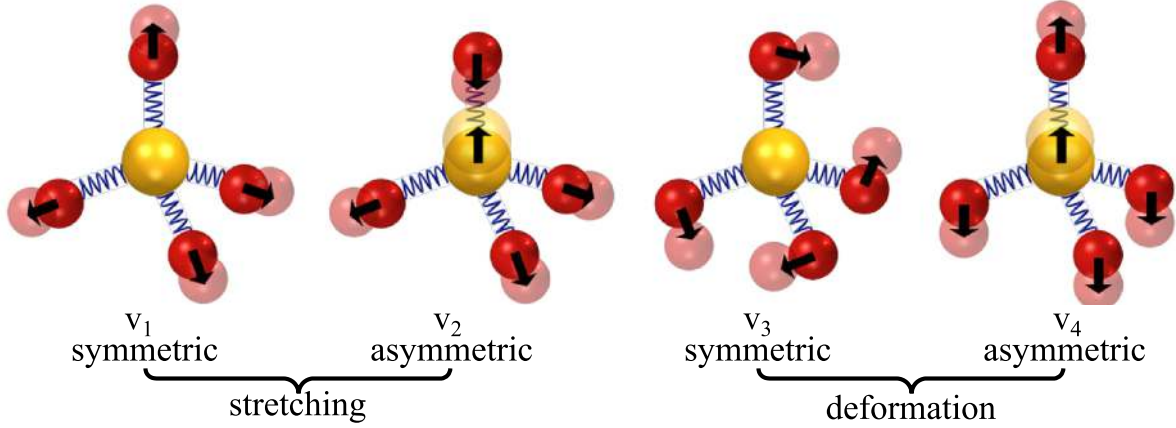


Figure 3.4: Schematic of tetrahedra vibration modes [75]

The induced dipole moment leads to the absorption of an incident high energetic photon and the molecular vibration state transitions to a virtual state [73]. A new photon is re-emitted/scattered with a different energy and the molecule transitions back to the initial state [73]. When the molecule is initially in an excited state and the photon is re-emitted to the ground state, the scattering is termed Anti-Stokes [73]. Stokes scattering occurs when the molecule is initially in the ground state and the photon is re-emitted into a vibrational state [73]. Most molecules at room temperature exist in the ground state, hence the Stokes scattering is more intense and probable than the Anti-Stokes scattering [73].

Raman Spectroscopy

Figure 3.5 shows an example of a Stokes Raman spectrum of earth alkaline aluminoborosilicate Type II glass. A direct comparison between the raw measured (I_{exp}) spectra of the differently textured substrates was difficult because the difference in the intensities were in some cases magnitudes high. D'Angelo et. al note that the Raman intensity depends on the optical quality of substrates [76]. For this purpose, the following correction and normalization procedures were conducted to be able to compare the results.

The measured spectra were corrected for frequency and temperature-dependent scattering intensity by [77]

$$I_{red} = \frac{I_{exp}}{\omega [n(\omega, T) + 1]} \propto \frac{g(\omega)C(\omega)}{\omega^2} \quad (3.7)$$

where I_{red} is the corrected intensity and shall henceforth be termed reduced Raman in-

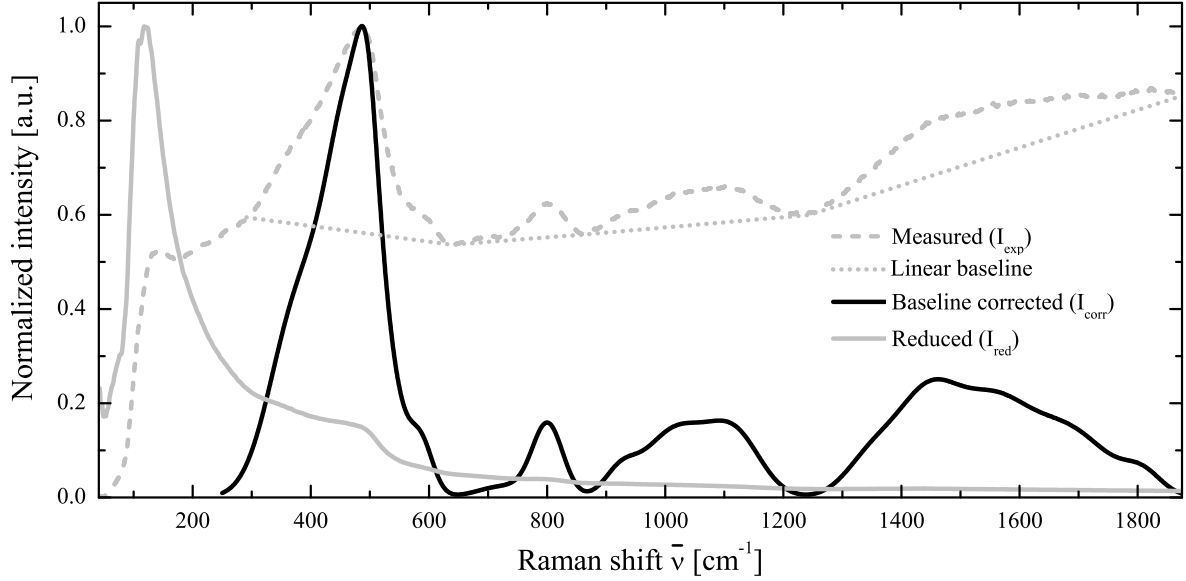


Figure 3.5: Correction and reduction procedure for the raw Raman spectra (I_{exp}) demonstrated for Type II glass substrates measured for the range between 42-1875 cm^{-1} . The spectral region $\bar{\nu} < 300 \text{ cm}^{-1}$ was reduced (I_{exp}) as described by Shuker and Gammon et. al [77] and the region $\bar{\nu} > 300 \text{ cm}^{-1}$ was corrected (I_{corr}) by fitting a linear baseline.

tensity, ω is the frequency, $n(\omega, T)$ is the Bose-Einstein relation at room temperature $T=293 \text{ K}$, $g(\omega)$ the vibrational density of states and $C(\omega)$ is the photon-phonon coupling coefficient. Reduced Raman spectra are considered to be “free of spurious structure due to thermal population effects” [78].

The reduced spectra were used to analyse the low frequency region $\bar{\nu} < 300 \text{ cm}^{-1}$ as shall be discussed in detail in Chapter 4, Section 4.3.1. The reduction procedure does not change the forms of the bands in the spectral region $> 300 \text{ cm}^{-1}$ [79]. For this reason, a linear baseline was fitted to the raw spectra at about 250, 640, 860, 1245 and 1875 cm^{-1} (3.5). The influence of the different reduction procedures [80] and baseline types can be found elsewhere [81–83]. The baseline corrected spectra I_{corr} were deconvoluted with Gaussian peaks for the spectral region $> 300 \text{ cm}^{-1}$ using the software Fityk [84] and discussed in detail in Chapter 4.

3.5 Microstructure properties

The influence of textured glass surface topology and morphology on the microstructure of sputtered AZO films was investigated by XRD-diffraction spectroscopy.

3.5.1 X-Ray Diffraction (XRD) Analysis

The measurements were carried out with a powder X-Ray diffraction (XRD) from PANalytical X’Pert PRO MPD diffractometer equipped with a $\text{Cu K}\alpha$ radiation ($\lambda = 1.5418 \text{ \AA}$).

Samples were rotated in plane on a goniometer and the beam was incident and detected at varying angles.

The characterisation principle is based on the interaction between the incident X-Rays with the structural units constituting the material. In a simplified approach illustrated in figure 3.6, the crystal lattices are considered to be planes separated by a distance. Incident radiation $I_{i,1}$ and $I_{i,2}$ on two parallel planes at a defined angle θ_i is diffracted by the atoms along the plane into the angle θ_r . Interference conditions of the diffracted radiation $I_{r,1}$ and $I_{r,2}$ can be described using the Bragg formalism.

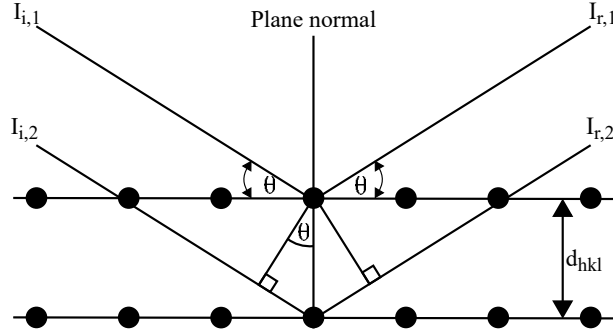


Figure 3.6: Schematic illustration of the Bragg condition, modified from [85]. The incident radiation ($I_{i,1}$ and $I_{i,2}$) at the angle (θ_i) is reflected in the (θ_r) with the intensities ($I_{r,1}$ and $I_{r,2}$) by atoms in planes separated by a distance (d). Constructive interferences of the reflected radiation occur when the Bragg criterion ($n\lambda = 2d\sin\theta$) is met.

Constructive pattern is observed when the criterion

$$n\lambda = 2d\sin\theta \quad (3.8)$$

is met, where n is an integer, λ the wavelength of the incident radiation, d the distance between the planes, and θ the angle of incidence. The distance between the planes is a crystallographic class-dependent parameter, which shall be denoted as d_{hkl} according to the miller indices (hkl). For the investigated AZO which crystallizes in the wurtzite structure, the lattice parameters are calculated from the lattice geometry equations

$$\frac{1}{d_{hkl}^2} = \frac{4}{3} \left(\frac{h^2 + hk + k^2}{a^2} \right) + \frac{l^2}{c^2} \quad (3.9)$$

The latter parameters are collectively representatives of the corresponding crystallite size and lattice strain, which are commonly used to quantify the crystal quality. Thus, measured Bragg reflection can be used to determine the former and latter. While crystallite size is a measure of a coherently diffracting domain, lattice strain is a measure of the distribution of lattice constants arising from crystal imperfections.

Figure 3.7 demonstrates how reflexes are changed by crystal deformation. Imperfections include lattice dislocation, grain boundary triple junction, contact or sinter stresses, stacking faults and coherency stresses amongst others. Shift of 2θ to lower angles is also

an indication of uniform strain [85–87].

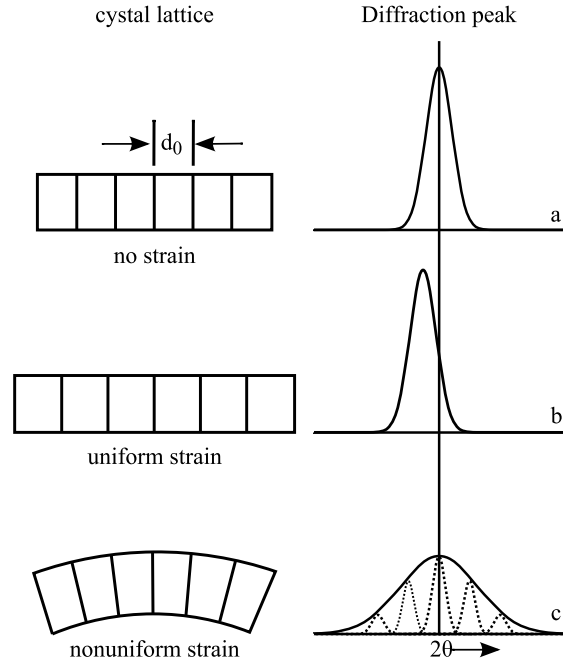


Figure 3.7: Influence of the crystal lattice strain on the XRD peak intensity and position with (a) no strain, (b) uniform strain and (c) nonuniform strain [87].

Reduced correlation length normal to the substrate plane and heterogeneous strain along the c-axis broadens the Bragg reflex [87–92]. Broadening of β_{hkl} and lowering of counts are an indication of a non-uniformly strained crystal lattice. A possible procedure to quantify crystal size and strain is the Williamson-Hall method illustrated in the following.

3.5.2 Williamson-Hall Method

Peak broadening is quantified by the full width at half maximum (FWHM) β of the peak profile. Experimentally measured FWHM β_{exp} is partially influenced by the instrument β_{intr} used for characterisation. Therefore, the first step in the analysis is deducting the instrument broadening

$$\beta_{hkl} = \sqrt{\beta_{exp}^2 - \beta_{intr}^2} \quad (3.10)$$

where

$$\beta_{intr} = \sqrt{(-0.005260679 \cdot \tan^2\theta) + (0.012269341 \cdot \tan\theta) + 0.018837553^2} \quad (3.11)$$

is for the used equipment.

Several assumptions are made by the Williamson-Hall method regarding the cause of β_{hkl} including crystal size, uniform and non-uniform strain. In the investigations carried

out, AZO films of one thickness were deposited under the same conditions, with the substrate texture being the only variable. Since the nature of strain in the films is unknown, it makes sense to evaluate the data with different models assuming different properties of the strain.

The contribution of the crystalline size to peak broadening β_D is given by the Scherrer method

$$D = \frac{K\lambda}{\beta_D \cos\theta} \Rightarrow \cos\theta = \left(\frac{1}{\beta_D}\right) \left(\frac{K\lambda}{D}\right) \quad (3.12)$$

where D is the crystal size, K the Scherrer constant and β_D the reflex broadening caused by the crystallite size. D is thus a measure of the diameter of crystallites, perpendicular to the plane [85]. The dimensionless Scherrer constant, also commonly termed structure constant, shape factor and correction factor in literature, depends on the shape of the crystallites and on the distribution of the coherent diffracting domains (CSD) [93]. Different values including 0.89 [86], 0.9 [92, 94], 0.94 [87], 1 [95], 1.05 [96] have been reported for ZnO. Moreover, different deposition techniques and parameters deliver differently shaped grains.

Figure (3.8) shows SEM images of AZO DC sputtered at different temperatures (3.8a) 350 °C and (3.8b) 450 °C, but otherwise under the same conditions and flat glass substrates. Different crystallographic orientations are observed under same deposition conditions and show different shapes. As shall be discussed in the AZO Chapter 5, different glass surface textures also influence the microstructure. The complexity of sputtered AZO makes it difficult to define the shape of the grains for each sample. Thus, for simplicities sake, an intermediate value $K=1$ was chosen for all the analysis carried out in this study.

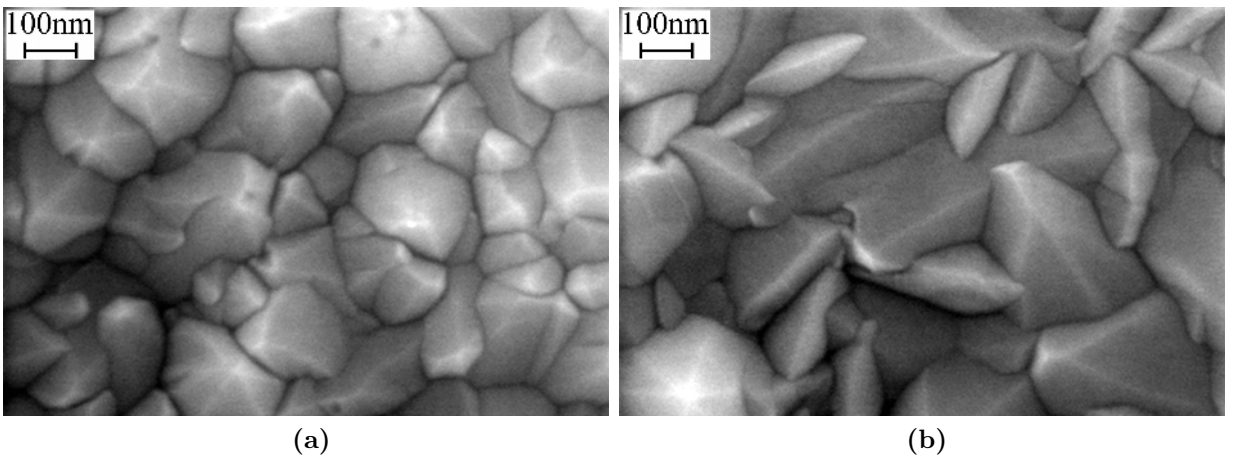


Figure 3.8: SEM images of ≈ 1300 nm AZO deposited on Type II flat reference at (3.8a) 350 °C showing grains hexagonally close-packed (002) and (103) orientation and at (3.8b) 450°C showing (002) and (101) orientation.

Figure 3.9 shows the Williamson-Hall plots of AZO film deposited on textured glass.

Assuming the peak broadening is only caused by crystallite size variation, the integrated grain size can be obtained from linear regression between $\cos\theta$ and β_{hkl} (figure 3.9a). D can then be calculated from the y-intercept ($D=K\lambda/y\text{-intercept}$).

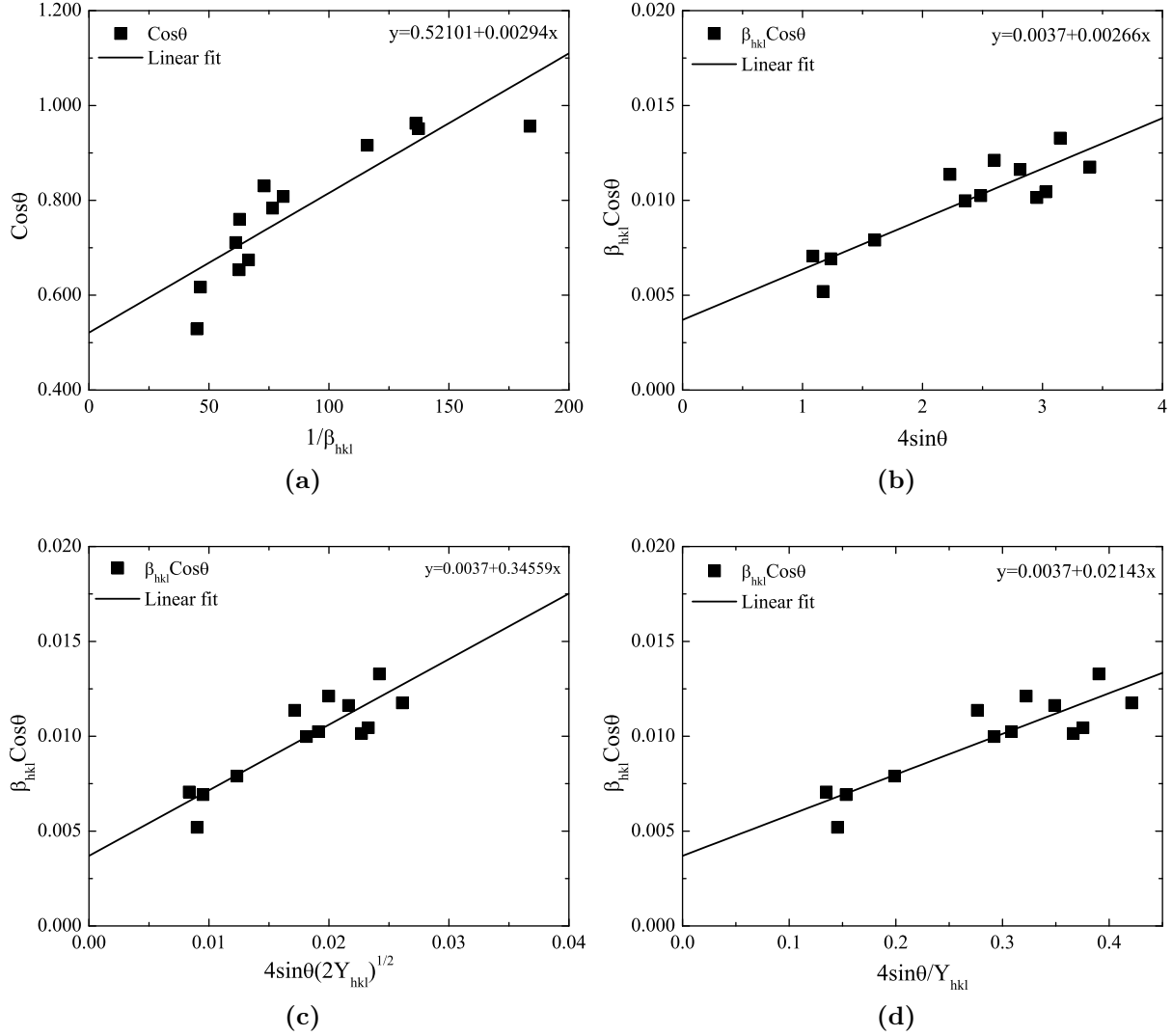


Figure 3.9: Williamson-Hall analysis of (3.9a) crystallite grain size (3.9b) uniform strain, (3.9c) stress and (3.9d) deformation energy

The Investigated AZO films are realised by doping with foreign Al into the ZnO crystal structure. Furthermore, used substrate chemistry and texture are expected to influence the lattice. Thus peak broadening is expected to be influenced by strain. Assuming the strain ε_s is isotropic in all crystallographic orientations,

$$\varepsilon_s = \frac{\beta_s}{4\tan\theta} \Rightarrow \beta_s = \varepsilon_s 4\tan\theta \quad (3.13)$$

β_{hkl} broadening is then given by

$$\beta_{hkl} = \beta_D + \beta_s \quad (3.14)$$

and when rearranged given by the uniform deformation model (UDM) as

$$\beta_{hkl}\cos\theta = \left(\frac{K\lambda}{D}\right) + \varepsilon_s 4\sin\theta. \quad (3.15)$$

The linear regression between the peak width term $\beta_{hkl}\cos\theta$ and strain term $4\sin\theta$ can be used to determine grain size from the y-intercept and the strain ε_s is given by the slope (figure 3.9b).

Assuming the lattice is under stress, a linear relationship between strain ε_s and stress σ_s is given by Young's modulus Y_{hkl} , a generalized Hooke's law

$$Y_{hkl} = \frac{\sigma_s}{\varepsilon_s} \Rightarrow \varepsilon_s = \frac{\sigma_s}{Y_{hkl}}. \quad (3.16)$$

Y_{hkl} is crystal lattice geometry-dependent and its anisotropic nature in hexagonal crystal phase is given by

$$Y_{hkl} = \frac{\left[h^2 + \frac{(h+2k)^2}{3} + \left(\frac{al}{c}\right)^2\right]^2}{S_{11}\left(h^2 + \frac{(h+2k)^2}{3}\right)^2 + S_{33}\left(\frac{al}{c}\right)^4 + (2S_{13} + S_{44})\left(h^2 + \frac{(h+2k)^2}{3}\right)\left(\frac{al}{c}\right)^2} \quad (3.17)$$

where S_{11} , S_{13} , S_{33} , and S_{44} are the elastic compliances of ZnO, and their values are 7.858×10^{-12} , 2.206×10^{-12} , 6.940×10^{-12} , and $23.57 \times 10^{-12} \text{ m}^2\text{N}^{-1}$, respectively [87, 92]. The calculated Y_{hkl} for the planes in the reference ZnO with $a=3.25$ and $c=5.2$ are listed in figure 3.1. The values are comparable to experimentally and empirically determined values in literature for ZnO nanoparticles [87, 92] and AZO films [97].

2θ	31.49	34.06	35.98	47.25	62.52	67.72	72.15	80.99	98.36	103.76
hkl	100	002	101	102	103	200	004	104	114	105
$Y_{hkl} \times 10^{11} [\text{GPa}]$	0.97	1.44	1.28	1.70	1.77	2.44	1.44	1.80	1.60	1.63

Table 3.1: Young's moduli of reference ZnO

Introducing Young's modulus to equation (3.15) results in

$$\beta_{hkl}\cos\theta = \left(\frac{K\lambda}{D_c}\right) + \frac{4\sin\theta\sigma_{hkl}}{Y_{hkl}} \quad (3.18)$$

a uniform deformation stress model (UDSM). The stress is then given by the slope of the linear regression between $\beta_{hkl}\cos\theta$ and $4\sin\theta/Y_{hkl}$. D is determined from the intersect and the strain from the stress the relationship given in equation (3.16).

The UDSM model is a linear approximation that is valid for significantly small strain. Since the extent of the strain on the differently textured substrates is unknown, the strain energy density μ_s (energy per unit volume) was taken into consideration.

Another form of Hooke's law relates the strain to the energy density μ_s by

$$\mu_s = \frac{\varepsilon_s^2 Y_{hkl}}{2} \Rightarrow \varepsilon_s = \sqrt{\frac{2\mu_s}{Y_{hkl}}}. \quad (3.19)$$

Integrating the term into the UDSM model gives the uniform deformation energy density (UDEDM)

$$\beta_{hkl} \cos\theta = \left(\frac{K\lambda}{D} \right) + \left(4 \sin\theta \sqrt{\frac{2\mu_s}{Y_{hkl}}} \right). \quad (3.20)$$

The slope of the linear regression between $\beta_{hkl} \cos\theta$ and $4 \sin\theta (2/Y_{hkl})^{1/2}$ gives the anisotropic energy density μ_s and the y-intercept is used to calculate the crystallite size D . Stress can be calculated from equation (3.19) and strain from equation (3.16) [87, 92].

3.6 EQE and J-V characteristics

The optical and electrical properties used to characterise the solar cells are illustrated in figure 3.10 for pin aSi:H deposited on a flat and textured reference. The flat reference is AZO deposited on flat glass. The textured reference is AZO deposited on flat glass and wet-chemically etched with highly diluted hydrochloric acid (HCl) following deposition.

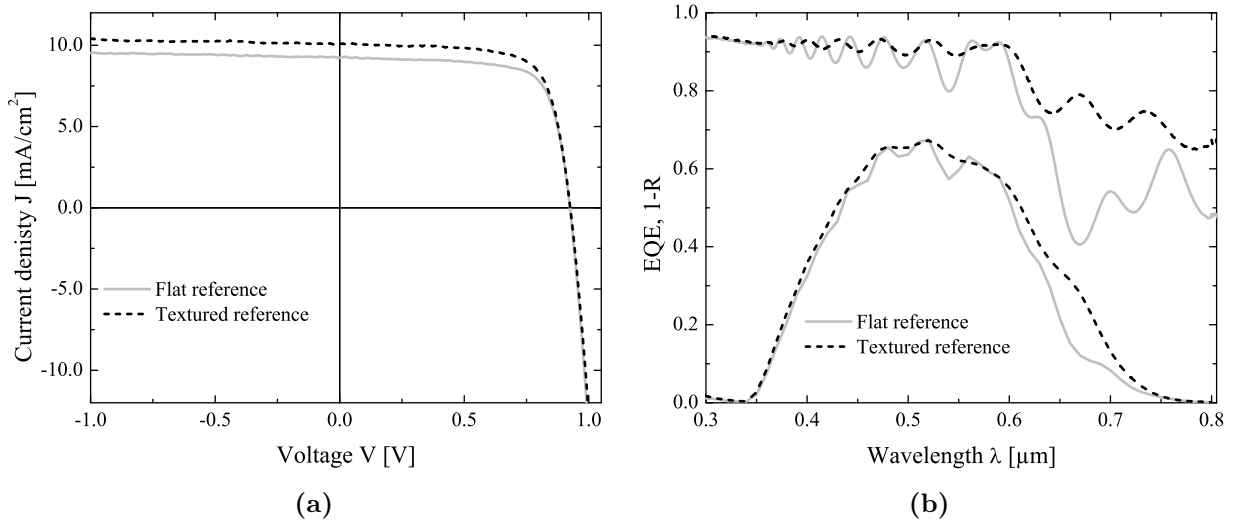


Figure 3.10: J-V-characteristics and EQE of pin aSi:H solar cells deposited on flat and textured reference

Solar cell performance was quantified by comparing J-V characteristics determined on an active area of 1.0 cm² and measured with a WACOM super solar simulator class AAA sun simulator (WACOM dual lamp). The measurements were carried out under the standard test conditions with AM1.5G spectrum referenced using a Fraunhofer ISE solar cell, at 25°C, and 1000 W/m⁻². The spectral response was measured with a RERA System using a halogen lamp.

From the current density (J) and voltage (V) curve (figure 3.10a), the most important characteristics derived to compare the electrical performance of the solar cells are given by

$$J_{SC} = J(V = 0 V) \quad (3.21)$$

$$V_{OC} = V(J = 0 \text{ mA/cm}^2) \quad (3.22)$$

$$FF = \frac{P_{max}}{J_{SC} \cdot V_{OC}} = \frac{J_{mp} \cdot V_{mp}}{J_{SC} \cdot V_{OC}} \quad (3.23)$$

$$\eta = \frac{P_{max}}{P_o} = \frac{J_{SC} \cdot V_{OC} \cdot FF}{P_o} \quad (3.24)$$

where J_{SC} is the short circuit current density, V_{OC} the open circuit voltage, FF the fill factor, P_{max} the maximum power output, J_{mp} the current density, V_{mp} the voltage at maximum power output, P_o the incident radiation and η the efficiency.

Another parameter to determine the optical performance is the spectral response (SR) of the solar cell given by

$$SR(\lambda) = \frac{J_{ph}(\lambda)}{P_0(\lambda)} \quad (3.25)$$

For qualitative measure, the external quantum efficiency (EQE) (figure 3.10b) is derived from SR and indicates the number of charge carriers generated in comparison with the number of incident photons. The relationship is given by

$$EQE(\lambda) = \frac{h \cdot c}{q\lambda} SR(\lambda) \quad (3.26)$$

For a better comparison of the optical losses occurring in the solar cell, EQE is plotted with 1-R, which is the solar cell absorption assuming no transmission occurs. Texturing of the glass used as substrates for the solar cells is discussed in the following Chapter 4.

4 Glass substrates

The literature review showed that textured glass substrates have potential to compete with conventional textured TCO for light trapping. However, the experimental realisation of effectively textured glass substrates remains complex and is a major drawback of the concept. In this Chapter, direct ps laser texturing of multicomponent glass is investigated as an alternative texturing method. A systematic investigation is carried out for laser scribing at varying pulse energy and scribing speed. The morphological modifications are analysed for potential application in silicon thin-film solar cells. For a better understanding of the results, the molecular structure of glass is first briefly outlined.

4.1 Laser texturing of glass substrates

4.1.1 Structure and properties of reference glass substrates

Glass, one of the most abundant and widely investigated materials [74] is extremely complex in nature. It can be considered an amorphous solid with a short-range order of the functional groups [74, 98]. The constituents of glass can be divided into four major groups: glass formers, modifiers, intermediates and fining agents with the following functions [74, 98, 99]. The glass-former provides the basic network in which the other components are accommodated. Silicon oxide (SiO_2) and boric oxide (B_2O_3) are commonly used as this basic structure [74].

Figure 4.1a shows an example of a SiO_2 based glass matrix. The unit cell of the matrix consists of silicon atoms coordinated in a tetrahedral unit surrounded by a variable number of oxygen (4.1a). Adjacent tetrahedra are connected by a common corner O^{2-} ion also termed bridging oxygen (\emptyset). The units neither have common edges nor faces to form a stable structure with a variable angle (α). However, the matrix can also have more than one glass former (e.g. B_2O_3 additionally) and incorporate intermediates such as Al_2O_3 to achieve the desired properties [74, 98–103]. The former and latter are integrated into the basic matrix as demonstrated in figure 4.1a by Al^{3+} and B^{3+} .

This increases the number of non-bridging (O^-) oxygen [100], which interrupts the network and significantly deteriorates other properties. Monovalent cations such as Na^+ or divalent cations such as Ca^{2+} and Mg^{2+} are thus added as modifiers in the form of (earth) alkali oxides to charge-balance Al^{3+} in tetrahedral coordination [98–103]. The cations are located in the interstitials of the basic structure as shown in the two-dimension matrix in figure 4.1b by the Na^+ cation (red). Eventually, fining agents which include NaCl are sometimes added to reduce the amount of air bubbles in the glass [98].

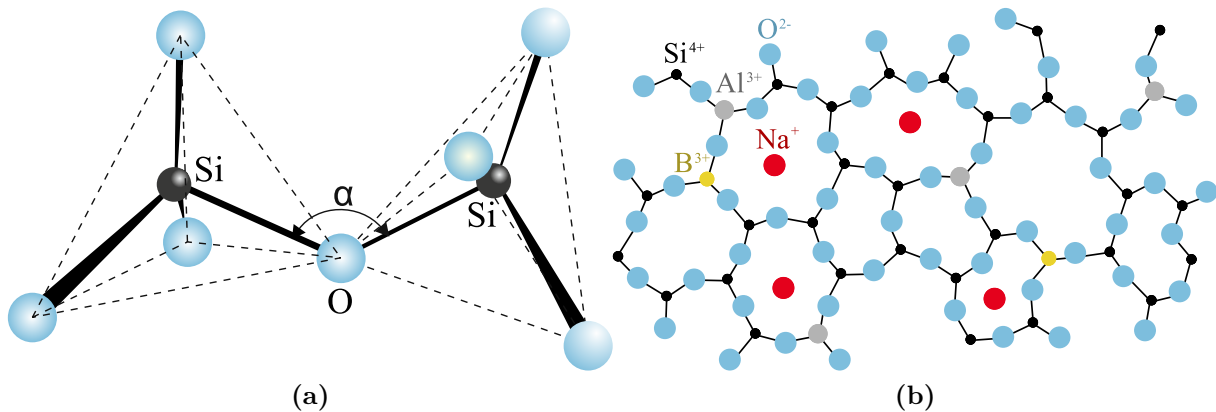


Figure 4.1: Molecular structure (4.1a) of two neighbouring silicon tetrahedra with a common vertex, but statistically varying angle α [74] and (4.1b) an excerpt from a two-dimensional matrix of an alkali aluminoborosilicate [103]

Depending on the compositions, glass can be divided into three main groups; soda-lime (e.g SiO_2 , Na_2O , CaO , Al_2O_3), borosilicate (e.g SiO_2 , B_2O_3 , Na_2O , Al_2O_3) and lead glass (e.g SiO_2 , PbO , K_2O) which all have different properties [74, 75, 98–105]. These properties include thermal conductivity (κ), density (ρ) and specific heat capacity (C_p) shown in table 4.1 for two aluminoborosilicate glass, one containing alkaline (Type I), the other earth alkali (Type II) and a soda-lime (Type III) glass.

Sample name	Type	Manufacturer	d	κ	ρ	C_p
			mm	W/(m·K)	kg/m ³	J/(kg·K)
Type I	alkali borosilicate	Schott Borofloat 33 [103]	2.0	1.2	2380	830
Type II	earth alkali borosilicate	Corning Eagle XG [106]	1.5	1.22	2500	896
Type III	soda-lime	Saint Gobain SGG [107]	3.0	0.8	2200	800

Table 4.1: Thicknesses and thermophysical properties of the investigated glass substrates

These substrates were investigated and their reference optical properties are illustrated in figure 4.2. The total transmission (4.2a) and refractive index (4.2b) showed how the dispersion was also composition-dependent. Pure SiO_2 (fused silica) has a high band gap of 9 eV in the ultraviolet region [108].

Figure 4.2a (excerpt) shows the transmission of fused silica [74]. The different additives shift the absorption edges to longer wavelengths e.g ~ 4 eV [109]. Slight discrepancies in the transparency were observed in different batches of the same type of glass. As a matter of fact, the illustrated data shows the most commonly observed trends in the NIR as well as the UV region (magnification).

The different glass substrate compositions were also expected to influence the textured profiles as a consequence of the different laser-dielectric material interaction. This aspect is elaborated in the following section.

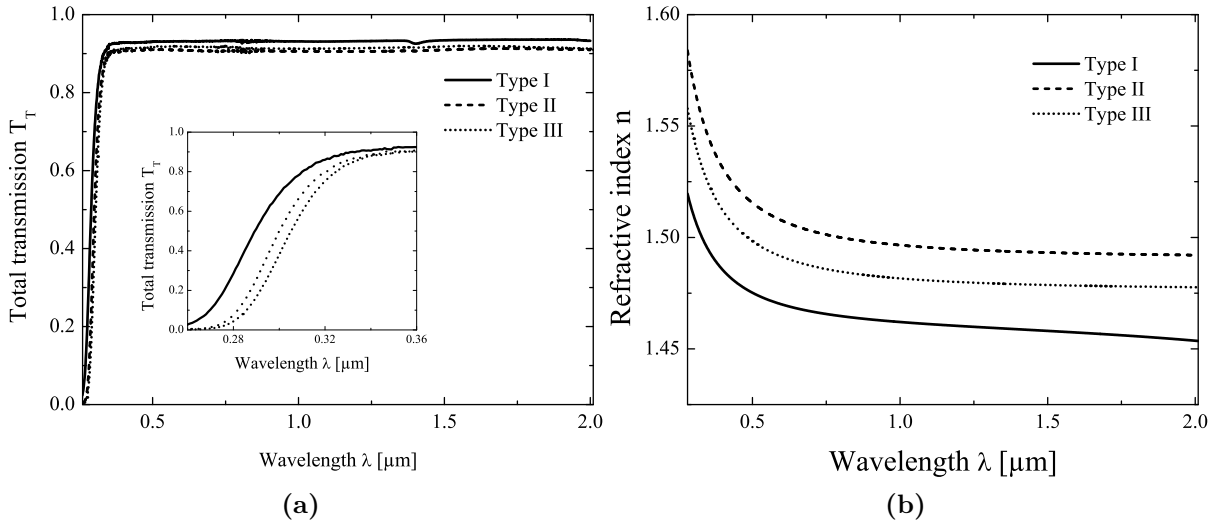


Figure 4.2: Reference (4.2a) transmission with a detailed excerpt in the UV-region of fused silica [74] and (4.2b) refractive index of Type I, Type II and Type III.

4.1.2 Laser and dielectric material interaction

Laser induced phenomena in target material are dependent on properties of both material and laser irradiation [110–113]. Material properties include the band structure, electron mobility and recombination rate [111]. The laser parameters include profile (Gaussian, step etc.), focused beam area (A_{ω_0}), pulse duration (τ) and pulse energy (E_p) [111]. During the interaction period, which is the pulse duration τ , (I) carrier excitation, (II) thermalisation, (III) carrier removal and (IV) thermal and structural effects occur consecutively on the time-scale [112]. These are elaborated for transparent dielectric materials such as the investigated glass substrates textured with $\tau \lesssim 10$ ps and laser wavelength $\lambda_{ps} = 1064$ nm in the following.

The investigated glass substrates were transparent for the laser wavelength used (figure 4.2a). Material removal is determined by the local inertial confinement [112], which is induced by the focused laser beam scanned on the substrate surface with a galvanometric head. The first process (I) carrier excitation is induced by non-linear absorption mechanisms, which require minimum energy. This minimum energy required to initiate ablation is defined as the texturing threshold energy (E_{th}), which also depends on the pulse duration. The relationship between τ and E_{th} determines the ablation mechanisms, which are distinguished into long pulse durations ($\tau > 10$ ps) and short pulse ($\tau < 10$ ps) regimes [109, 110, 112, 114].

For $\tau > 10$ ps, the texturing in dielectrics is induced by thermal excitation of the initial electron by the incident radiation. Subsequently, this energy is transferred to the lattice in the (II) thermalisation process. This is followed by (III) carrier removal where Auger recombination, additive recombination and carrier diffusion occur. The radiation time of the pulse is high enough for the excitation process to overcome the recombination

processes. Consequently, texturing occurs due to (IV) melting and boiling of the exposed region [114]. Thus, E_{th} is dependent on the rate of thermal conduction through the lattice by $\tau^{1/2}$ [109, 114].

Ablation in the short pulse regime ($\tau < 10$ ps) is a non-thermal process induced by multi-photon ionization (MPI) [114]. High intensity ultra-short pulse cause the excitation of the initial electron through mechanisms such MPI above the band-gap. Before complete relaxation, the electron is excited by a subsequent photon and ionizes other electrons, which initiates a cascade. The result of the ionization is a high electron density, which reaches saturation at the critical electron density (ρ_{cri}) where the plasma frequency is equal to the wavelength of the laser. The dielectric material thus behaves like a conductor and can absorb the laser energy [114].

At this point, which is above E_{th} , the material deteriorates due to the high electrostatic forces and the plume is ejected [109, 110, 114]. Both texturing mechanisms result in a crater with a structurally modified region, which has been observed for scribing with picosecond (ps) and femtosecond (fs) laser [56, 110, 113–116]. In this investigation, the ps laser pulse duration was $\tau = 8.5$ ps. Thus both thermal- and non-thermal processes are expected.

4.1.3 Topology of laser-textured glass substrates

The texturing degree was manipulated by changing the laser spot overlap (LSO), which defines the percentage of the spot diameter overlapping on the surface. To be able to tune the overlap specifically, information about the focused Gaussian laser spot diameter (ω_0) on the substrate is necessary. This was obtained from texturing series at constant speed (3000 mm/s), but varying pulse energy as described for Type II glass in the following.

Laser spot diameter determination Substrates were placed on the sample stage with the surface in the focused beam. An initial average laser power (P_p) of 11.5 W was measured. The pulse energy (E_p) is related to P_p by equation (4.1)[117]

$$E_p = \frac{P_p}{f} \quad (4.1)$$

where f is the laser repetition rate ($f = 100$ kHz). The pulse energy was set to a constant value and a row of isolated crater was ablated at 3000 mm/s. The energy was then decreased by attenuating the beam and a new row was scribed. This step was repeated until the energy was too low to initiate ablation. The isolated crater dimensions were measured with AFM. Cross sections of the crater obtained at different pulse energies are shown in figure 4.3a.

The results demonstrated that the textured crater diameter is reduced with decreasing energy. Furthermore, the profile was gradually changed from a rather step-function to a

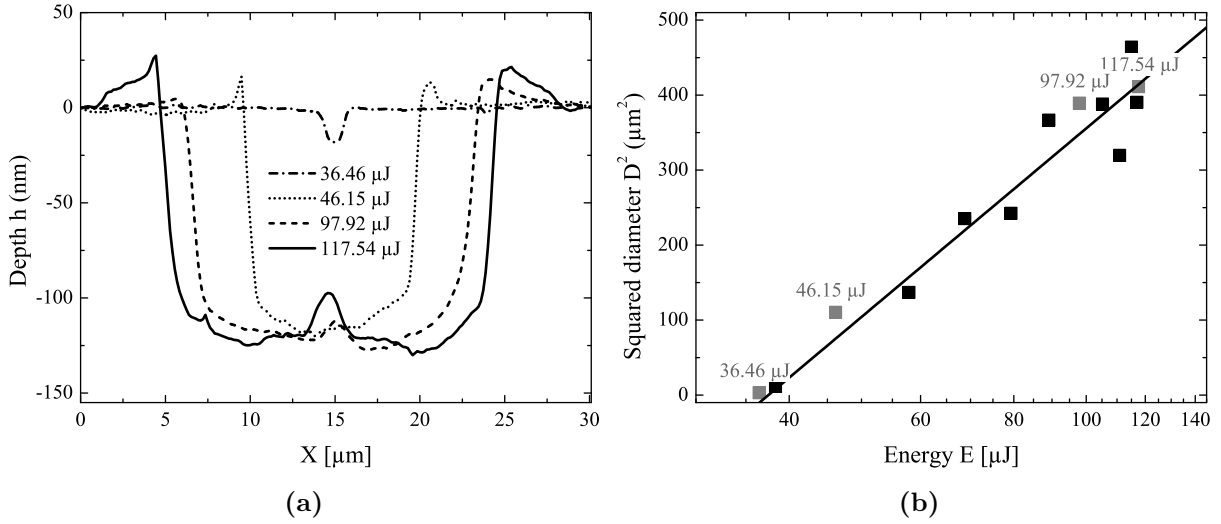


Figure 4.3: (4.3a) The cross-section used to determine the Gaussian profile diameter ω_0 on the substrate surface following ablation and (4.3b) the linear regression used to determine the threshold energy

Gaussian profile (figure 4.3a 117.54 μJ vs. 36.46 μJ). A linear regression between the square of the crater diameter and the logarithm of the laser energy was then used to determine ω_0 as elaborated in Ref. [109] and given by equation (4.2)

$$D^2 = 2\omega_0^2 \ln \left(\frac{E_p}{E_{th}} \right) \quad (4.2)$$

where D is the measured crater diameter and E_{th} the threshold energy. E_{th} is given by the x-intercept of the regression line where $D^2=0 \mu\text{m}$. Figure 4.3b shows this linear regression from which a texturing threshold of $E_{th}=28 \mu\text{J}$ was determined, which is comparable with results in other studies [118]. The laser spot diameter ω_0 was assessed to be $19.5 \mu\text{m}$.

Laser spot overlap (LSO) With this information, the degree of periodicity can directly be changed by adjusting the laser spot overlap (LSO) pattern on the surface. This was achieved by adjusting the scribing speed (ν_{max}) and alignment of adjacent lines. The relationship between the LSO and ν_{max} is given by equation (4.3)[25]

$$\nu_{max} = (f\omega_0)(1 - LSO) \quad (4.3)$$

As an example, a $\nu_{max}=1000 \text{ mm/s}$ is required for the repetition rate $f=100 \text{ kHz}$ and $\omega_0 \approx 20 \mu\text{m}$ to achieve a 50% laser spot overlap in the scribing direction. The overlap must also be taken into consideration in the adjacent line.

Schematic diagram in figure 4.4 shows how this was carried out with the galvo-head scanner. The LSO on the surface was first initiated in the scanning direction (X). A subsequent line in the Y-direction was overlapped with the same LSO. In addition, the position of the initial spot in the adjacent line further influences the pattern.

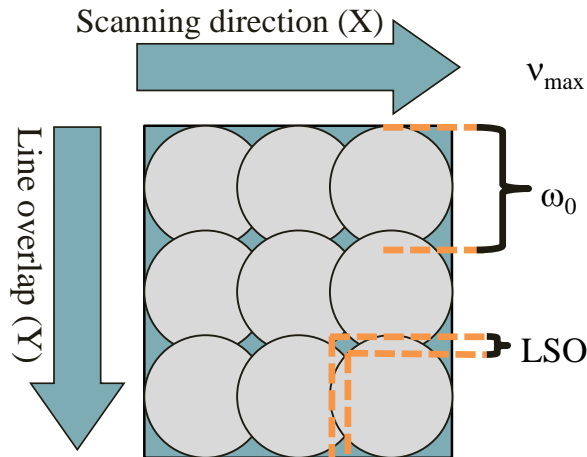


Figure 4.4: Schematic diagram showing the spot overlap in the X- and Y- direction on the substrate surface. The spots in the subsequent lines are aligned vertically to a cubic close-packed array.

In the illustrated example, the spots in the subsequent lines are aligned vertically and the arrangement resembles a cubic close-packed array with overlap. Alternatively, with sufficient horizontal displacement of the adjacent lines, a hexagonal close-packed array can be obtained. Small areas of $0.5 \text{ cm} \times 0.5 \text{ cm}$ were processed with a scribing speed starting from a high scribing speed of 6000 mm/s and gradually decreasing in 100 mm/s steps until 200 mm/s . Given the $\approx 20 \mu\text{m}$ spot diameter, an isolated laser spot pattern (-LSO) prevailed until 2000 mm/s where an overlap (+LSO) was gradually achieved with decreasing scribing speed.

Isolated crater dimensions Several studies have demonstrated that both periodic [45] and random [16] textures reduce the total reflection, increase the light scattering and thus enhance the short-circuit current density in solar cells. Arranging the Gaussian profiled craters in figure 4.3a with a diameter of approximately $2.5 \mu\text{m}$ in a cubic or hexagonal close-packed [119] array could have similar advantages. An attempt to scribe these craters however resulted in inhomogeneous and irreproducible textured surfaces. One possible explanation for the observed inhomogeneity was the low scribing energy close to the threshold, where the slightest fluctuation in the spot profile, glass composition or surface height is detrimental.

Thus, a much higher energy, which delivered larger craters as demonstrated in figure 4.3a was used. The crater dimensions ablated with high $\nu_{max}=3000 \text{ mm/s}$ to avoid overlap and constant $E_p=115 \mu\text{J}$ are shown in table 4.2 for the different glass substrates. Type I showed craters with a higher aspect ratio in comparison to Type II and Type III. Type III, on the other hand, demonstrated the shallowest and widest crater. As already mentioned, the texturing induced changes are substrate- and laser-dependent. Scribing was carried out under the same conditions, (focused) laser-spot to sample distance and the laser parameters were kept constant. The observed differences in behaviour were

therefore attributed to the glass composition.

	D	h		τ_c	ρ_p	τ_l
	μm	nm		fs	$\times 10^{19} \text{ cm}^{-3}$	ps
Type I	18.98±0.49	276.69±13.74	K9 [120]	2.8	7.0	6.6 103
Type II	21.54±0.66	140.70±7.13				
Type III	24.78±2.29	136.85±9.5	Soda-lime [120]	1.83	6.0	4.3 113

Table 4.2: Isolated crater dimensions textured at high scribing speed $\nu_{max}=3000$ mm/s and pulse energy $E_p=115\mu\text{J}$ measured on the surface of the different glass substrates. Literature values for electron collision time τ_c , electron plasma density ρ_p and electron life time τ_l [120].

Several studies have suggested the critical electron density (ρ_{cri}) as the texturing criterion to predict the textured crater dimensions in dielectric material [110, 116, 121, 122]. The texturing depth is assumed to be the maximum depth where the free electron density reaches the ρ_{cri} [116, 122]. Numerical models based on this assumption are capable of simulating the laser beam propagation and electron dynamics [116, 122]. For the beam propagation, the damping constant (χ) of harmonic oscillators used is considered to be the reciprocal of the electron collision time [110, 116, 121, 122]. Electron dynamics used to simulate the temporal evolution of the electron density ρ in the conduction band are given by the rate equation [122]

$$\frac{\partial \rho}{\partial t} = \sigma I^k + \alpha_c I \rho - \eta_{rec} \rho^2 - \eta_{diff} \rho \quad (4.4)$$

where the multi-photon ionization rate, cascade ionization rate, recombination rate and diffusion rate are given by the terms on the right, respectively. The respective variables I^k and I are the intensities and σ , α_c , η_{rec} and η_{diff} the coefficients. The cascade ionization coefficient (α_c) is dependent on the electron-electron collision time amongst other variables [122].

This approach indicates that the recombination rate of the electrons and the collision time influence the dimensions of the textured crater. Quan et al. determined fs pulse induced electron collision times in K9 borosilicate and soda-lime glass experimentally [120]. The values are summarized in table 4.2 where life times determined at the beginning and towards the end of the pulse duration are both shown.

Type II and Type I are assumed to behave similar to K9 and Type III similar to the soda-lime glass studied Quan et al. [120]. Sun et al. show in numerical modelling that crater width and depth decreases with increasing collision time since the ionization rate is decreased [122]. An agreement in the change of the width of the crater was found, but not the depth of the crater. Type I showed the narrowest crater diameter followed by Type II and Type III.

Increasing recombination coefficient resulting in an increased loss rate is also suggested to result in a decreased crater width and depth [122]. Here, consistency is found in the

depth of the crater, but not the width. Type III delivers the shallowest depth followed by Type II and Type I. Considering the calculated errors, crater profiles of Type II and Type III were similar. This correlated with the observed transmission trend in figure 4.2a.

Furthermore, observed crater in Type III had a flat-bottom compared to the crater in the borosilicate glass substrates. Jiang et al. attribute this shape to an increased reflectivity and absorption coefficient of the generated plasma [121], which might also explain the shallow features. Additionally, a higher damping constant resulting from the reciprocal of the collision time might lead to a reduced penetration and thus explain the shallow depth.

Periodic and random textured surface The observed differences in the dimensions of the isolated crater were also evident in increasingly random textures. By decreasing the scribing speed at constant pulse energy, the obtained surface texture was changed from periodic to random. The topologies obtained at different scribing speeds are illustrated by the AFM images in figure 4.5.

A white high reflecting powder was observed for very low scribing speeds $\nu_{max} \leq 1000$ mm/s. Several studies report nano-particles debris forming around the crater [112, 123, 124] is from plasma plume resolidifying onto the substrate. By applying a strong mechanical cleaning process, the powder could be removed.

Another interesting observation was the evolution of steep crater (isolated dark regions) at points of multiple overlap and peaks following a high spot overlap. Precise knowledge of the nature of these outliers is of great importance for the quality of subsequently deposited layers. For one, steep regions might lead to empty voids following TCO deposition, which affects the stability of the front contact. Peaks might cause short-circuit currents if the solar cell layers deposited are much thinner than the texture height. Such negative effects are detrimental for the application in thin-film solar cells. Similarly, particular textures might favour the growth of TCO, which might have a positive effect on the solar cell performance.

In either case, statistical analysis of the surface texture distribution is an important and helpful tool to assess these aspects (see Chapter 3, section 3.2 for detailed theory). The surface roughness σ_{rms} gradually increased with rising scribing speed and the height profile reached the micrometre range. The autocorrelation length (ACL) and skewness (Ssk) of the texture are illustrated in figure 4.6. ACL (4.6a) decreased with increasing scribing speed, demonstrating the evolution of smaller features.

The results suggested that the texture remained in the micron range (minimum ACL) which might however be limited by the scanning resolution. This might be particularly the case for Type II where lower ACL was than the observed values for $\nu_{max} \leq 2000$ mm/s. It should also be noted that the initial ACL (untextured reference glass) was expected to be much higher and the observed results were attributed to the bulging surface and

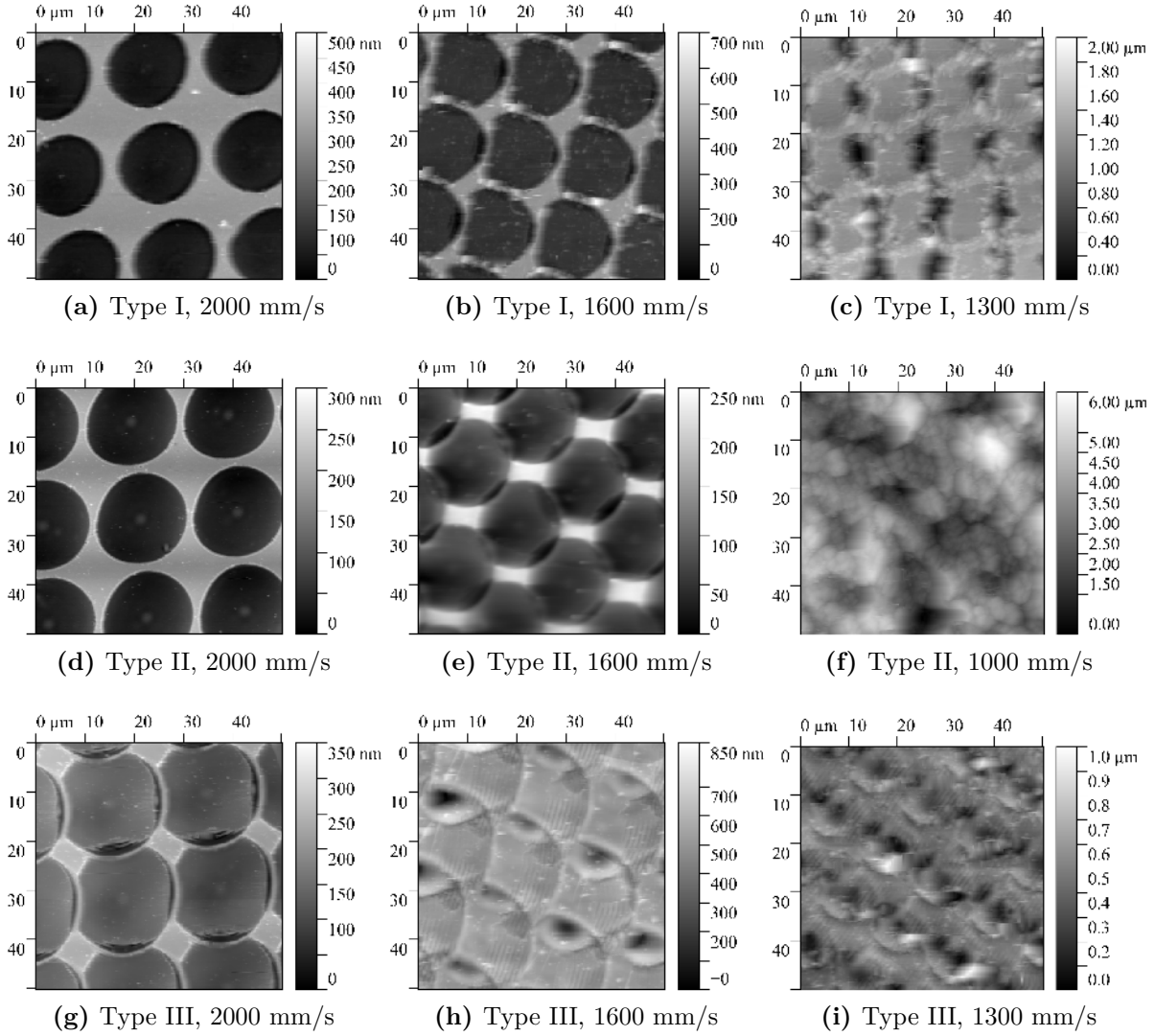


Figure 4.5: Atomic force microscopy images of Type I (4.5a-4.5c), II (4.5d-4.5f) and III (4.5g-4.5i) textured at the scribing speed 2000 mm/s, 1600 mm/s, 1300 mm/s (1000 mm/s for Type II), respectively. Laser parameters used were pulse length $\tau_{ps}=8.5$ ps, laser wavelength $\lambda_{ps}=1064$ nm, Gaussian laser spot diameter $\omega_0=19.5$ μm and pulse energy $E_p=115$ μJ

presence of foreign particles such as dust on the surface. In theory, ACL converges into infinity for a perfectly smooth surface.

The texturing degrees observed were distinguished between $\text{LSO} \ll 0\%$, $\text{LSO} \approx 0\%$ and $\text{LSO} \gg 0\%$. Skewness S_{sk} of the differently textured substrates is shown in figure 4.6b. The observed elevations in the untextured flat reference were attributed to surface bulging and foreign particles on the surface. The transition between the texturing degrees was glass-composition dependant and shifted to higher ν_{max} from Type I, II to III.

The AFM images in figure 4.6b compare the topologies of Type I, Type II and Type III scribed at 2500 mm/s. Type III crater showed a slight overlap while Type I and Type II crater were still isolated. The high scribing speeds ($\text{LSO} < 0\%$) delivered surfaces predominantly accommodating plateaus with a few craters and thus $S_{sk} < 0$. With decreasing

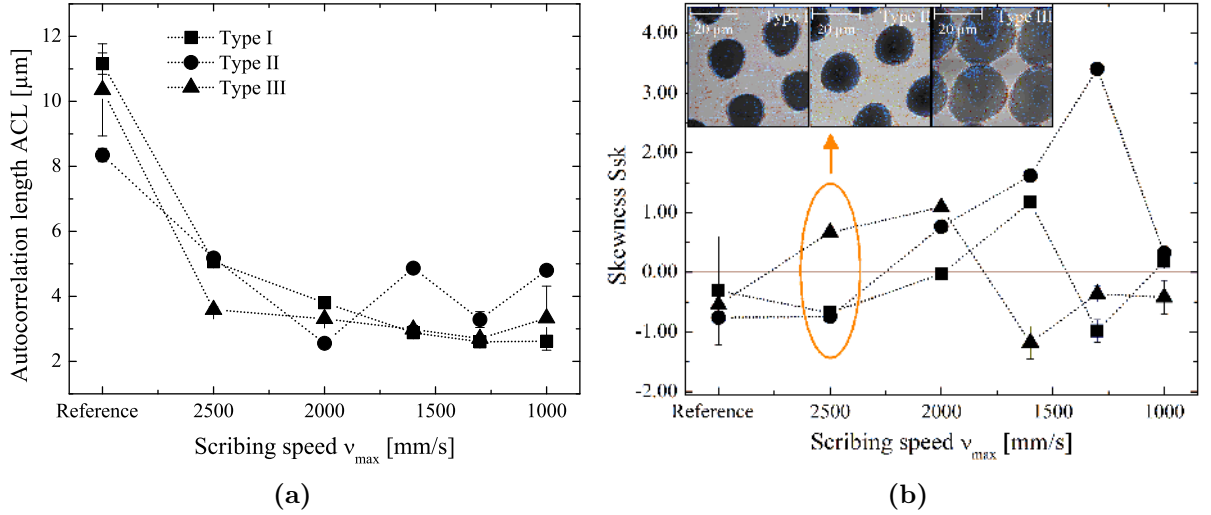


Figure 4.6: Statistical analysis of the topology following texturing with varying scribing speed at constant pulse energy with (4.6a) the surface autocorrelation length (ACL) and (4.6b) skewness (Ssk) depicting the structural evolution from periodic to random surface.

v_{max} , the ratio between untextured plateau/crater decreased and the height distribution approaches $Ssk \approx 0$. Around transition to overlapping crater, peak formation was observed $Ssk > 0$. The peaks were therefore a mixture of untreated and treated regions, which were not completely removed.

With increasing LSO, peaks disappeared and steeper narrower valleys at sites of overlap occurred. In turn, high overlap resulted in a completely treated surface and the valleys from multiple overlap $Ssk < 0$. Consequently, steep isolated valleys were observed and their origins can be explained as follows. After a single spot texturing with sufficient energy, a layer around the crater is modified. Subsequently, the following overlapping spot partially encounters structurally modified material, with different properties [110, 122, 123] along with parasitic debris absorption. The texturing threshold is decreased and the material can be easily removed. Steep crater as demonstrated in figure 4.5 (4.5c, 4.5h and 4.5i) by the dark regions can then eventually occur. However, these also depend on other factors such as material homogeneity.

heat-affected Zone (HAZ) This region in the bulk material is prone to structural changes [110, 115, 124]. The structural modification around the textured crater affects the bulk material and the surface morphology. This was indicated by the computed AFM average tip oscillation phase shift measured within the crater and untreated material as demonstrated in figure 4.7. The phase shift image of Type III textured with $v_{max} = 3000$ mm/s and $E_p = 115 \mu\text{J}$ (table 4.2) is shown in figure 4.7a to clarify the difference.

Figure 4.7b shows that the averaged phase shift gradually increased with decreasing scribing speed and was more intense for Type I followed by III and II. The results showed that the phase shift variation was also glass substrate composition-dependent and more

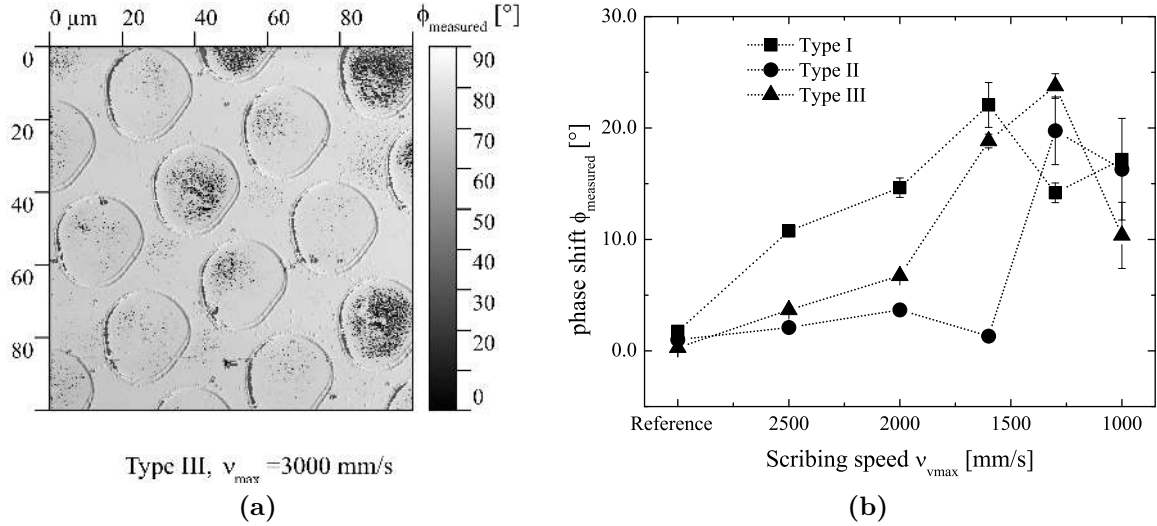


Figure 4.7: Phase contrast image of (4.7a) Type III scribed at a speed of $v_{max}=3000$ mm/s, pulse energy $E_p=115$ μJ and (4.7b) the corresponding averaged phase shift measured for Type I, II and III following texturing with varying scribing speed

profound in Type I.

Increased and decreasing phase shifts when probing an inhomogeneous substrate are attributed to increasing and decreasing stiffness of the material, respectively [125, 126]. Stiffer materials show a lower thermal expansion coefficient. Moreover, higher mismatch in the linear thermal expansion coefficients between film and substrate increases the thermal strain component in the film. Therefore, the phase shift results suggested that the stiffness in Type I was higher in comparison to Type II and II and that the stiffness increased with decreasing scribing speed.

The different chemical compositions of the substrates also determine further glass properties including thermal capacity (κ), density (ρ) and specific heat capacity (C_p) which are shown in table 4.1. These parameters influence the thermal diffusion length (L), which can be calculated for one dimension by

$$L = \sqrt{\frac{\kappa\tau}{\rho C_p}} \quad (4.5)$$

The thermal diffusion length is a measure of the distance across which the temperature propagates in a given period of time (τ), which can be considered the pulse duration [110, 124] (in this case 8.5 ps). L is thus a measure of how far the energy is dissipated.

For the three glass types, a diffusion length of 2.36 nm, 2.21 nm and 1.84 nm was calculated for Type I, II and Type III, respectively. The length of the affected region is similar, considering the used properties were taken from literature [103, 106, 107]. Note that L is calculated with the specified properties for temperatures $\leq 100^\circ\text{C}$. Since significantly higher temperatures are present during laser ablation [124], higher diffusion depths can be expected.

The elevated regions around the crater indicate the glass is molten. The melting temperature of borosilicate glass is reported to be around ≈ 1500 K [115]. During scribing, temperatures as high as $\geq 900^\circ\text{C}$ are therefore probable in the HAZ [115]. The energy dissipation is continued post pulse duration. Combined effects of the initial and post energy transfer can lead to material changes in the heat-affected zone (HAZ)[110].

4.1.4 UV-VIS optical properties

Both the morphological and topological changes influence the optical properties of the textured substrates. The surface area resulting from periodic and random roughness is increased and enhances light in-coupling along with the introduced light scattering. The morphological variation is also expected to influence the amount of light attenuated. The former and the latter aspects are important for the application in thin-film solar cells and are therefore analysed and discussed in the following.

Light scattering The textured surfaces became milky with decreasing scribing speed, which indicates an enhancement in light scattering. The diffuse transmission and thus haze of these substrates increased. It should be clarified that this trend was also observed after mechanical cleaning of the substrates.

Figure 4.8 shows the corresponding angular resolved intensity ADI. To be able to compare the three glass types in an overview, only the scattering at the wavelength 700 nm is shown for substrates textured at the scribing speeds 2000 mm/s and 1000 mm/s. Introducing a slight texture on the surface (figure 4.5a, 4.5d and 4.5g) enhanced the diffraction into greater angles slightly, in comparison to the reference.

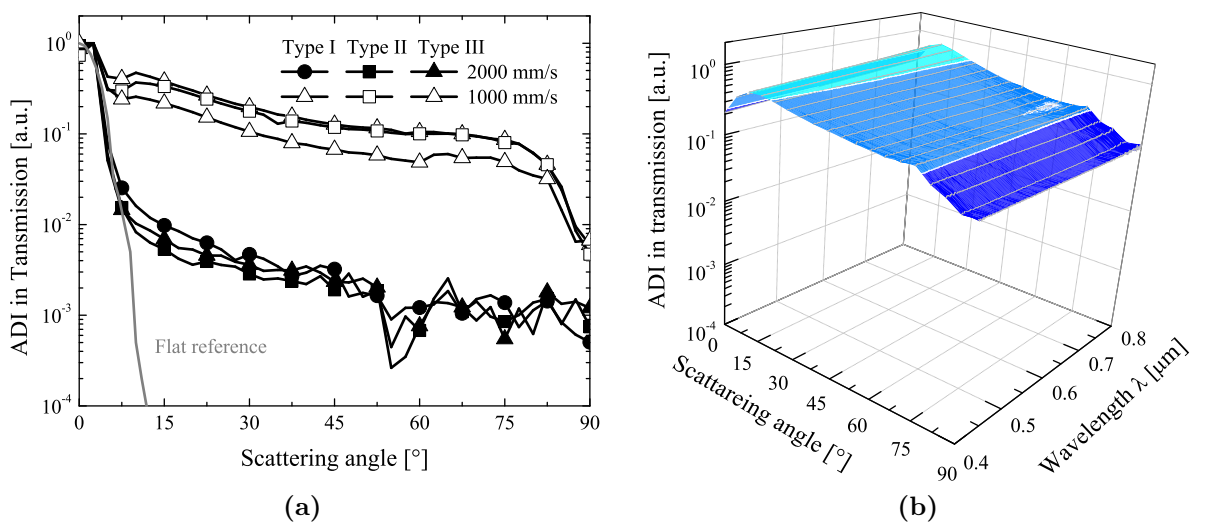


Figure 4.8: Angular resolved scattered intensity (4.8a) at 700 nm wavelengths of Type I, II and III textured with a pulse energy $E_p=115 \mu\text{J}$ and scribing speed of $\nu_{max}=2000$ mm/s and 1000 mm/s respectively. (4.8b) ADI of Type II scribed at $\nu_{max}=1000$ mm/s respectively.

Given the crater diameters, this was attributed to geometric optics in the overlapping regions. Furthermore, the elevated rims around crater might contribute to the observed scattering. The 1000 mm/s samples on the other hand demonstrated high scattering intensities in angles up to 80° .

Type III showed a slightly lower intensity throughout all the scattering angles. Scattering behaviour in Type III was attributed to shallower features compared to Type I and Type II. High scattering intensity of the very rough surface was attributed to multi-fold of dimensions resulting from the high laser spot overlap. The textures thus demonstrate broadband light scattering as shown for Type II (right), which is an important and desired aspect for light in-coupling in silicon thin-film solar cells.

Transmission, Absorption and Reflections Another important aspect is the intensity of light reaching the absorber material in the solar cell following reflection and absorption in other layers. Figure 4.9 demonstrates that the total transmission (4.9a) of Type II gradually decreased and the absorption (4.9b) increased with decreasing scribing speed from 2600-400 mm/s. This corresponds to increasing LSO from -30 to +80%. A similar trend was observed in Type I and Type III, with changes being more profound in Type II.

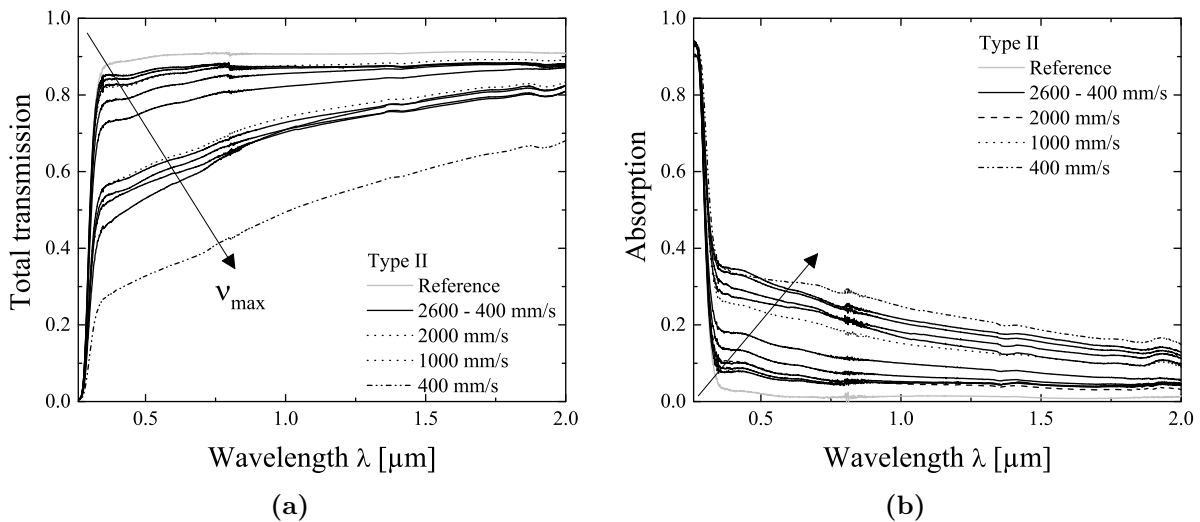


Figure 4.9: (4.9a) Transmission and (4.9b) absorption spectra of Type II substrates textured with a pulse energy $E_p=115 \mu\text{J}$ and varying scribing speed of ν_{max} between 2600-400 mm/s

The observed absorption was rather high. Loss in transmission near the ultra violet region is attributed to trapped electrons in soda silicate exposed to ionizing radiation [127]. Another possible explanation might be measurement artefacts. In particular, the substrates were measured in the arrangement air/glass/texture/air. According to Snell's law, light propagating from dense to less dense medium is diffracted away from normal incidence [128]. Highly textured substrates additionally scatter the light strongly so that

multiple reflections occur on the substrates surface, resulting in an increased absorption.

Laser-induced refractive index variation Highly textured substrates showed increased reflection. The reflection of periodically textured substrates reduced. It is possible that a different mechanism is responsible for this behaviour. Reflectivity is dependent on the dispersion relation of the bulk material. A change in the refractive index (Δn) might be a possible explanation for the increased reflection. The relationship between reflection and refractive index (n) at a perpendicular incident is given by [128]

$$R = \frac{(n_{air} - n_{glass})^2}{(n_{air} + n_{glass})^2} \quad (4.6)$$

The refractive index can be measured by ellipsometer spectroscopy. The fundamental of technique includes the detection and interpretation of phase information of polarised light reflected from a sample [69]. Textured substrates with an optically rough surface (e.g. samples textured at 1000 mm/s) cause great errors in measurements because they scatter and depolarize the light [69]. Hence, only the refractive index variation of slightly textured substrates ($\nu_{max}=3000$ mm/s), where coherent light propagated following reflection, were analysed. Substrates were illuminated with a micro-spot beam of the textured side. Optical constants were fitted from transmission, reflection and ellipsometer data measurements. The surface texture with the heights 297, 141 and 137 nm in Type I, Type III and Type III was considered to be a separate layer, respectively.

The deduced refractive index modifications are shown in figure 4.10. The refractive index of the reference ($n_{initial}$) increased in Type I and III and decreased in Type II following laser ablation ($n_{textured}$). The observed behaviour might be caused by different mechanisms resulting from the rearrangement of different structural units [56]. The extent of the change $\Delta n = n_{initial} - n_{textured}$ was wavelength and glass composition-dependent.

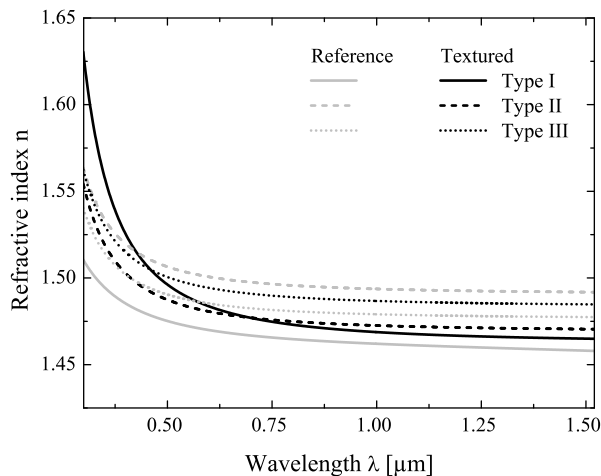


Figure 4.10: Refractive index change in Type I, II and II following texturing with a pulse energy $E_p=115$ μ J and scribing speed of $\nu_{max}=3000$ mm/s. Ellipsometer measurements were fitted with spectrometer transmission and reflection data assuming the surface texture to be a separate layer.

In the (N)IR region, the difference approached a constant value. The maximum Δn observed in the different glass types was 0.16, -0.02 and 0.02 in Type I, Type II and Type III, respectively. The results, particularly, of Type II and III were comparable with values reported by Chan. et al. [118]. At lower pulse energies, changes in the range of ± 0.005 [56] are reported for borosilicate glass. Studies also report on refractive index change of magnitude 10^{-4} to 10^{-3} [118, 129–131]. For higher fluences $F_p=40 \text{ Jcm}^{-2}$, refractive index change one magnitude higher (0.05) is assumed [118].

The observed modification in Type I was a magnitude higher than the values reported in literature [56, 118]. This might result from defect [127], stress [130] and significant structural rearrangements [56] at such high texturing energy used. Thus modifications in randomly textured substrates were expected to be even higher. Limited optical characterisation techniques to assess refractive index in optically rough surface make it difficult to deduce this variation. A numerical approach was thus taken to model and calculate the influence of hypothetically high refractive index on the reflection and light in-coupling in thin-film solar cells and is discussed in the following section.

4.2 Simulation of refractive index variation

The refractive index of Type I and III glass substrates increased and Type II decreased following ablation. Limited optical characterisation methods for optically rough surfaces made it difficult to characterise the changes in highly textured substrates. The refractive index change in glass substrates can influence the performance of solar cells negatively or positively. Sufficient knowledge of its extent and its influence on the reflection and transmission might however make it possible to exploit the effect to enhance light in-coupling. Quantification and prediction of possible drawbacks are furthermore necessary for weighing whether further experimental investigations are required to understand the structural modifications in order to find means of mitigating them. Simulations were therefore carried out to assess the potential of the modified refractive index at the glass/AZO interface.

4.2.1 Simulation domain

The software Sentaurus TCAD developed by Synopsis was used for 2D finite-difference-time-domain (FDA) method numerical modelling [132] with the approach validated by Lacombe et al. [133]. Figure 4.11 shows the simulation domains of the layer stacks investigated in this study. 2D simulations were carried out for the spectral region 300-800 nm for the layer stack shown in figure 4.11. The layer stack consisted of glass (200 nm), AZO (800 nm) and i-aSi:H ($3 \mu\text{m}$). The optical constants of the films determined from experiment [134] were used as input parameters.

The planes were inserted as demonstrated in the 2D cross section in figure 7.1b to detect the transmitted (T) and reflected (R) amplitude. The excitation plane was placed

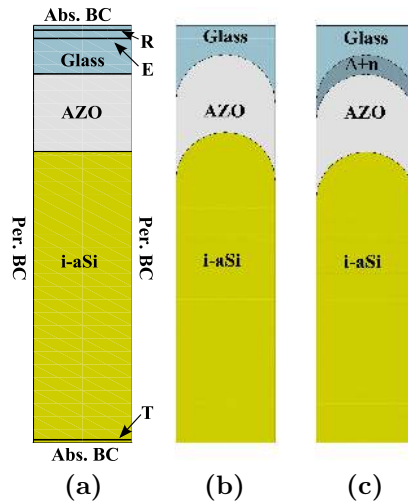


Figure 4.11: 2D simulation domain of the solar cell layer stack glass/texture/ $(\pm\Delta n)$ /AZO/i-aSi:H on (4.11a) a flat reference showing the reflection (R), excitation (E), transmission (T) planes, periodic (per.) and absorbing (abs.) boundary conditions (BC). Simulation domain of a textured substrate with (4.11b) rounded crater texture and (4.11c) modified $\pm\Delta n$ region on the glass surface.

within the glass substrate to deliver an electromagnetic field (E) source. Absorption in the glass was therefore neglected, and a constant 4% reflection was assumed for the air/glass interface. Periodic (per.) boundary conditions (BCs) were assumed for the vertical sides of the structure and absorbing (abs.) for the horizontal. A coherent, monochromatic harmonic, plane electromagnetic wave with a wavelength λ was applied at normal incidence. The AM1.5G spectrum was used for both EQE and reflection simulations, and kept constant at 1000 W/m^2 for the AID simulations.

The aSi:H i-layer was intentionally thick to effectively absorb the wavelengths, particularly in the NIR region with a high penetration depth. Experimentally obtained dispersion data of Type I was used as input parameters for the glass substrates in the simulations. The layer stack configuration (without a back contact) allowed a better comparison of the reflection at the glass/AZO and AZO/aSi interfaces between the reference and the textured substrates. Periodic textures, rounded (4.11b) and Gaussian crater similar to those observed in the AFM measurements (Chapter 4, Section 4.1.3) were investigated. The crater diameter of 2-20 μm was reduced to 1 μm , mainly due to limited simulation capacity and because this dimension is suggested to deliver an effective light scattering [45].

Gaussian profile had a depth of 200 nm, similar to the crater depths observed in experiment and the rounded crater a radius of 500 nm. A flat reference was also modelled to approximate the effect prevailing at the 20 μm crater bottom. A layer with a changed refractive index ($\pm\Delta n$) (4.11c) was added on the glass surface to simulate the modified region. For the layer stack glass/texture/ $(\pm\Delta n)$ /AZO/i-aSi:H, the thickness of the modified layer ($\pm\Delta n$) was varied between 50-1000 nm, thicknesses reported in literature

[115, 116]. Both positive and negative refractive index variations were investigated for the range 0.005-0.5, similar to experimentally observed and reported variations in literature [56, 118, 129–131].

4.2.2 Optical generation rate profile

Figure 4.12 shows the optical generation rate (G_{opt}) profiles at a 700 nm wavelength in the differently textured substrates. The results are shown for representative parameters summarizing the most important observations in the variations carried out. The wavelength of 700 nm was chosen because light in-coupling is relevant here due to its high penetration depth in the aSi:H layer ($4.8 \mu\text{m}$). The refractive index at this wavelength was 1.47 and the results are shown for $\Delta n = -0.005$ and thickness 200 nm of the modified glass region.

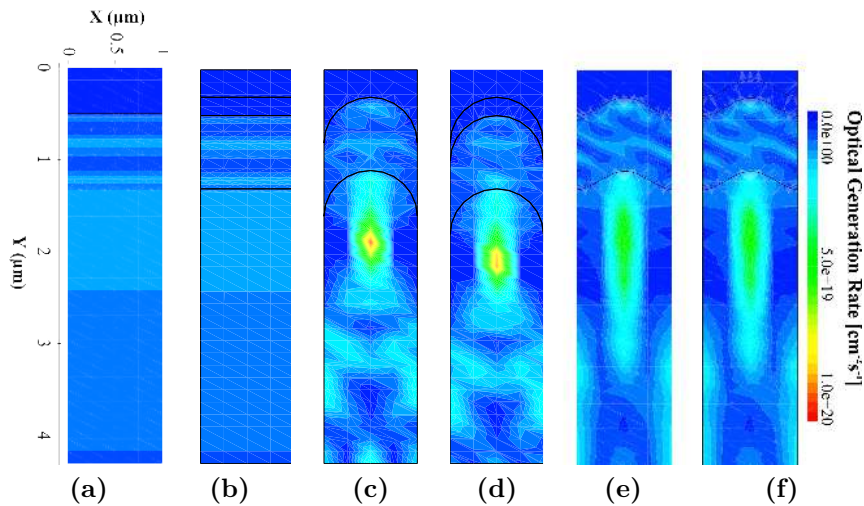


Abbildung 4.12: Optical generation (G_{opt}) rate profiles at 700 nm wavelength of the solar cell layer stack glass/texture/ $(\pm\Delta n)$ /AZO/i-aSi:H on (4.12a) flat reference (4.12b) with $\Delta n = -0.005$ modified region, (4.12c) rounded crater texture, (4.12d) with $\Delta n = -0.005$ modified region and (4.12e) Gaussian crater texture (4.12f) with $\Delta n = -0.005$ modified region. Maximum intensity of the colour bar of the optical generation rate was set to $1 \times 10^{20} \text{cm}^{-2} \text{s}^{-1}$.

The flat reference (4.12a) showed a stationary wave in the AZO layer, which indicated the light was strongly reflected on the AZO/aSi:H interface without any scattering. The low refractive index change (4.12) on the glass surface did not affect the G_{opt} profile. Rounded crater texture on the glass surface (4.12c) changed G_{opt} to a focused profile. The distance of the focal point was about 800 nm from the AZO/aSi:H interface.

Decreasing the radius reduces the focal length according to geometric optics [128]. Similarly, increasing the radius increases the focal length beyond the simulation domain dimensions, as expected for the experimentally obtained $20 \mu\text{m}$ crater. The behaviour observed in the flat reference was approximated for the crater bottom while the low refractive index change (4.12d) $\Delta\pm 0.005$ on the glass surface had no influence on G_{opt} .

G_{opt} focusing behaviour was also observed for the Gaussian profile (4.12e). The focal length was around 750 nm away from the AZO/aSi:H interface. Focusing was not as confined as for the rounded crater and extended further into the bulk material. Low refractive index change (4.12f) on the glass surface did not change G_{opt} . Altering the thickness of the refractive index modified region ($\Delta\pm 0.005$) on the glass substrate surface had no effect on G_{opt} for all the textures either (4.12a-4.12f).

4.2.3 Simulated reflection

The simulated reflections of the layer stacks glass/texture/ $(\pm\Delta n)$ /AZO/i-aSi:H are shown in figure 4.13. A comparison between the flat reference and textured substrates (4.13a) showed that implementing a periodic texture reduced the reflection. Also, slight refractive index modification whether positive or negative (4.13b) did not influence the optical behaviour in all the investigated geometries. Furthermore, an increased thickness of the modified region ($\Delta n\pm 0.005$), had no effect on the reflection either. Change in the reflection was observed for higher refractive index variation.

Figure 4.13c shows the reflection of the layer stack with rounded crater texture and 200 nm modified region with decreasing refractive index. Decreasing Δn increased the reflection. While a moderate change ($\approx 2\%$) was observed for $\Delta n = -0.05$, more intense ($>10\%$) deviation was observed for $\Delta n = -0.5$. Increased Δn (4.13d) also enhanced the reflection, but the extent of the change was not as high as for the reduced refractive index. Increased thickness of the modified region for higher Δn increased the reflection intensity and interference profile (not shown).

It should be noted that in the simulations, the modified region was assumed to be an isolated layer with a constant Δn and defined thickness. Furthermore, the investigated modified film thicknesses were in the range of the wavelengths (≤ 1000 nm). Thus, optical effects such as quarter-wavelength anti-reflection (effective medium) might be modelled, which do not necessarily apply to the experiment. Studies show that the evolution of the refractive index change [56] and molten region [115] around the crater is graded. The simulation results and trends observed in the reflection following refractive index change were nevertheless valid. Calculations and experiment of the reflection for the layer stack glass/AZO confirmed the simulated trend.

Figure 4.14a shows the reflection $R = (n_{glass} - n_{AZO})^2 / (n_{glass} + n_{AZO})^2$ calculated with the refractive index values used in the simulation. The reflection at the interface was increased with the decreasing refractive index of the glass substrate. In contrast, increasing the refractive index reduced the reflection, because the difference between the glass and AZO refractive indices was minimized. A similar reflection behaviour was experimentally measured for AZO coated textured Type II glass substrates (4.14b).

The glass substrates were laser textured with $\nu_{max} = 2000$ mm/s and 1000 mm/s. A negative refractive index change of $\Delta n_{typeii} = -0.02$ was measured for the periodically tex-

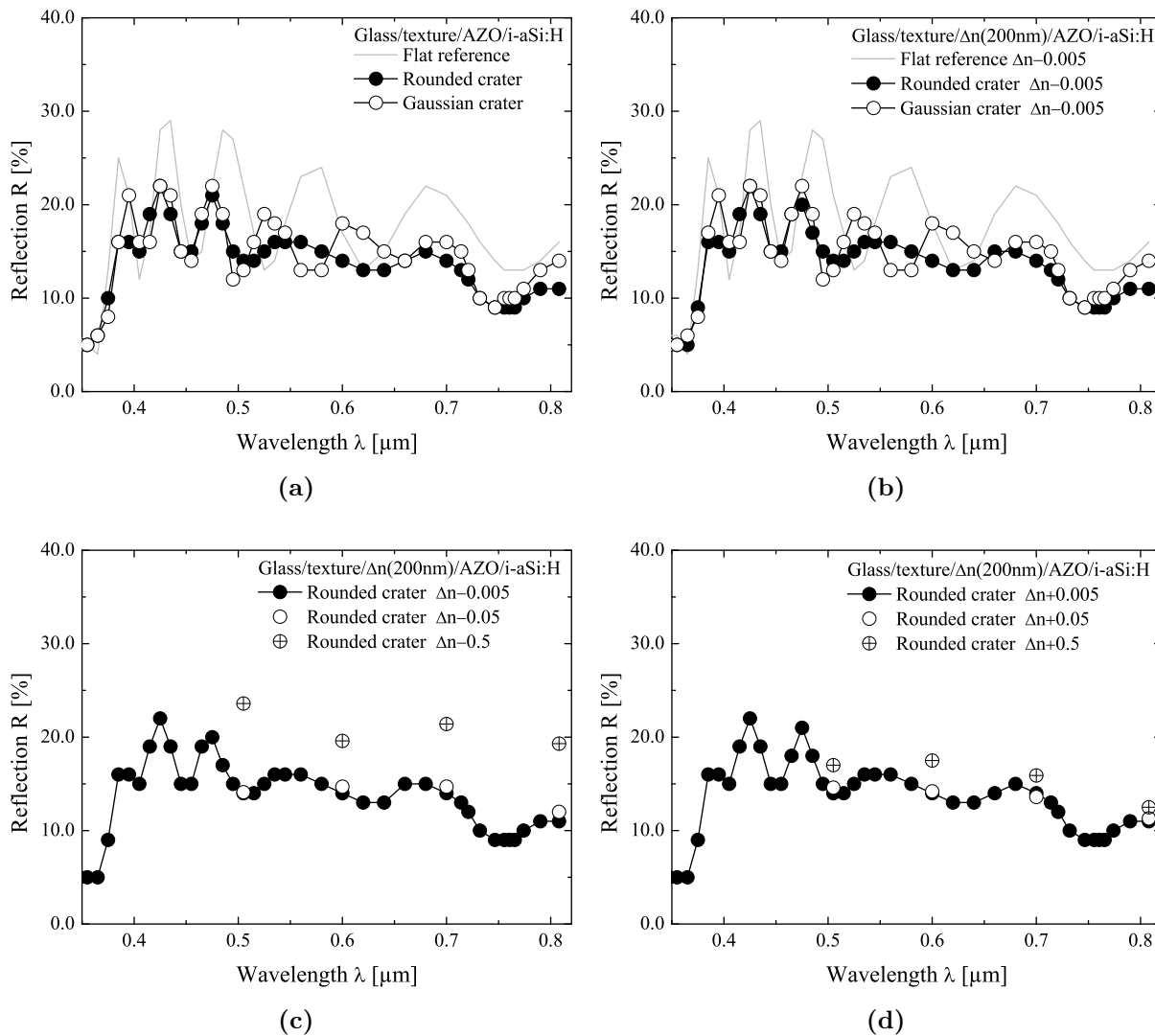


Figure 4.13: Simulated reflection of the solar cell layer stack glass/texture/ $(\pm\Delta n)$ /AZO/i-aSi:H on (4.13a) a flat reference, rounded and Gaussian crater texture (4.13b) with reduced refractive index $\Delta n = -0.005$ region of 200 nm on the glass surface. Rounded crater texture with (4.13c) decreasing and (4.13d) increasing refractive index of the 200 nm modified region on the glass surface.

tured 2000 mm/s glass substrates. These experiment results showed how the laser induced morphological changes influenced the reflection. Reflection was first slightly reduced at a low spot overlap (2000 mm/s) and gradually increased with increasing texture (1000 mm/s). A comparison to simulations and calculation suggests that a decreased refractive index change of the glass surface is responsible for the observed increased reflection. These results further indicate that the refractive index on highly textured substrates is much higher than $\Delta n_{\text{typeii}} = -0.02$ of the periodically textured substrate.

For the application in the superstrate configuration, means of mitigating the reflection losses must therefore be investigated. Molecular vibrational modes of differently textured glass substrates were therefore investigated from Raman measurements and are discussed in the following Section (4.3). Furthermore, a better understanding of bulk material gives

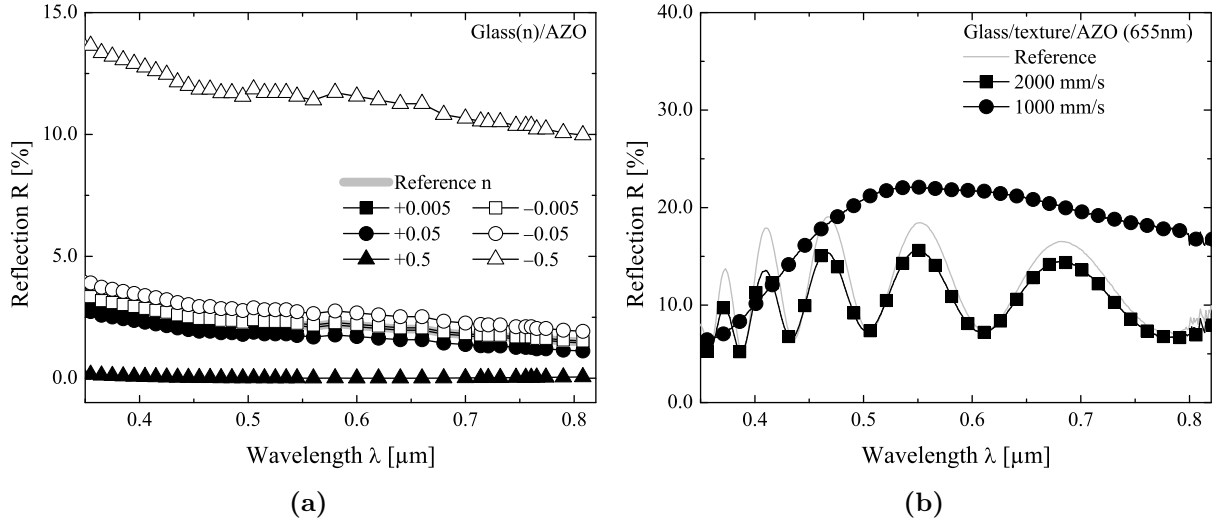


Figure 4.14: Reflection (4.14a) calculated by $R = (n_{glass} - n_{AZO})^2 / (n_{glass} + n_{AZO})^2$ for normal incidence at the glass/AZO interface for varying refractive index of the glass surface and (4.14b) measured on AZO coated textured Type II glass substrates

indication of the surface morphology. This is an important aspect for AZO deposition. Optoelectronic properties of AZO were assumed to be constant for flat reference as well as textured substrates in the simulations. However, glass morphology influences AZO growth and thus optoelectronic properties of the AZO. Influence of the glass surface morphology on the AZO properties were investigated experimentally and discussed in Chapter (5).

4.3 Raman optical properties

Simulation results showed that the reduced refractive index change following laser ablation in Type II glass substrates had a severe impact on the reflection of the substrates. Raman scattering of Type II glass substrates were therefore investigated to determine the mechanisms responsible for the reduced refractive index change. The section is organised as follows: first the commonly found band interpretations in literature for the reference substrates are discussed (subsection 4.3.1), then the observed variations in the bands following laser texturing at varying pulse energy (subsection 4.3.2) and scribing speed (subsection 4.3.3) are detailed. Post-ablation annealing of the substrates was investigated to analyse the reversibility of the molecular rearrangement and is detailed in subsection 4.3.4.

4.3.1 Band interpretation

Low-frequency region I Figure 4.15 shows the reduced Raman intensity (I_{red}) of a reference Type II substrate, normalized to the highest peak intensity. The characteristic peak shape, observed to be universal for the amorphous state [76, 80, 98, 100, 135–139], was observed with the maximum intensity around 120 cm^{-1} . The low-frequency broad

band ($\bar{\nu} < 300 \text{ cm}^{-1}$) is observed in disordered vitreous materials and commonly accepted to arise from excess vibrational density of states (VDOS) [76, 80, 98, 100, 137, 139]. The population density of thermally excited phonon at room temperature is high and observed in low-frequency Raman spectra [140].

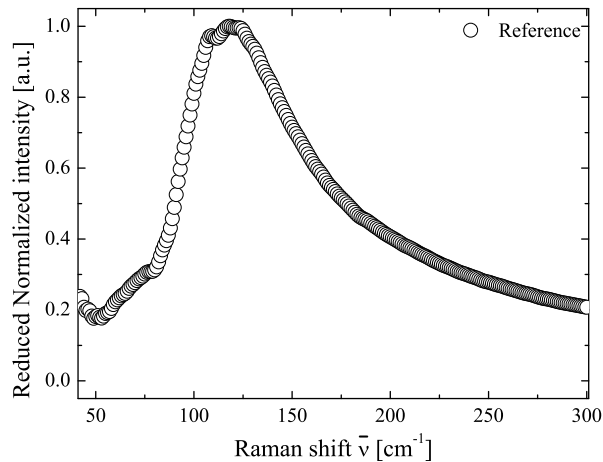


Figure 4.15: Reduced and normalized Raman intensity (I_{red}) of a Type II reference glass substrate

The enhancement is observed in the low-frequency region and is therefore frequency- and temperature-dependent [80]. The origins are controversially debated with contradicting theories in condensed matter physics research [76, 80, 98, 100, 136–141]. One assumption is the bond-bending modes of interconnected chains which are susceptible to the longer-range structural (dis)order [140]. In lithium and caesium containing borate glass, the origin is coupled with vibrations of boroxol rings and rattling-like vibrations of alkaline ions [100]. Similarly, Gamut et al. assign the band to metal cations such as Ba^{2+} , Sr^{2+} bond vibrations in borosilicate glasses containing La_2O_3 and $(\text{Ba}, \text{Sr})\text{Ti}_3$ [142]. Alkali ions are suggested to influence the peak because they constrain the transverse displacement of the low atomic density structural units surrounding them [76].

The region furthermore becomes cumbersome to interpret, as acoustic modes are assumed to manifest in this band [76, 98, 135, 136, 138–140, 143]. In particular, a linear correlation between the band frequency and the transverse sound velocity has been identified [76, 136, 139]. An elevation in the low-frequency region ($< 55 \text{ cm}^{-1}$) is assumed to arise from anharmonic (relaxational) motions responsible for the quasi-elastic scattering [144]. The presence of these modes would indicate a disordered structure. Harmonic (or vibrational) motions which account for an inelastic broad band are assumed to be responsible for the higher frequency region ($> 55 \text{ cm}^{-1}$) where the boson peak (BP) is observed [144].

Several physical and structural properties of the glass substrates are assumed to contribute to this peak and thus manifest in this region. The frequency and intensity of the peak are strongly influenced by the nature of the matrix [76, 80]. The peak is also assumed to be related to other properties such as thermal-conductivity [76]. With respect

to the demonstrated glass properties in table 4.1, C_P is similar for all the glass types, which might explain the observed similar peak position (not shown).

Other studies have demonstrated that the peak correlates with the shear modulus, which relates the stress with the strain (shear modulus=shear stress/shear strain) [145]. Strong glasses are interpreted to show an intense peak while weak glasses demonstrate a weak peak [76, 100]. Structural disorder in the glass matrix is also reflected in the region and an enhancement in this region would indicate an improved matrix structure. Variation in the physical and structural properties following texturing and annealing is thus expected to be reflected in this region. BP dependency on the texturing and annealing properties was therefore investigated to deduce the modification in glass properties.

High-frequency region Figure 4.16 shows a baseline corrected and deconvoluted spectrum of a reference Type II substrate. The baseline corrected spectra were fitted with an increasing number of Gaussian peaks, until no further changes in the residual occurred with further added Gaussian peaks [146, 147]. Gaussian peaks were fitted without any restrictions on the position, width, height and positions.

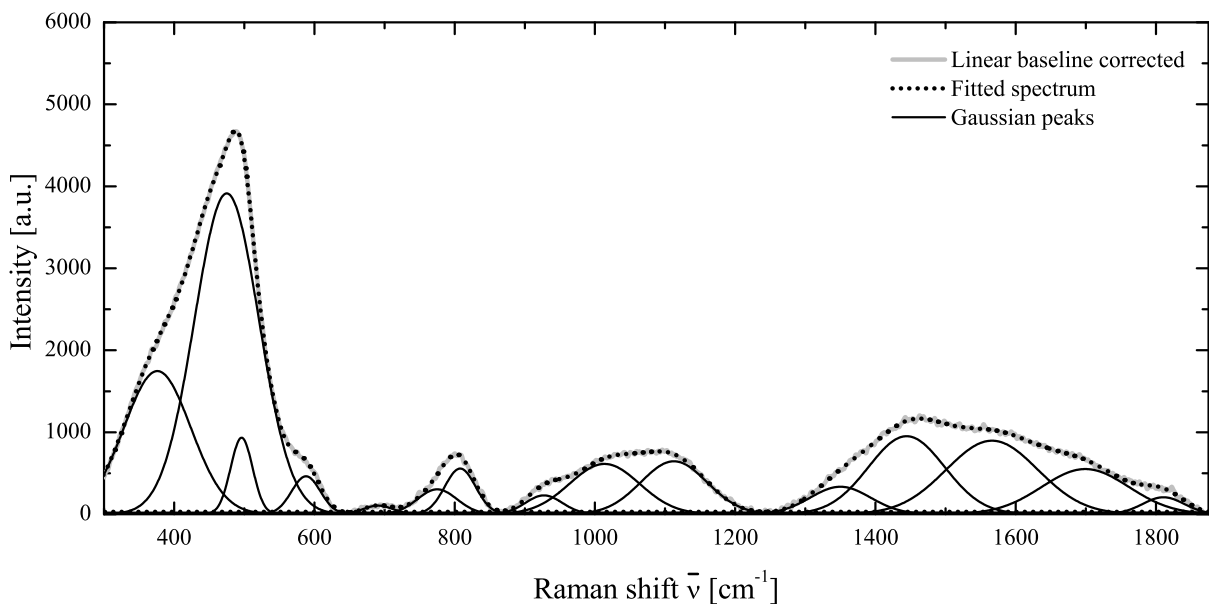


Figure 4.16: Raman shift $\bar{\nu}$ of baseline corrected spectra and deconvoluted peaks in Type II reference glass substrates

For the analysis and interpretation, the spectra were distinguished into the regions *low-frequency II* 200-650 cm^{-1} , *mid-frequency* 650-850 cm^{-1} , *high-frequency I* and 850-1250 cm^{-1} and *high-frequency II* 1250-1875 cm^{-1} . The assignment of deconvoluted peaks found in literature is summarized in table 4.3. For all subsequent discussions, detailed frequencies should be understood as approximate values of the Raman shift ($\bar{\nu}$). The assignment and interpretation in table 4.3 is reviewed for silicate, borate and borosilicate glass substrates containing aluminium, earth and alkaline metals.

	Position [cm^{-1}]	Peak assignment	
Low-frequency II	200 – 500	Si-O and B-O network bending	[148–151]
	495	Q ⁴ SiO ₄ /breathing of three-membered rings	[75, 152]
	590	Q ² SiO ₄ /B-O-Si bending	[141, 152]
	600	metaborate / breathing of four-membered rings	[75, 153]
Mid-frequency	650 – 870	stretching of borate rings	[154]
	700 – 850	rocking of Si-O-Si bridges	[150]
	750	six-membered ring with one BO ₄ units	[75, 152, 153]
	770	six-membered ring with two BO ₄ units	[75, 101, 104, 152, 153, 155]
	806	boroxol rings breathing	[79, 143, 149, 152]
High-frequency	800	Q ⁰ orthosilicate stretching	[156]
	920	Q ¹ pyrosilicate stretching	[141, 148, 149]
	950 – 1000	Q ² metasilicate stretching	[75, 151]
	1050 – 1100	Q ³ disilicate stretching	[75, 129, 150–152, 156]
	1150–1200	Q ⁴ stretching	[75, 149–153]
High-frequency II	1250–1380	free BO ₃ units	[149, 157, 158]
	1410 – 1430	BO ₃ units bonding BO ₄ in chain	[149, 155, 159]
	1450–1600	BO ₃ units bonding BO ₃ in chain	[149, 155, 160–162]
	1550	molecular oxygen dissolved in matrix	[150]
	1670	metal ion transitioned to higher state	[163, 164]
	1615 – 1870	hydroxyl-related and combined modes or overtones	[165, 166]

Tabelle 4.3: Literature review of deconvoluted peak assignment in silicate based glass

The peak assignment is commonly achieved by systematically changing the glass composition and observing the changes in the bands in comparison to the corresponding crystal [149, 156]. This procedure and several others used to assign the bands only give assumptions [156], which results in the deconvoluted peaks being assigned to several different structural units in different glass compositions [146, 147, 149, 153, 156, 167, 168]. The properties of the convoluted bands (spectral regions) nevertheless indicate the quality of the glass matrix such as the degree of polymerisation [156].

The structural re-arrangement was thus analysed by comparing the sum of the area under the peaks at a defined frequency ($A_{\bar{\nu}}$) of a band with the total area (sum of all peaks) of the spectrum (A_{total}). The area fractions were defined as follows:

$$A = \frac{(A_{375} + A_{475} + A_{495} + A_{590})}{A_{total}}$$

$$B = \frac{(A_{690} + A_{775} + A_{806})}{A_{total}}$$

$$C = \frac{(A_{920} + A_{1012} + A_{1114})}{A_{total}}$$

$$D = \frac{(A_{1350})}{(A_{1350} + A_{1450} + A_{1560})}$$

A and C are associated with network polymerization [149, 156] and assumed to indicate Si-O-Si linkages within the glass matrix [153, 156]. B is assumed to indicate “disorder” of the matrix and D the variation in the metaborate groups [149, 160, 162].

The *high-frequency II* $\bar{\nu} > 1600\text{cm}^{-1}$ region contains bands, which are not often reported in literature. Hydrous (1630 cm^{-1}) [165] and organic (1810 cm^{-1}) [169] species have been reported to manifest in this region. Changing atmosphere in the laboratory and thus different quantity and quality of species inserted into the matrix during texturing might influence these bands. Furthermore, the bands around 1810 cm^{-1} might be greatly susceptible to the linear baseline correction. Thus, only the bands associated with stretching of the B-O bonds of the borate network [155] in the region $\bar{\nu} < 1600\text{cm}^{-1}$ were taken into consideration.

In the following sections, variation in normalized I_{red} , A, B, C and D of reference and laser-textured substrates are compared. The results are discussed for laser texturing at varying pulse energy E_p (subsection 4.3.2), scribing speed ν_{max} (subsection 4.3.3) and post-ablation annealing at different temperatures (subsection 4.3.4).

4.3.2 Pulse energy variation

The pulse energy variation was carried out to determine the laser spot diameter as detailed in section 4.1.3 at a constant $\nu_{max}=3000\text{ mm/s}$. The surface texturing with varying ν_{max} was then performed at a constant pulse energy $115\text{ }\mu\text{J}$ to ensure a homogeneous texturing (Section 4.1.3). The structural modifications in textured substrates were therefore assumed to result from the superposition (I) of the single and (II) overlapped pulse energy. The influence of the single (I) pulse energy on the Raman scattering of Type II substrates is illustrated in figure 4.17. The reduced Raman intensity I_{red} (4.17a) did not show any dependency on the texturing energy. The band shape and intensity remained similar and suggested that the physical and structural properties were minimally influenced at these ablation parameters.

The corresponding area fractions A, B, C and D are shown in figure 4.17b. Slight variations ($<3\%$) were observed in the area fractions of laser-textured substrates in comparison to the reference (dashed horizontal line). The extent of the changes was comparable to values for glass composition analysis [149] reported in literature. An increase by $\approx 3\%$ at $79.28\text{ }\mu\text{J}$ pulse energy was observed in comparison to the reference. D reduced by 3.8% and increased by 9.7% at the pulse energy $79.28\text{ }\mu\text{J}$ and $117.5\text{ }\mu\text{J}$, respectively.

The changes in A and D might indicate increased Si-O-Si linkages and reduced “loose” BO_3 units following texturing with pulse energy $<79.28\text{ }\mu\text{J}$. Bhardwaj et al. suggest that the structural modification observed in the glass substrates result from restructuring of strained bond and molecular rearrangements [56]. Densification of fused silica ablated

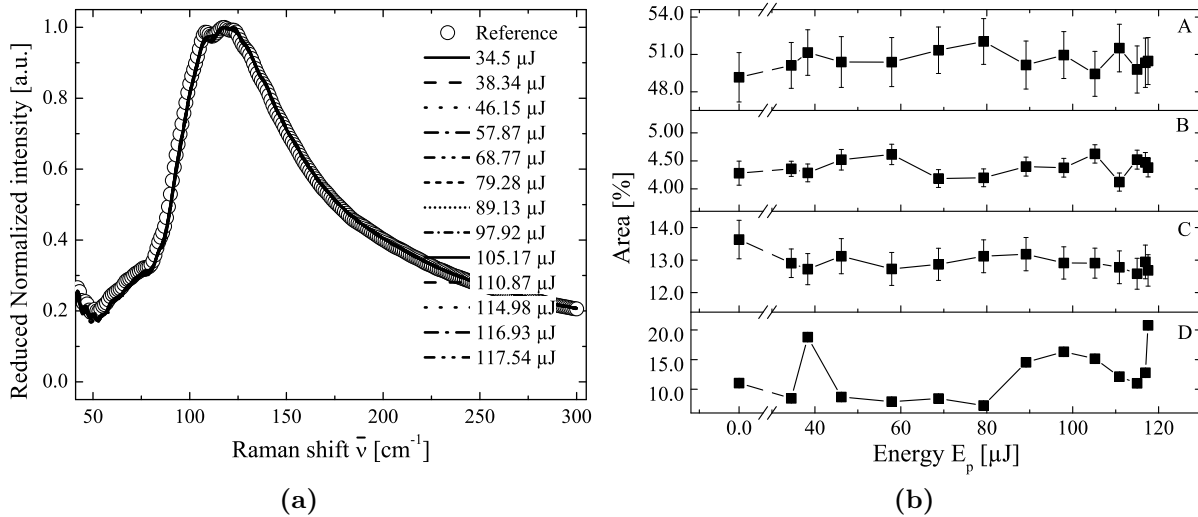


Figure 4.17: Type II glass substrates (4.17a) reduced and normalized Raman intensity and (4.17b) area fractions A, B, C, D as a function of the pulse energy E_p at a constant scribing speed $\nu_{max}=3000$ mm/s.

with low-energy pulse is reported to result from the rearrangement of broken five- and six-fold rings to smaller three- and four-fold rings [118] and decreased Si–O–Si bond angle [56]. Chan et. al. demonstrate that there is a correlation between the increased density, increased refractive index and 490 and 605 cm^{-1} peaks of the glass. This might explain the observed trend in A and D and the increased refractive index.

4.3.3 Scribing speed variation

The scribing was carried out at a constant pulse energy 115 μJ and the scribing speed ν_{max} varied between 6000-200 mm/s. The influence of the (II) overlapped pulse energy is shown in figure 4.18. The observed variation in the Raman spectra following scribing at lower speeds was more profound in comparison to the pulse energy variation. The results suggest that the maximum peak position of I_{red} (4.18) shifts to lower wavenumbers. This might be a consequence of a changed refractive index.

Another explanation found in literature for refractive index change includes the migration of (earth) alkaline metals away from the heat-affected zone, which reduces the density and refractive index of the region [56]. It is also possible that the investigated glass had less dense material surrounded by densified regions as a result of stress [56]. Transverse displacement of the structural units around the alkali is believed to be limited and therefore influences the boson peak position [76]. Constraints from the migrated alkali in highly textured substrates might be eliminated. It is also possible that low atomic density regions hosting the alkali are increased in cross section, thereby reducing the density [76].

A further hypothesis for the refractive index change includes defects resulting from the

formation of mobile charge carriers following texturing [127]. Defect formation is greater for alkali with increasing diameter [130], which might further explain the suggested high refractive index change in Type II. Highly absorbing trapped hole centres at the site of non-bridging oxygen \emptyset near an alkali, are produced from the interaction of the charge carriers [127]. For multi-component glass, loss in transmission near the ultra violet region is attributed to trapped electrons induced by fs laser [127]. This might further explain the observed reduced absorption and transmission in the investigated highly textured substrates.

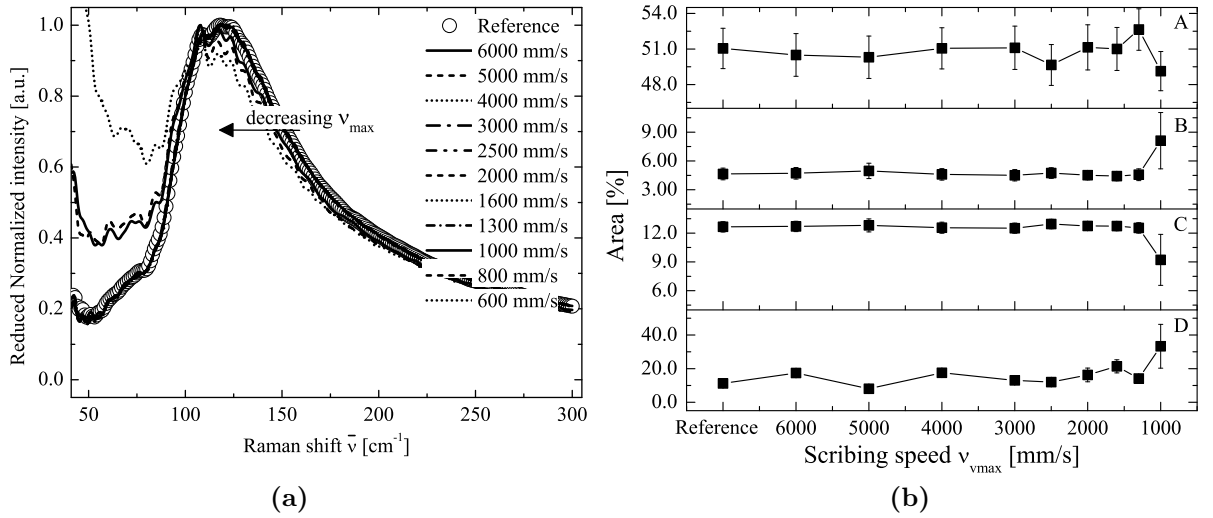


Figure 4.18: Type II glass substrates (4.18a) reduced and normalized Raman intensity I_{red} and (4.18b) area fractions of A, B, C and D as a function of scribing speed ν_{max} at constant pulse energy $E_p=115\mu\text{J}$

Elevation in the low-frequency region ($<100\text{ cm}^{-1}$) was observed for substrates textured with $\nu_{max} \leq 1000\text{ mm/s}$. Decreased intensity in this region is furthermore an indication of compromised glass mechanical strength [76, 100], which is a major drawback. The elevations might be an indication for increasingly disordered glass matrix with decreasing scribing speed [144].

This assumption would correlate with the changes observed in the area fraction. A and C decreased by 1.9% and 3.4%, respectively. D reduced by 3% and increased by 22% at 5000 mm/s and 1000 mm/s in comparison to the reference, respectively. Increased D suggests the structural disorder results from an increased number of “loose” BO_3 units. Increased B (3.5%) at 1000 mm/s might further indicate the variation in the silicate matrix structural units.

McMillan et al. [156] associate the bands near 800 cm^{-1} with silicon vibrations in Q^0 orthosilicate (SiO_4) with four non-bridging oxygen (NBO) [156]. They observe that the band shifts to lower frequencies to near 770 cm^{-1} and the intensity decreases with reducing silica content [156]. They further suggest that the vibrations might be due to

highly polymerized and semi-rigid networks [156].

This assumption contradicts the assignment of the region to the disorder of the matrix. It might however explain the additional sharp peaks observed throughout the spectra of highly textured substrates. To recall, a white high reflecting powder was observed for very low scribing speeds ($\nu_{max} \leq 1000$ mm/s), which is reported to result in the resolidification of plasma plume [112, 123, 124].

The raw Raman intensities of these substrates were lower and characterised with additional sharp peaks in comparison to periodically textured substrates. It should also be noted that the error in the fitted data and calculated area fractions increased with decreasing speed, particularly for $\nu_{max} \leq 1000$ mm/s. This might be due to the highly diffuse scattering surfaces. While the substrates show desired light scattering properties, the texturing degree was at the cost of material stability. These substrates ($\nu_{max} \leq 1000$ mm/s) were excluded from further analysis as the cracks were expected to be detrimental for solar cell stability. For substrates textured at $\nu_{max} \gtrsim 1000$ mm/s few cracks were also observed. Wortmann et al. report that thermally induced stress resulting from ablation at high E_p with a high volume of melted and resolidified material is permanent [130]. Cracks, stress and defects in the glass would of course be a trade-off between stability and performance of the solar cells. Annealing at temperatures commonly used to deposit AZO was thus investigated as a possible means of reducing observed material deterioration.

4.3.4 Annealing effect

Thin-film solar cells are commonly deposited on glass substrates coated with AZO, which is deposited at various temperatures ranging between 150-450°C [170]. Before deposition, the substrates are heated for a considerable amount of time to reach a steady temperature. Studies demonstrate that laser induced structural modifications are reversible by post-annealing to a certain extent [56, 80, 131, 137]. It would be an added advantage, if the induced annealing effect at temperatures used for AZO sputtering were permanent and also applicable to laser induced stress. For this investigation Type II substrates were heated for one hour at temperatures between 150-450°C. Annealing was carried out for substrates scribed at a constant pulse energy $E_p=115\mu\text{J}$ and varying scribing speed ν_{max} 6000-1000 mm/s.

Figure 4.19 shows the normalized reduced intensities of annealed substrates. For a better overview only the reference figure 4.19a and substrates textured at 1000 mm/s figure 4.19b are shown. The results suggest that I_{red} of the reference substrates does not change following annealing at 150-450°C. A similar behaviour was observed in periodically textured substrates. The intensity of the reduced Raman reduced ($\bar{\nu} > 100$ cm⁻¹) and widened ($\bar{\nu} > 100$ cm⁻¹) with increasing temperatures for highly textured substrates in comparison to the reference. Similar observations are made by Yannopoulos et al. who summarise that annealing induced changes in low energy region of the Boson peak, induced

a blue-shift of the maximum peak frequency and decreased the intensity [80].

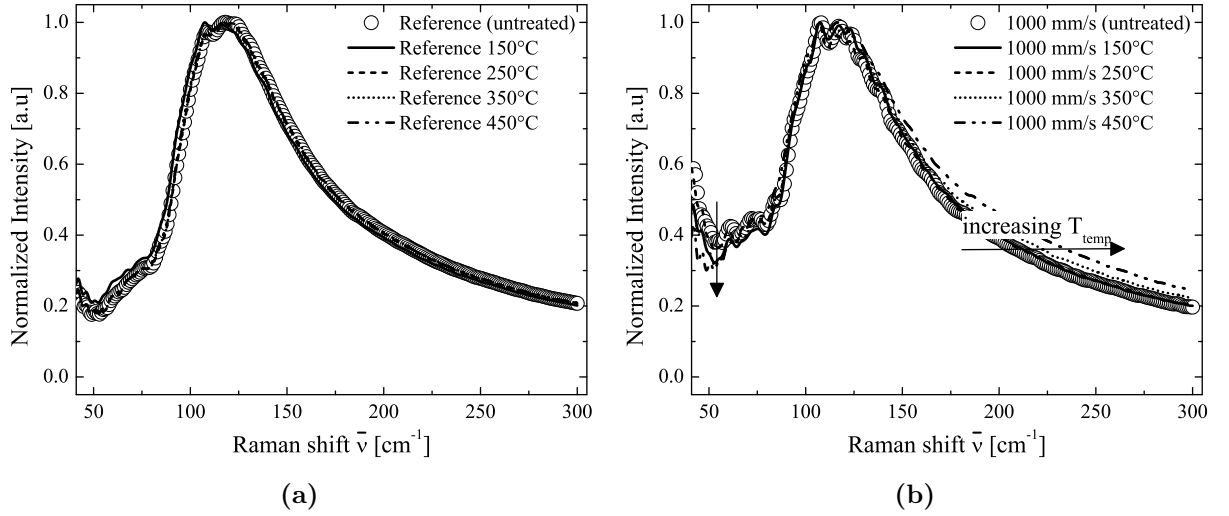


Figure 4.19: Type II glass substrates reduced and normalized Raman intensity I_{red} of (4.19a) reference and (4.19b) textured glass substrates at 1000 mm/s as a function of annealing temperatures

Figure 4.20 shows the area fraction of A (4.20a), B (4.20b), C (4.20c) and D (4.20d) for $\nu_{max} < 3000$ mm/s. Higher scribing speeds are not shown because the area fractions of periodically textured and post-annealed substrates did not show any variation. The results suggested that molecular vibrations in highly textured substrates such as $\nu_{max} = 1000$ mm/s changed post-annealing. For example, A and B decreased by 22% and >2% following annealing at 450°C in comparison to the textured (1000 mm/s) reference, respectively.

Chan et. al. show that the refractive index increases with increasing 490 and 605 cm^{-1} peak intensities. The reduced A and B might be an indication of the reversed effect. The results did not show a clear dependency between annealing and mid-frequency vibrations resulting from Si-O-Si linkages. The intensity of B-O vibrations in the high frequency II assigned to “loose” BO_3 units was slightly lower (with the exception of 1000 mm/s at 450°C) following annealing in comparison to the reference. Samples were measured several weeks after annealing and the reversed effect was still observed. The results suggested that annealing with increasing temperatures improved material properties, particularly in randomly textured substrates.

In summary, laser texturing glass substrates with decreasing scribing speed changed the obtained surface texture from periodic to random. Light scattering properties of substrates increased with increasing texture. The results demonstrated that laser texturing also induced atomic-scale structural re-arrangements comparable to literature [56, 118, 129] in Type II glass substrates. Numerical modelling and calculations suggested that the refractive index change was much higher in highly textured substrates than in periodically textured substrates. The reduced refractive index was detrimental for light in-coupling in

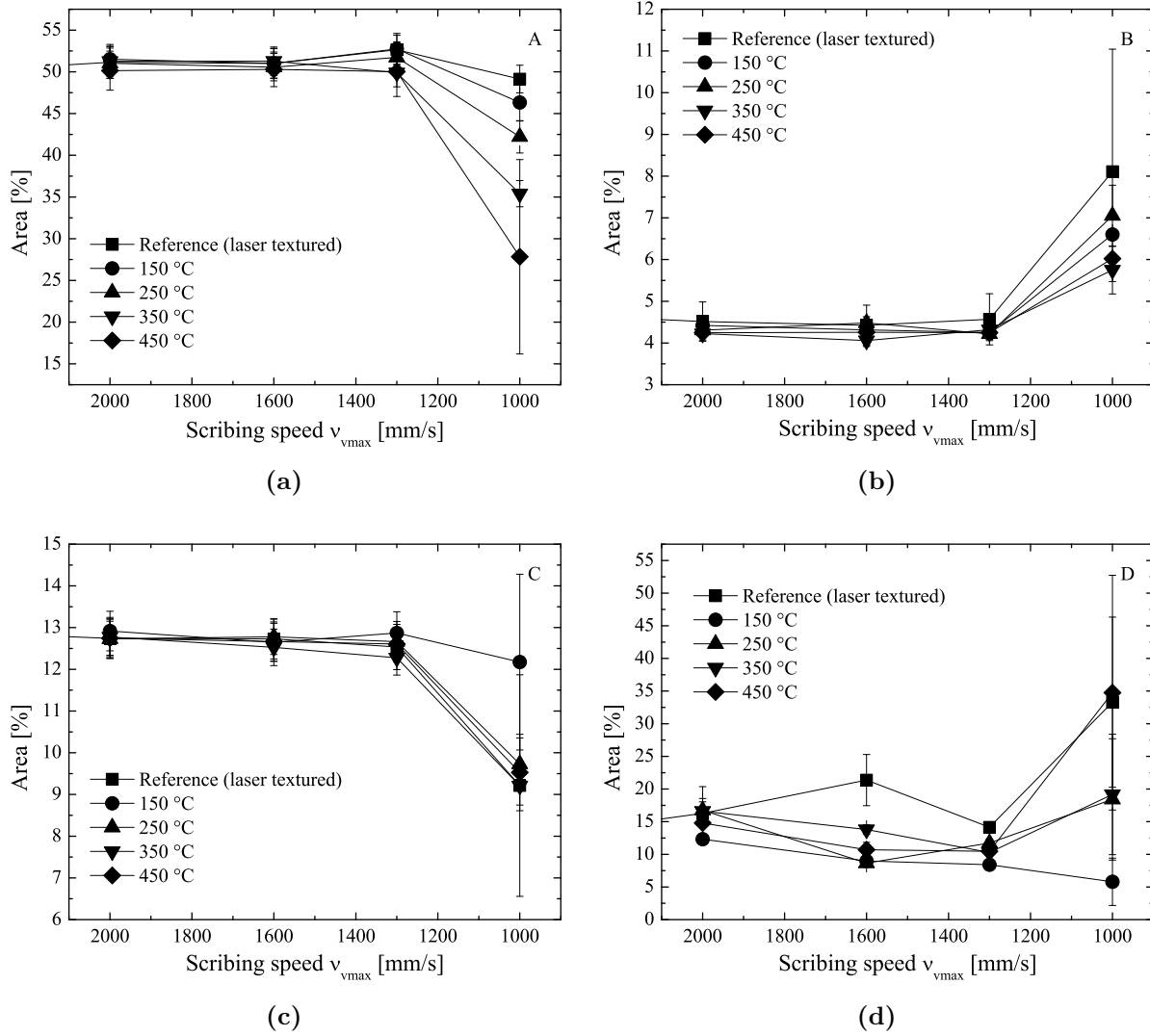


Figure 4.20: Area fractions A (4.20a), B (4.20b), C (4.20c) and D (4.20d) for substrates textured at $v_{max} < 3000$ mm/s as a function of annealing temperature

silicon thin-film solar cells stacks. The Raman spectra suggested that increased three- and four-fold rings or alternatively Si-O-Si linkages were responsible for the increased refractive index. The results suggest that annealing between 150-450 °C reduces the structural modification.

Both the topological and chemical changes on surface are crucial aspects for deposition and growth of AZO front electrodes. Mobile metals and charge carriers present near the surface resulting from the migration might diffuse into the AZO films during deposition. Depending on the nature of the ions, this might be detrimental if they act as contaminants [96]. Similarly, the topology as well as the densified and decompressed borosilicate network in the heat-affected zone, which is also assumed to prevail on the surface might promote or impend AZO nucleation. This would then influence the growth mechanisms and further affect AZO structure-dependent properties and subsequently the solar cell performance. These aspects are investigated in the following Chapter 5 where the quality of AZO

films deposited on differently textured substrates at different temperatures are analysed. Drawbacks of using textured carrier substrates addressed in literature such as deteriorated AZO properties are addressed. Consequently, silicon thin-film based solar cells in the substrates and superstrate configuration are investigated along with micromorph tandem solar cells in Chapter 7. Potential of highly textured glass with low transmission for bifacial application in nip solar cells is assessed.

5 Aluminium doped zinc oxide

The topology of picosecond laser-textured glass substrates was changed from periodic to random with decreasing scribing speed. Phase contrast images and molecular vibration modes showed structural modifications in textured substrates compared to reference substrates. The morphology of the glass substrate influences AZO growth and the quality of the final polycrystalline films. The optoelectronic properties of AZO depend on its microstructure and are relevant for the performance of solar cells. This summarises the results of DC magnetron sputtered AZO on the differently laser-textured glass substrates.

5.1 Thin-film growth

Aluminium doped zinc oxide (AZO) is an attractive transparent conductive oxide (TCO) due to its wide band gap E_g (≈ 3.4 eV) [96] and large exciton binding energy (60 meV) [90]. It is abundant, non-toxic and stable in hydrogen-rich ambient and therefore a suitable front electrode in thin-film solar cells. Thin and highly conducting AZO films are desired for this application to reduce parasitic absorption. One main challenge is the trade-off between the optical and electrical properties.

The electrical properties can be improved by increasing the charge carrier concentration and mobility by reducing the scattering centres [171]. Optoelectronic properties can be adjusted by deposition conditions such as temperature and pressure, depending on the deposition technique. Methods of depositing AZO include pulsed laser deposition (PLD), chemical vapour deposition (CVD) and physical vapour deposition (PVD) [172]. Sputtering is a PVD technique readily used and its advantages include the use of relatively low substrate temperatures, flexible deposition parameters and rapid large area coverage [90, 96, 172].

In this study, AZO films were deposited on differently textured Type II glass substrates by DC magnetron sputtering. (A detailed analysis of the glass substrates and ablation parameters is given in Chapter 4, Section 4.1.3). The investigated AZO film thicknesses were 75, 552, 650, 869, 1340 and 1963 nm. The thickness measurements were carried out on flat references and assumed to apply for textured substrates in co-deposition.

It should also be noted that the deposition conditions were not optimized for the textured substrates. Rather, deposition parameters (Chapter 3) were kept constant and the substrate surface texture was the only variable in the sputtering process. The aim was a better comparison between AZO deposited on flat reference and textured substrates. Growth mechanisms and parameters influencing the evolution must be understood to compare the substrates. The fundamental stages of thin-film growth are therefore summarized

in the following section.

Fundamental growth stages Thin-film growth is distinguished into two phases (I) initial growth and (II) actual growth [173]. Initial growth (I) starts with the sputtered high energetic adatoms impinging on the glass substrate surface from various directions [174]. Successful adsorption of adatoms is dependent on several parameters including their trapping probability and sticking coefficient or probability to remain adsorbed [175]. The substrate molecules interact with the condensed adatoms by van-der-Waals forces or chemical bonds [175] depending on their nature. The former results in physisorption and is observed for non-polar molecules while the latter in chemisorption by polar molecules [175].

Chemisorption leads to stretching of bonds on the substrate, which creates surface tension γ_s [175, 176]. The surface tension also depends on the energy of broken bonds of atoms exposed on the surface, which in turn is determined by the crystallographic orientation $\gamma(hkl)$ of the substrate [176]. The tension can be reduced if the adatoms have sufficient energy and time to diffuse to lower energetic sites. Moreover, the diffusion rate increases with rising substrate temperatures.

For thin-film growth to occur, the surface energy barrier must be overcome by adatoms arriving on the surface. In the PVD process, this is possible because the vapour adatoms have a higher chemical potential than the condensate on the substrate surface. Condensates eventually form nuclei, the building blocks of the film growing in the actual growth (II) phase [173]. Growth forms are distinguished into three conditions as shown in figure 5.1.

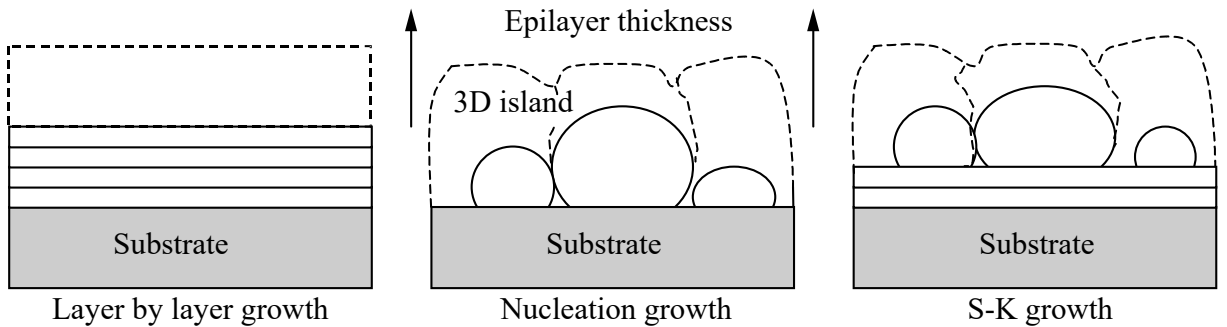


Figure 5.1: Schematic of growth models resulting from substrate and film mismatch [174]

The growth model depends on the relationship between the surface energies of the substrate γ_s , film γ_f and substrate-film interface γ_i which are distinguished into

- $\gamma_i + \gamma_f \leq \gamma_s$ layer-by-layer growth, also termed wetting and commonly known as the Frank-van der Merwe model (FW) [174]. The adatoms are attracted more to the substrate than to each other [176]. As a consequence, monolayer island aggregates first grow and then coalesce to form a monolayer [177]. This growth

mechanism is considered to be thermodynamically stable and dominant for homo- and heteroepitaxial growth of lattice matched materials.

- $\gamma_i + \gamma_f \gg \gamma_s$ 3D island growth (no wetting), also termed Volmer-Weber model (VW). This nucleation mechanism is considered to be thermodynamically unstable and prevails when film and substrate materials are structurally and chemically highly mismatched [174]. The adatoms are stronger attracted to each other than to the substrate [176]. As a result, individual nuclei grow dispersed [91] on the surface before reaching a critical size where coalescence occurs.
- $\gamma_i + \gamma_f \geq \gamma_s$ layer-by-layer followed by island growth described by the Stranski-Krastanov model (SK). This intermediate model is generally accepted for low-lattice mismatched systems [174]. Initial monolayer layers grow under thermodynamically stable conditions [174] and result in a strained monolayer to match the substrate [176] covering the surface [173]. The strain energy increases with the number of strained layers. The system thus becomes unstable with increasing film thickness due to the increased interface energy [176]. Consequently, the film growth is shifted to 3D growth [174].

The growth conditions can be shifted by changing γ_i [175]. This can be achieved by carefully matching the substrate with the film material. The interface energy γ_i is lower when the substrate and film share the same bonding nature (covalent/ionic/metallic). Furthermore chemical reactivity lowers γ_i , which can be achieved by curing or peening the substrate or film surface. The former and latter influence the ability of the substrates to dissociate oxygen molecules that condense from the gas vapour [172] during AZO deposition. Low reactivity causes the formation of peroxides, resulting in a non-reactive interface which impedes the initial growth [172]. On the other hand, a reactive surface can dissociate the oxygen molecules and promote growth [172].

Heterogeneous nucleation at sites of defects, steps and contamination is favoured because γ_i is lower on these sites. With respect to the investigation carried out, the glass substrate is amorphous with short-range order. The atomic “disorder” is thus expected to lower γ_i . The surface roughness and structurally modified regions are also expected to change γ_i .

Initial island growth is followed by competitive growth of differently oriented neighbouring islands in AZO [91, 173]. Ellmer et al. observe an approximately 2-3 nm amorphous nucleation layer of ZnO sputtered on different substrates [172]. The thickness of the amorphous layer and polycrystalline film is changed by optimizing the deposition parameters.

Structure zone model The structure zone model gives the relationship between polycrystalline films quality and deposition temperature and pressure. The polycrystalline

film properties vary when transitioning from low (high) to high (low) temperature (pressure) sputtering parameters [173, 175, 178]. Figure 5.2 shows the different zones I, T and II used to distinguish the films [173, 175, 178].

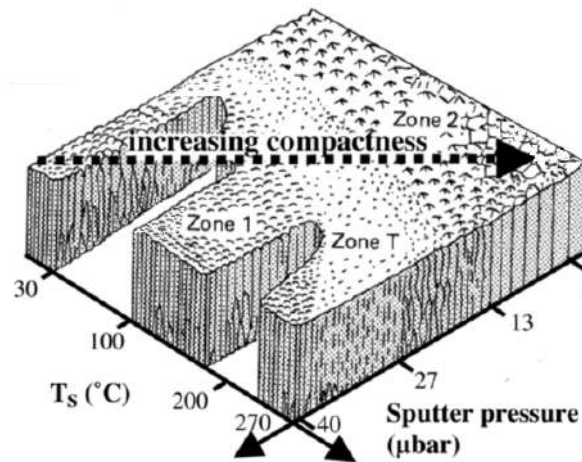


Figure 5.2: Structure zone model of AZO sputtered with varying substrate temperatures and deposition pressure [178]

- Zone I is characterised by porous layers with tapered crystallites due to low ad-atom mobility (slow surface diffusion) and shadowing of incident adatoms by the surface roughness.
- Zone T is a transition phase between zone I and II and is characterised by dense fibre-like grains.
- Zone II results in dense continuous columnar grains due to high ad-atom mobility. Particularly for rough surfaces, the high mobility compensates the shadowing effect. Hence growth is mainly controlled by diffusion of adatoms on the surface which results in more dense layers with small columnar grains.
- Zone III (not shown at $T > 270^\circ\text{C}$ and partial pressure $< 1\mu\text{m}$) conditions at low pressure and high temperatures allow the recrystallization of grains. Bulk diffusion and coalesce leads to formation of larger grains.

In this study, depositions were carried out at high temperatures of 350°C and a low pressure of 6×10^{-3} mbar. Thus, a growth within Zone II and III is expected. Since the deposition parameters were kept constant, the AZO film microstructure is expected to be mainly dependent on the substrate surface geometry, film bulk and surface diffusion, thermal expansion and lattice mismatch [175].

5.2 Microstructure

Figure 5.3 shows an example of a baseline corrected and normalized XRD pattern of an AZO film and theoretical reflexes for a wurtzite structure [179]. For all the investigated films, the diffraction of the (002) plane was the most significant which indicated a preferred c-axis orientation. Other studies show that the (002) orientation is preferred over other planes already during initial growth [180] and competitive growth of islands [91].

Coalescence of islands leads to a columnar growth of polycrystalline films perpendicularly to the substrate plane and with an inclination towards the sputtering flux direction [181]. One possible explanation for the preferred growth orientation is the low surface energy of (002) compared to other facets [180]. The low energy facets grow parallel to the substrate normal in a thermodynamically stable system [173, 180]. In addition to that, the effect is increased with rising binding energy between the film and the substrate [180].

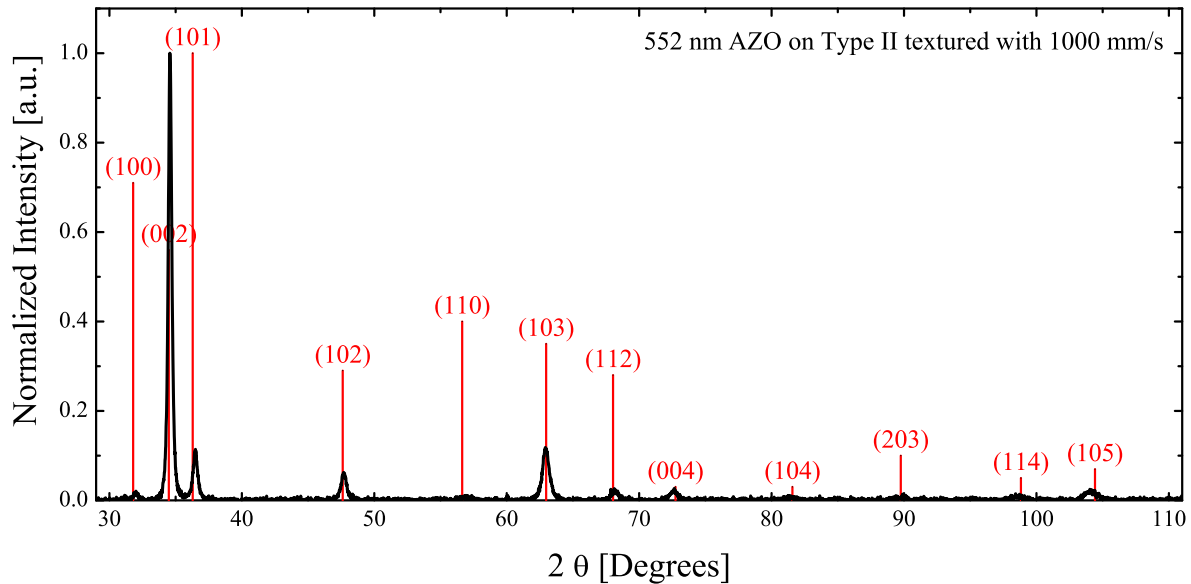


Figure 5.3: XRD pattern of 552 nm AZO film deposited on a glass substrate scribed with 1000 mm/s following baseline correction and normalisation to the highest intensity. theoretical reflexes expected for a wurtzite ZnO structure are shown and indexed by the red vertical lines[179]

Figure 5.4 shows SEM images of the AZO films on differently textured substrates. The cross section of the 75 nm film (5.4a) deposited on a periodically textured glass substrate (top) suggested that the growth was compact and columnar. Compact small grains (bottom) and a low density of small islands were indicated on the surface. The lateral dimension of the grains increased with rising film thickness. Figure 5.4b shows the grains were bigger for the 552 nm film in comparison to the 75 nm film (5.4a).

The intensity and full width at half maximum (FWHM) β_{hkl} of the (002) reflex increased and decreased with increasing film thickness, respectively. The reflexes of the AZO films on highly textured substrates had a lower intensity and broader β_{hkl} in comparison to periodically textured substrates. The measured reflex intensity is influenced by

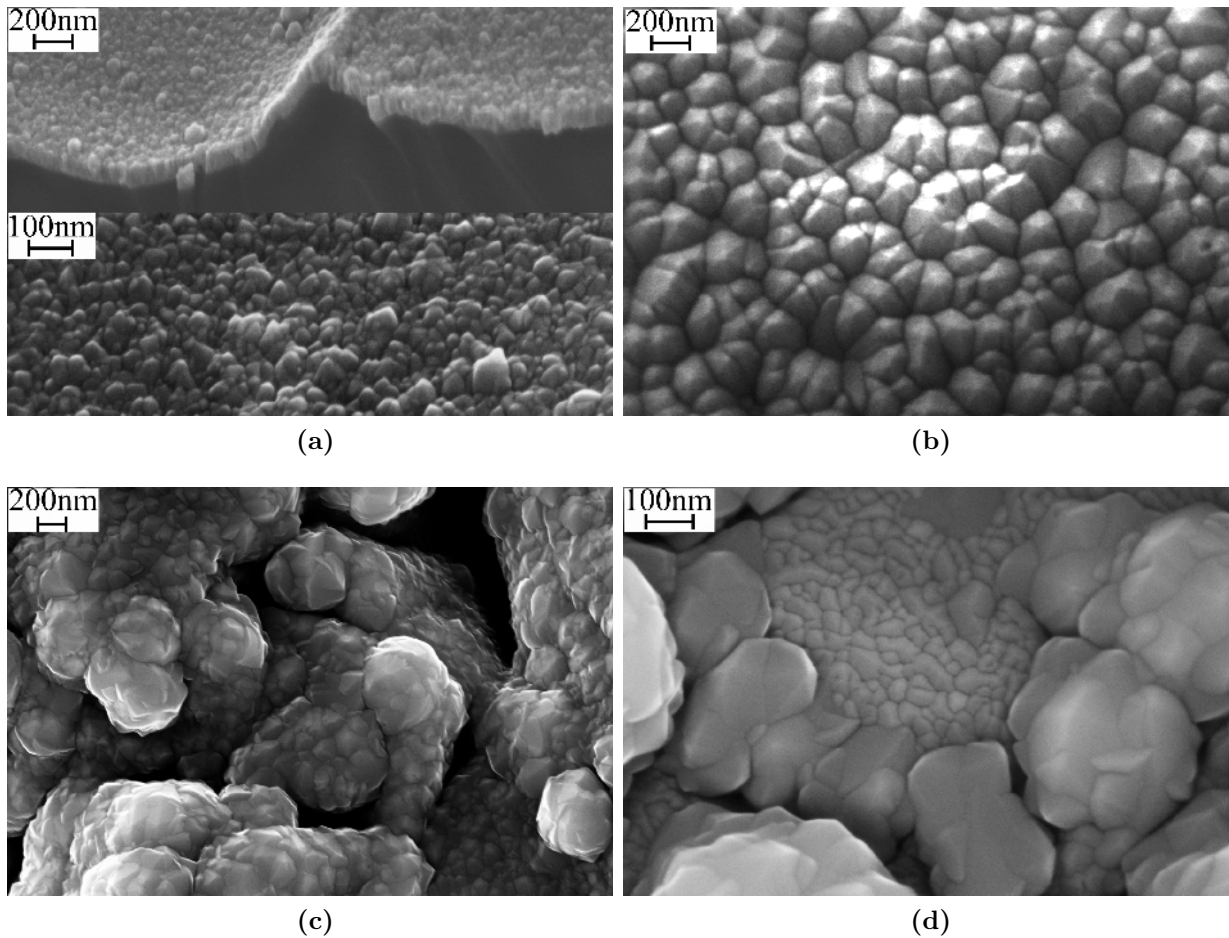


Figure 5.4: Scanning electron microscope (SEM) images of the investigated AZO films. (5.4a) cross-section (top) and view (bottom) of the 75 nm film on a periodically textured glass substrates, (5.4b) (002) oriented crystallites, grain boundaries and voids in a 552 nm AZO film and (5.4d) different crystallographic oriented planes and (5.4c) showing coalesce of crystallites

several substrate properties and film quality such as surface roughness and voids, respectively. Figure 5.4c shows a 552 nm AZO on a highly textured 1000 mm/s substrate. The SEM image indicates that coalescing of crystallites and grains formed occasional voids at unfavourable angles of intersection.

The intensity of the reflexes from planes such as (100), (101), (102), (110), (103), (112), (004), (104), (203), (114) and (105) increased with increasing glass surface texture for all the investigated film thicknesses. Figure 5.4d shows a 552 nm AZO film deposited on a glass substrate scribed at 1600 mm/s. The film shows crystallites with different crystallographic orientation and coalesced grains. Moreover, the different orientations suggest that the crystallinity of the substrates is reduced.

5.2.1 Grain properties and Strain

Figure 5.5 shows the crystallite size D and strain ε for the different film thicknesses as a function of the laser texturing scribing speed, respectively. (The Scherrer and Williamson

Hall method used to determine the former and latter are detailed in Chapter 3, Section 3.5.2). The results showed that the crystallite size decreased with decreasing scribing speed. Thereby, the strain in the films on highly textured substrates was higher in comparison to the periodically textured and reference substrates, respectively.

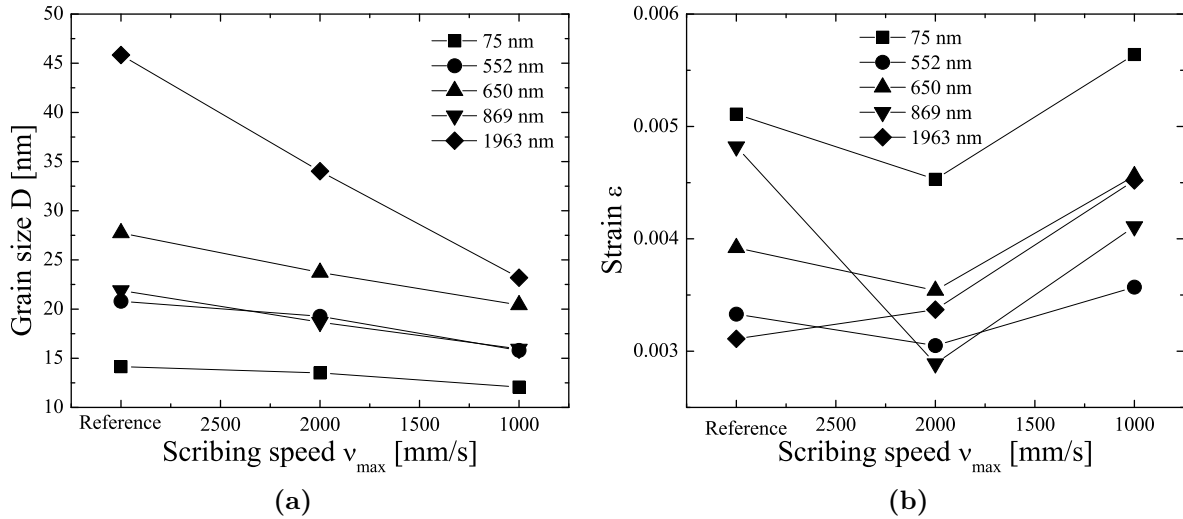


Figure 5.5: Crystallite size D(5.5a) and (5.5b) strain ϵ as function of the scribing speed and AZO film thickness

This might be because the increasing surface texture causes step defects, which lower the interface energy and favour heterogeneous nucleation [175]. As a result, differently oriented crystallites grow. It is however possible, that other factors such as stress caused by impurities contribute to the strain (Chapter 3, Section 3.9b). The stress in the films is assumed to consist of the two components (I) intrinsic stress introduced by impurities and defects in the crystal and (II) extrinsic stress introduced by the lattice mismatch and thermal expansion coefficient mismatch between the film and substrate [86]. The former and latter might be applicable to the investigated glass substrates and is discussed in the following sections.

5.2.2 Impurities and defects in the crystal

Al_2O_3 and ZnO contents of the target were kept constant during the deposition. It is possible that excess Al or Zn diffused from the textured glass substrate surface and was incorporated into the films. Bhardwaj et al. show that densification during laser ablation in glass is accompanied by ion migration [56]. It is possible that ionized elements are increasingly present on the surface with increasing texture.

Taking the glass composition into consideration, these can include ions from the glass former such as Al^{3+} , B^{3+} and O^{2-} and modifiers such as Cl^- , Na^+ , Ca^{2+} and Mg^{2+} . Element mapping by energy-dispersive X-Ray (EDX) spectroscopy demonstrated a variation

in the distribution of the latter elements, along with potassium (K), carbon (C) and silicon (Si). Figure 5.6 shows an example of the 75 nm AZO deposited on a glass substrate scribed with 2600 mm/s.

SEM cross-section image (5.6a) shows an edge of a crater with a conform region demonstrating variation in the glass composition. The region is assumed to be the heat-affected zone (HAZ) during laser ablation. For a better overview, the AZO/glass interface is marked by the solid red line. EDX images show that Zn (5.6b) is mainly detected in the AZO film and a very low content is homogeneously distributed in the glass substrate. Detected O content (5.6c) on the other hand is higher, but with an inhomogeneous distribution extending beyond the HAZ in the bulk substrate. Interestingly, a higher Al content is detected in the HAZ than in the film and rest of bulk material. It should be noted that the elements might also diffuse between the film and substrate during measurements. However, a correlation with the HAZ and element distribution makes the observation plausible.

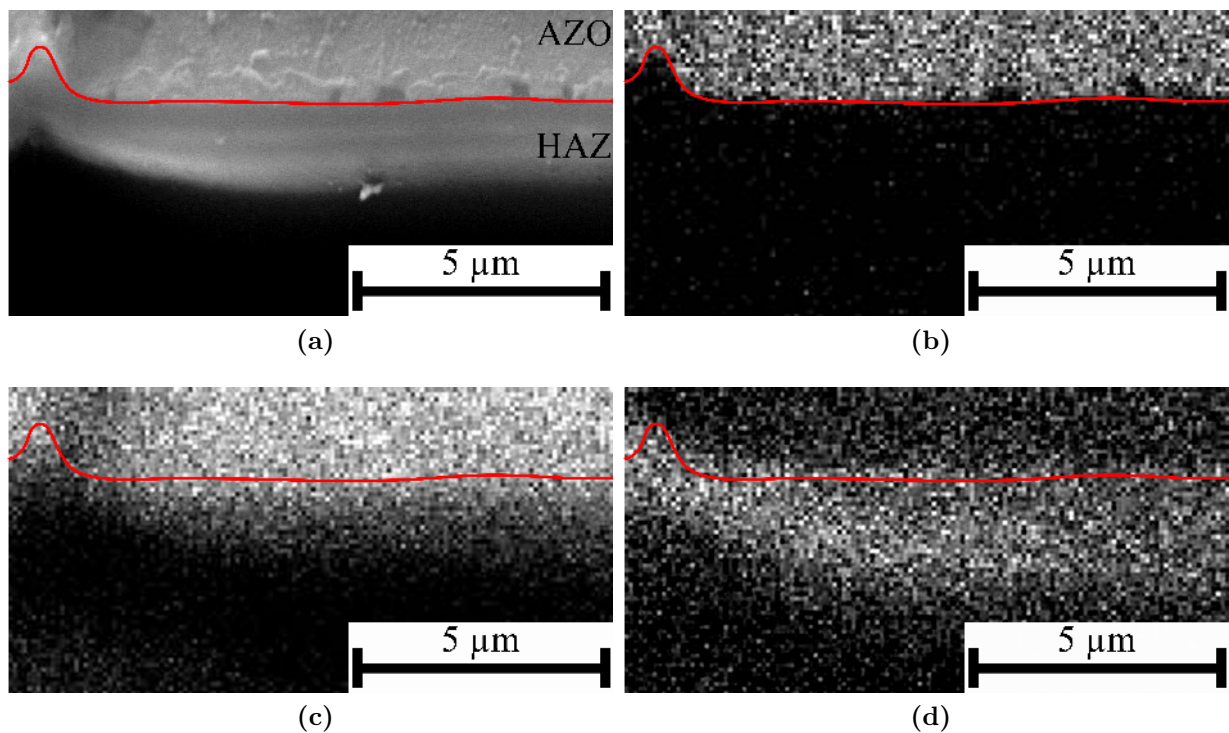


Figure 5.6: Scanning electron microscope (SEM) image of 75 nm AZO films on a 2600 mm/s textured glass earth alkaline aluminoborosilicate glass (5.6a) and the corresponding energy dispersive X-ray spectroscopy (EDX) showing the distribution of (5.6b) Zn (5.6c) O and (5.6d) Al in the films and glass substrate

The distribution of the elements is expected to increasingly vary with increasing texturing. Foreign elements diffusing into the AZO film can either act as contaminants or dopants, depending on their nature. The extent of the influence depends on the element properties such as atomic or ionic radius, charge and the defects resulting from their

incorporation into the crystal lattice. Studies show that ZnO, which is intrinsically n-type, has a high compressive stress (2.43×10^9 N/m²) with predominant Zn interstitials in nonstoichiometric pure ZnO [86]. Excess Zn diffusing into the AZO film might also cause a similar effect. Studies show that for ZnO homoepitaxial growth, the Zn atoms evaporated from the Zn-face at low temperatures around 380 °C [182]. Deposition in this investigation was carried out at 350°C which might also induce Zn diffusion from the glass into the growing AZO films and possibly act as a contaminant.

Incorporating 1% Al into ZnO reduces the compressive stress to 1.34×10^9 N/m² [86]. Substitutional defects resulting from Al³⁺ with an atomic radius of 0.039 nm taking the place of Zn²⁺ with an ionic radius of 0.06 nm in the crystal shortens the c lattice parameter [86]. Other cations such as Mg²⁺ with an atomic radius of 0.057 nm and Na⁺ (0.099 nm) can also substitute Zn²⁺ [183–185]. Al shortens the c lattice parameter, alleviates the residual compressive stress and decreases the resistivity [86]. This could be a possible explanation for the slightly reduced strain in films on periodically textured substrates in comparison to the reference and highly textured substrates, respectively.

Defects and imperfections in the crystal structure cause formation of grain boundaries and thus reduce the sizes of the grains. However, Cebulla et al. report improved crystalline quality following addition of Al to ZnO [96]. They attribute the observation to the beneficial role of Al as a surfactant in the growth process. Surfactants reduce the substrate-film interface energy and promote FM layer-by-layer growth.

Lu et al. [86] propose a different model called stress-release mechanism which correlates the stress with the grain size. In this model, the decrease in the stress is accompanied by an increase in grain size. Reduced stress is assumed to (I) alleviate stress-induced defects such as dislocations in film thus improving the crystal perfection and (II) as an alternative mechanism to islands formation, for relieving the strained system to promote two-dimensional 2D growth. It is possible that both models apply to the investigated films and further alternative mechanisms could be responsible for the observation as discussed in the following sections.

5.2.3 Lattice and thermal expansion mismatch

laser-textured glass substrates surface morphology was changed as suggested by HAZ in the SEM cross-section images (figure 5.6) and indicated by the AFM phase-contrast images. The substrate local chemical environment changes the cantilever tip-sample interaction during the discrete tapping mode measurements. Increased and decreasing phase shifts when probing an inhomogeneous substrate are attributed to increasing and decreasing stiffness of the material, respectively [125, 126].

Stiffer materials show a lower thermal expansion coefficient. Higher mismatch in the linear thermal expansion coefficients between film and substrate increases thermal strain component in the film. The linear thermal expansion coefficient of float glass is around

$\alpha_{glass} = 9 \times 10^{-6} \text{ K}^{-1}$ and that of a of ZnO $\alpha_{ZnO} = 4 \times 10^{-6} \text{ K}^{-1}$ [96]. The results suggested that Type I was stiffer than Type II and III following ablation. Furthermore, highly textured substances were also suggested to have a higher material stiffened. The linear thermal expansion coefficient is assumed to be lowest in Type I and highly textured substrates. It is therefore possible that the periodically textured substrates show reduced strain, due to a lower thermal expansion, which is closer to that of ZnO in comparison to the flat reference and highly textured substrates.

Lattice mismatch and thermal expansion also play a significant role in thin-film growth. Periodically textured substrates could have a lower thermal expansion, which is better matched with that of the AZO films. This could explain the reduced strain compared to the flat reference, particularly for 75 nm AZO. Similarly, much lower or higher mismatch, as possible for the reference could induce a high strain.

Bulk morphological changes were suggested by Raman spectra and Ellipsometer data. The results suggested that laser scribing at low pulse energy (E_p) and high scribing speed (ν_{max}) increased the number of three- and four-fold boroxol rings or alternatively the Si-O-Si linkages in the glass matrix. At high E_p and low ν_{max} , randomly textured substrates suggested that the number of five- and six-fold boroxol rings or alternatively orthosilicate species increased in the glass matrix (table 4.3).

The S-O bond length in isolated units is longer (0.163 nm) than in the framework (0.161 nm) [186]. Assuming the surface is affected in a similar manner, this could explain the higher strain in the films on flat reference compared to textured substrates. Studies show that ZnO strain and dislocation density can be reduced when substrates with a similar lattice (a=0.325 and c=0.5213 nm) are used [182]. Crystallographic defects are formed at interfaces of highly mismatched systems. Such defects cause electronic defect states within the band gap which can act as recombination centres [172].

Increasing film thickness relaxes the strain as the grain boundaries migrate and are reorganized [175]. Grains furthermore coalesce to reduce the surface tension with increasing deposition time at elevated deposition temperatures. Crystallinity, grain size and defects influence the mobility and concentration of charge carriers in the film, which in turn affects the resistivity [86, 96]. As a matter of fact, the resistivity of the front contact is an important parameter for the use in thin-film solar cells, because it influences the solar cells series resistance. It is therefore important to investigate and understand the electrical properties of the films.

5.3 Electrical properties

The sheet resistance R_s of the films was characterised by four-point probes to determine whether the electrical properties were significantly different. Hall measurements were then carried out using the van der Pauw method to give a better understanding of the electrical

properties of the films. Figure (5.7) shows the resistivity ρ of the AZO film thicknesses 75, 552, 869 and 1963 nm.

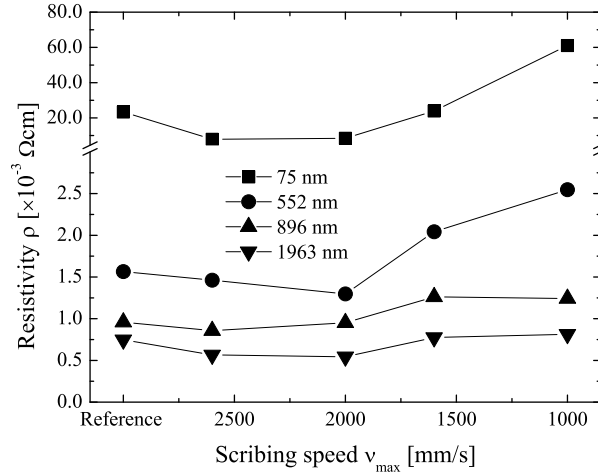


Figure 5.7: Resistivity ρ of the AZO films from co-deposition on flat reference and textured glass substrates.

The resistivity of the films on periodically and randomly textured substrates decreased and increased in comparison to the reference, respectively. The difference between the reference and periodic texture was estimated to be $\approx 1 \text{ k}\Omega/\square$. These values were higher than the determined error, and suggested a significant change in the resistance of the films on the differently textured substrates. The difference between the AZO film resistance measured on differently textured substrates was however suggested to decrease with increasing film thickness. For the $\approx 2 \mu\text{m}$ film, the difference of merely $< 1 \Omega/\square$ was determined.

One possible explanation for the observations is the changed film thickness on the differently textured substrates as a consequence of the changed step coverage. Another possible explanation is the changed carrier concentration and mobility. The former and latter aspects are discussed in the following sections.

5.3.1 Charge carrier concentration and hall mobility

Figure 5.8 shows the charge carrier concentration n_e and Hall mobility μ_H of the AZO films as a function of the scribing speed and film thickness. The results suggested that the charge carrier concentration (5.8a) slightly increased with increasing film thickness. The variation remained within the same magnitude (10^{20} cm^{-3}). Minimal enhancement was observed in the textured substrates in comparison to the reference. The highest enhancement was observed for the 75 nm AZO film where n_e was suggested to be about $5.7 \times 10^{19} \text{ cm}^{-3}$ on the flat reference substrate and $\approx 1.2 \times 10^{20} \text{ cm}^{-3}$ on textured substrates. The carrier concentration of the films with the same thickness on the differently textured substrates was similar.

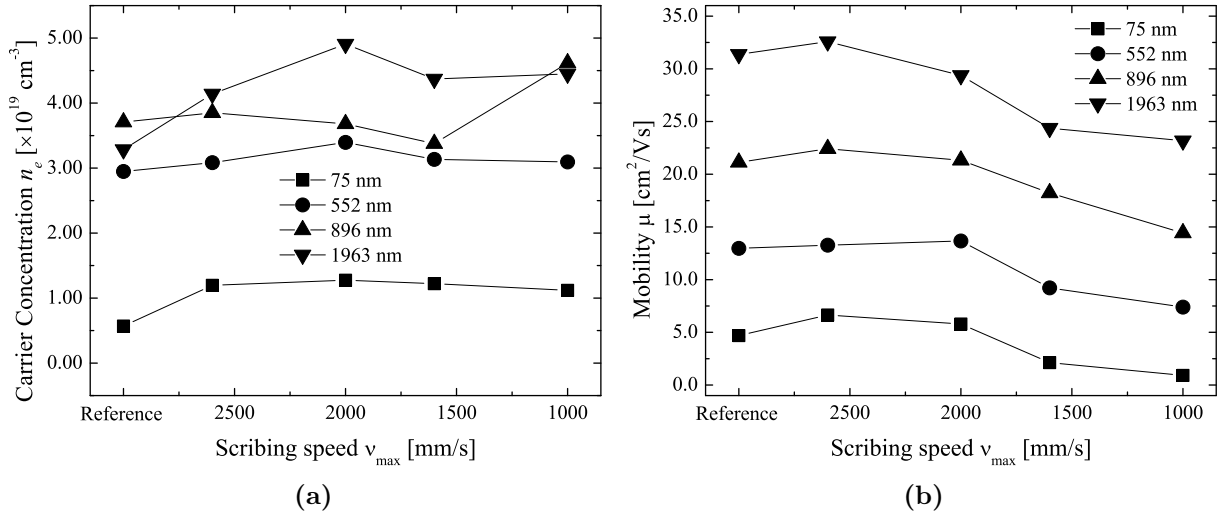


Figure 5.8: (5.8a) charge carrier concentration n_e and (5.8a) Hall mobility μ_H of the AZO films from co-deposition on flat reference and textured substrates at different scribing speeds

The mobility (figure 5.8b) increased with increasing film thickness. For films with the same thickness, a slight increase was observed on slightly textured substrates compared to the reference. The electron Hall mobility in the 75 nm film on the flat glass reference increased from $4.69 \text{ cm}^2/\text{Vs}$ to $6.64 \text{ cm}^2/\text{Vs}$ on the periodically textured (2600 mm/s) glass substrate. The mobility decreased with increasing surface texture, particularly in thinner films. As an example, the Hall mobility of the 75 nm film on the glass substrate textured with 1000 mm/ dropped to $0.913 \text{ cm}^2/\text{Vs}$. The change in the mobility can be a consequence of changed electron scattering mechanisms as discussed in the following sections.

5.3.2 Scattering mechanisms

The mobility in polycrystalline AZO is limited by several scattering mechanisms which include neutral impurity μ_n , ionized impurity μ_i , grain-boundary scattering μ_g and lattice vibration μ_l scattering [86, 187]. Studies show that μ_l dominates in high temperature regimes, and can be neglected at room temperature [86, 171, 187]. The scattering mechanisms contributing to the Hall mobility can therefore be reduced to

$$\frac{1}{\mu_H} = \frac{1}{\mu_n} + \frac{1}{\mu_i} + \frac{1}{\mu_g} \quad (5.1)$$

In doped oxide films, the observed neutral impurities are low, thus μ_n is also commonly not considered [86, 187]. On the other hand, the deflection of the electrons by the charged impurities results in μ_i having a major contribution [171] and this mechanism is considered to be applicable to the investigated films due to the following reasons.

The investigated AZO films were intentionally doped with 2 %wt Al_2O_3 as demon-

strated by the high charge carrier concentration (10^{20} cm^{-3}). Substitutional defects resulting from Al^{3+} or other cations with a higher charge taking the place of Zn^{2+} in the crystal increases the conductivity due to the surplus positive charge. This is the desired and aimed effect of intentional doping to obtain n-type ZnO.

It is however possible that Al or different impurities diffuse from the glass substrate into the AZO films during growth and increase μ_i . Periodically textured substrates can for example demonstrate this effect and explain the improved electrical properties in comparison to the reference.

Other cations such as Mg^{2+} and Na^+ can also substitute Zn^{2+} , but result in a p-type conduction with O^{2-} governing the charge transport [188, 189]. This effect can however be ruled out or might only play a minor role, since the Hall-measurements showed a negative voltage for all the samples, demonstrating the films were all n-type.

Further defects include interstitial defects, which are however more common for smaller elements such as hydrogen. Also intrinsic defects from excess Zn ions from the glass substrates might increase the impurity scattering.

Another scattering mechanism, which is expected to play an important role, is the grain-boundary scattering μ_g , particularly for films with small grains [86]. The investigated films had crystallite sizes $D \geq 10 \text{ nm}$. For free electrons to be scattered at the boundaries, their mean free path must be higher or in the range of the grain sizes. The free-electron mean path can be calculated by [187]

$$L = \left(\frac{h}{2e} \right) \left(\frac{3n_e}{\pi} \right)^{1/3} \mu_H \quad (5.2)$$

where h is Planck's constant and e the electron charge. $L \leq 4 \text{ nm}$ was calculated for investigated films investigated as shown in figure 5.9. These are magnitudes smaller than the grain sizes observed in all the films (figure 5.4). The grain-boundary scattering μ_g can therefore be ruled out as an explanation for the observed high resistance in the films on highly textured substrates. The step coverage is discussed in the following section.

5.3.3 Step-coverage

Sommer et al. also observe a higher and lower charge carrier mobility in AZO films sputtered on U-shaped and V-shaped substrates in comparison to the reference, respectively. They attribute the increased resistivity to the increased grain boundaries in the 600 and 700 nm AZO films deposited on the V-shaped substrates [181] and attribute the higher mobility in U-shaped textures to reduced growth disturbances [181].

Although the dimensions of the textures in this study are greater, the rounded and highly textured substrates crater showed a similar behaviour to the U- and V-shaped textures, respectively. The observed improvement in AZO quality on periodically textured

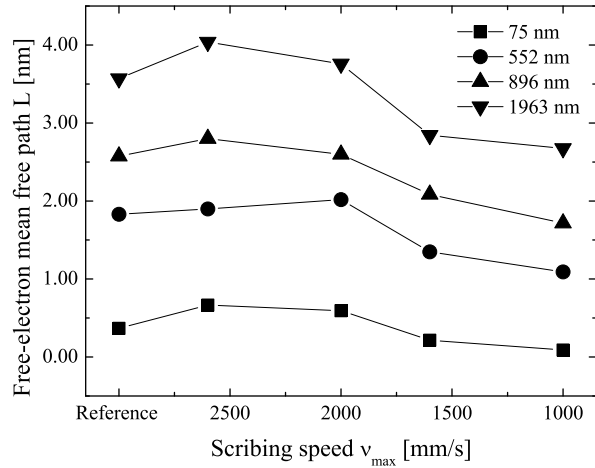


Figure 5.9: Free-electron mean path L of the AZO films from co-deposition on flat reference and textured substrates scribed at different scribing speeds

substrates could thus be a consequence of improved step coverage. Figure 5.10 shows a schematic of the variation in film thickness homogeneity as a function of the surface texture.

Sharp edges (5.10a) cause overhangs and their shadowing effect results in inhomogeneous films on the walls. Consequently, microcracks are formed at texture intersections. High aspect ratio geometries lead to poor coverage of the side walls [190]. Most incident adatoms strike the texture peaks and only a few reach the valleys [175].

Tapered walls (5.10c) improve coverage, which can further be increased with the angle of inclination α (5.10d). Smy et al. demonstrate that the uniformity of the film thickness on the side wall of trenches improves by 15% by tilting the geometry angle (5.10d) from 90° to 82.58° [190].

In the sputtering process, the high energetic adatoms from the target strike the substrates surface [181] from various angles. Energy and distribution of the flux, as well as noise in the flux influence the resulting quality of the films [175]. The angle between the particle flux and the substrate normal influences the orientation of the crystalline columns. Column axis is inclined from the substrate normal to the direction of the particle flux [181].

The textured substrates thus influence the angle of incidence of the adatoms depending on the geometry of the surface. Furthermore, the angle of incidence, surface geometry as well as the aspect ratio are important parameters which influence step coverage. The surface texture also influences ad-atom surface mobility, which is important for the relocation to lower energetic sites. An increased diffusion would lower the energy barrier and promote nucleation, while a reduced diffusion would impend the nucleation. Bulk diffusion is also affected. Grain boundary migration is necessary for recrystallization of the films, which enhances the polycrystalline film quality [175].

Rounder edges (5.10b) reduce the shadowing effect and improve the isotropic growth.

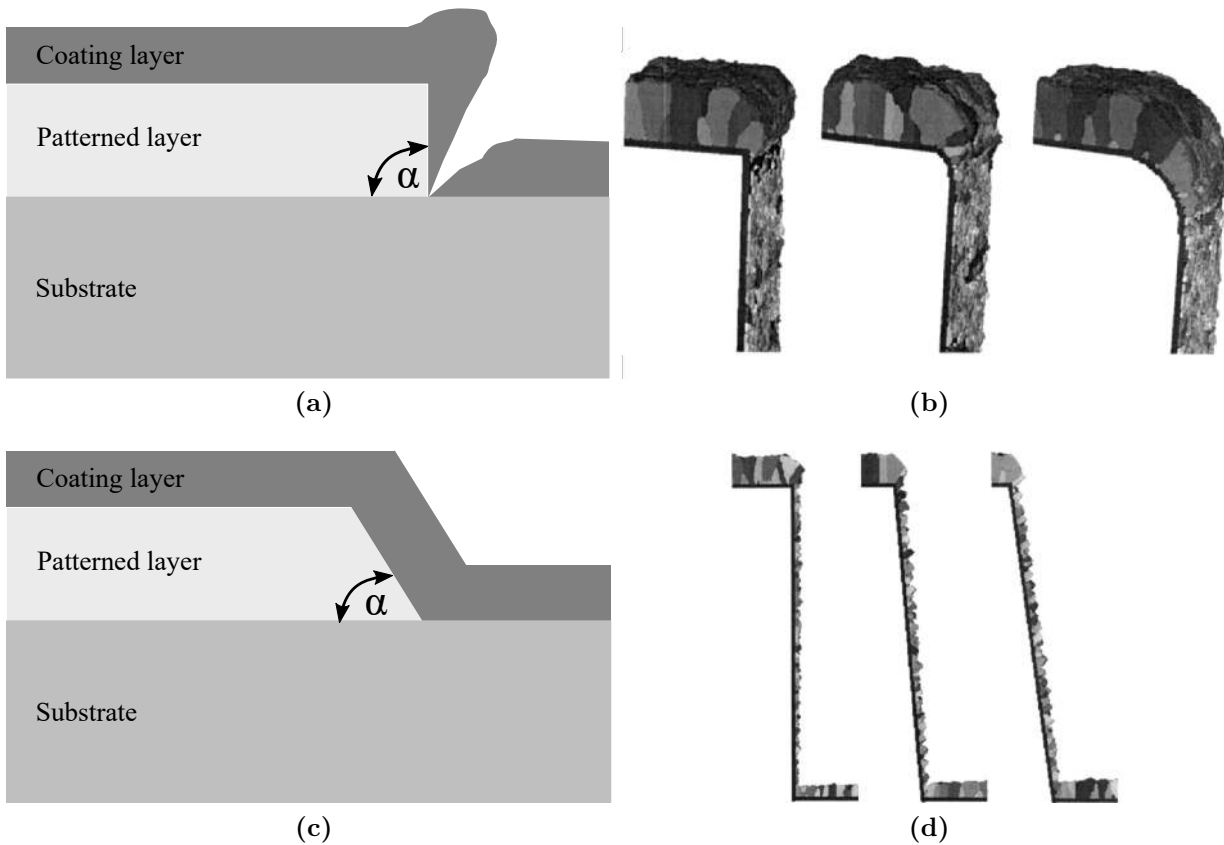


Figure 5.10: Film thickness uniformity variation with changed step coverage (5.10a, 5.10c [174]) on different surface geometries (5.10b, 5.10d[190]). Bad coverage (5.10a) of sharp edges leads to anisotropic film growth and microcracks. Isotropic growth is promoted by (5.10b) smoother edges and (5.10c) inclined walls with (5.10d) an increasing angle of inclination α .

Also, rounded edges, as observed for crater profiles (5.10b) reduce the formation of overhangs, which lead to inhomogeneous film thickness growth along the walls of the trenches [190]. This reduces the porosity of the film, improves the quality [190] and might explain the observed improved electrical properties in the periodically textured substrates.

The high surface roughness and porous films show favourable conditions for nitrogen and oxygen chemisorption [86]. Integration of these elements at the grain boundaries increases the barrier height and thus lowers the carrier mobility [86]. This could be applicable to the highly textured substrates. In these films microcracks, voids, cusps and interruption or film instability [190] greatly impend the mobility of free electron, and thus increase the resistivity of the films.

With increasing film thickness, the voids are more likely to be filled through coalescence of polycrystalline films. This might explain the observation that the thicker films ($>1\mu\text{m}$) on all substrates demonstrated similar properties. These observed differences in the electrical and structural properties further influence the optical properties of the films, which are important parameters for solar cell generated photo current density. Therefore, the optical properties were analysed and discussed in the following section.

5.4 Optical properties

The transmission of the substrates was measured with the light first striking the AZO film, then the glass substrate to be able to deduce the thin-film properties. The results are illustrated in figure 5.11. The reference glass/AZO substrates for two different film thicknesses are compared to Type II reference glass substrate (5.11a). The results show that the transparency decreases in the UV region due to the absorption in the AZO film. The presence of interference fringes indicates that the layer stack surfaces are optically smooth. Increased (double) AZO thickness does not affect the absorption in the UV region, but rather reduced the transparency in the visible region.

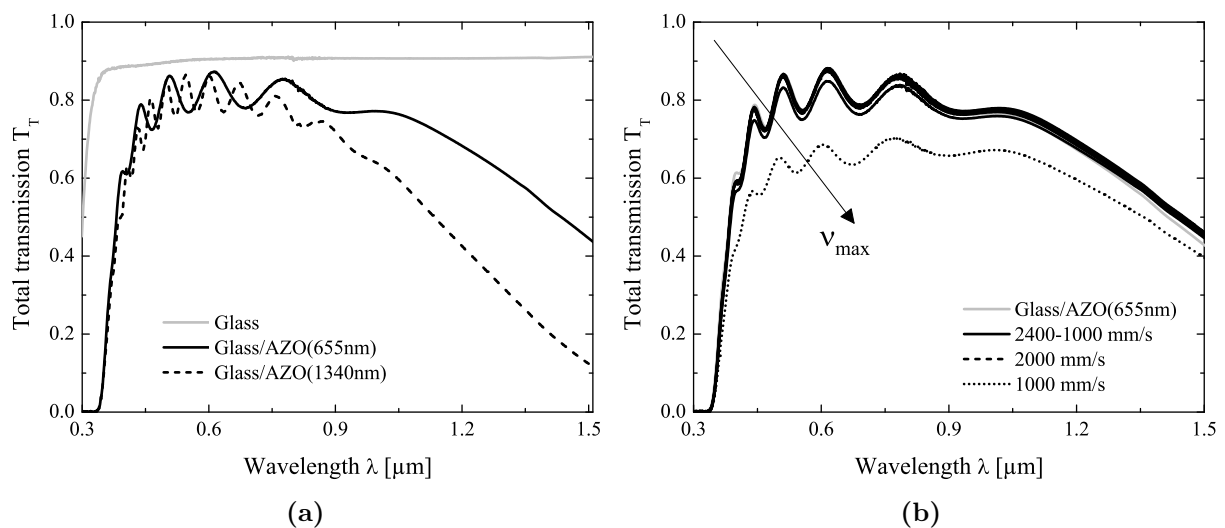


Figure 5.11: Type II glass substrates (5.11a) transmission of the reference coated with different AZO thickness and (5.11b) 650 nm AZO on glass substrates textured with a constant pulse energy $E_p=115 \mu\text{J}$ and varying scribing speed from 2400-400 mm/s.

The influence of the differently textured substrates is therefore only discussed for the 650 nm AZO film thickness. The transparency of the AZO films in the visible spectrum decreased with increasing texture (5.11b). A similar trend was observed in the transparency of the laser-textured glass substrates as discussed in Chapter (4), Section (4.1.4). The interference effects observed in the reference were also observed in the periodically textured substrates and decreased with increasing texture. This was attributed to increased light scattering of highly textured substrates in comparison to periodically textured and flat reference substrates with optically smooth surfaces. The light is effectively coupled into the AZO films and the absorption of the films is increased. It is because of this reason that the AZO films must be thin to avoid parasitic absorption, particularly when textured glass substrates are used.

The changed absorption tail inclination suggested that the optical band gap shifted [191]. For better comparison, the absorption coefficient of the films was used to determine the optical band gap. The optical band gap corresponds to the energy difference

between the valance and conduction band [86]. It can be determined by assessing the energy required to excite an electron from the valance band to the conduction band. The absorption coefficient is given by $\alpha = -\frac{1}{d} \cdot \ln\left(\frac{T}{1-R}\right)$ where d is the film thickness, T the transmission and R the reflection. AZO is a direct band gap semiconductor [192] and the absorption coefficient is related to the optical band gap by [192]

$$\alpha h\nu \sim (h\nu - E_g)^{1/2} \quad (5.3)$$

where h is the Planck's constant, ν the frequency of incident light and E_g the band gap. The optical band gap can then be deduced from the linear regression between $(\alpha h\nu)^2$ on the y-axis and $h\nu$ on the x-axis.

Figure 5.12 shows an example (5.12a) of the absorption coefficient and the linear regression used to determine the optical band gap of the 650 nm AZO film on a flat reference and substrates scribed with 2000 mm/s and 1000 mm/s scribing speed. The deduced E_g values are shown in (5.12b) as a function of the scribing speed. The results suggest that the optical band gap of the AZO films on periodically textured substrates decreases in comparison to the reference. A blue shift in the band gap is suggested for the highly textured substrates.

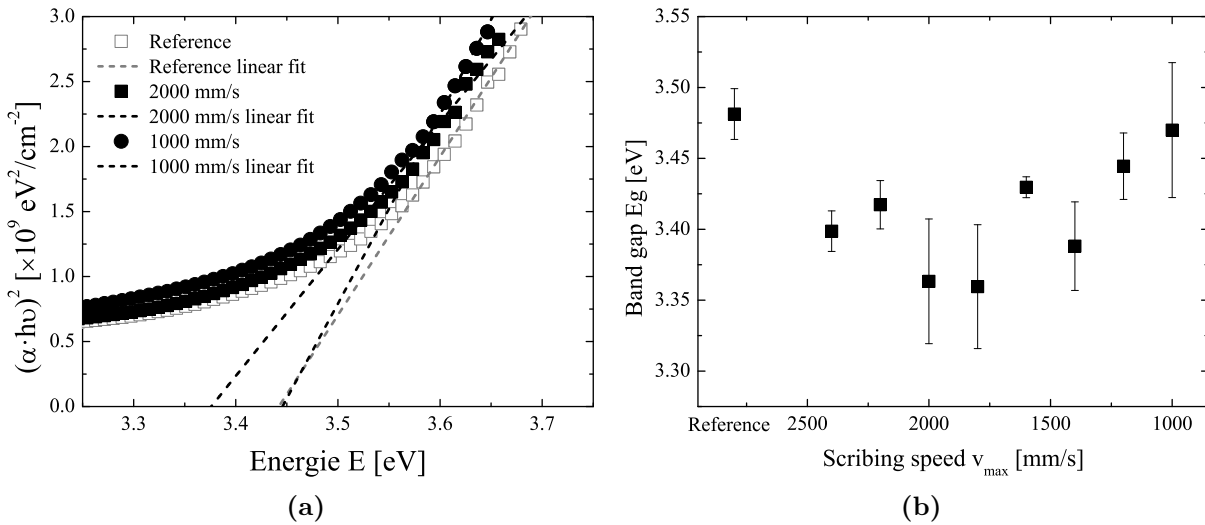


Figure 5.12: (5.11a) absorption coefficient and linear regression to determine the optical and gap of AZO on differently textured glass substrates and (5.11a) variation in E_g as a function of the scribing speed at a constant pulse energy $E_p=115\mu\text{J}$.

Liping et al. show that the band gap increases gradually with increasing stress in strained ZnO with varying Mg content [191]. They also observe that the increasing stress is accompanied by a slight increase in the electron effective mass of conduction band [191]. The Williamson-Hall analysis of the uniform deformation stress suggested that the strain in AZO films deposited on periodically textured substrates was lower in comparison to the highly textured substrates.

These results correlate with the observation made by Liping et. al. in AZO films with low strain [191]. They attribute the red shift in the films to the improved crystallinity [191]. Tan et al. attribute the blue shift to the amorphous phase in the ZnO films [192]. Moreover, they suggest that the amorphous phase causes an increase in the number of localized states extending in the conduction and valence bands [192]. The XRD analysis suggested that the amorphous content in the AZO films increased with increasing texture. This was indicated by the appearance and increased intensity of reflexes from planes other than the (002) and might be a further explanation for the observed changes.

To summarise, different AZO film thicknesses were deposited on differently textured glass substrates. The crystallite size of the AZO films decreased with increasing glass surface texture. The strain was lower and the electrical properties improved in the films on periodically textured substances in comparison to the randomly textured substrates and flat references, respectively.

A red and blue shift of the band gap of the AZO films was observed on periodically and randomly textured substrates, respectively. The red shift is attributed to improved crystallinity [191] and the blue shift to the amorphous phase in the ZnO films [192]. The light scattering of the substrates increased with increasing glass surface texture and the transparency decreased. The parasitic absorption in the AZO films was expected to be high because the textured glass surface couples the light into the AZO films. This is one of the main reasons why ultra-thin front electrodes are required. It is possibility that ions from the laser-textured glass substances diffuse [56] into the AZO films and influence the properties.

The suggested lower thermal expansion coefficient might be a possible reason for the increased and decreased strain in the highly and periodically textured substrates in comparison to the reference. Crystallographic defects are formed at interfaces of mismatched films and cause electronic defect states within the band gap which can act as recombination centres [172]. Step defects from the texture are furthermore assumed to lower the interface energy and favour heterogeneous nucleation [175], resulting in films with different crystallographic orientation. The improved electrical properties of the films on periodically textured glass substrates are assumed to result mainly from the improved step coverage. These substrates are expected to have higher density of void, which are gradually filled with increasing film thickness.

The electrical and optical properties of the AZO films influence the performance of the solar cells. In the following Chapter (7), the performance of silicon thin-film solar cells on differently textured glass substrates is discussed.

6 Silicon thin-film solar cells

Multi-component glass substrates were textured with a picosecond laser with varying scribing speed and pulse energy. The crater dimensions decreased with decreasing pulse energy and the surface texture was changed from periodic to random with decreasing scribing speed and increasing laser spot overlap, respectively. Light scattering increased with increasing texture. The optoelectronic properties of AZO improved and deteriorated on periodically and randomly textured substrates, respectively. In this chapter, the performance of silicon thin-film solar cells deposited on the differently textured substrates is discussed.

6.1 Application in thin-film solar cells

For the application of the investigated textures in thin-film solar cells, their optical behaviour has to be matched with the requirements of the solar cell configuration. The textures promise to be advantageous in different configurations. Transmission and light scattering are important for the application in the superstrate configuration (pin figure 2.1a). Section 6.2 demonstrates performance of pin aSi:H solar cells on the differently textured substrates.

The transparency of the substrate is not important for application in the substrate configuration (nip figure 2.1b). Highly textured substrates therefore have potential for this application. This would have the advantage that light reaching the back contact (the textured glass) would be diffuse-reflected back into the solar cell intensely. Such substrates also promise to be suitable for bi-facial configuration, where the light is incident from both sides. Limited transparency might be compensated by the additional illumination. The experimental realisation of aSi:H nip bi-facial solar cells on differently textured glass substrates was investigated and discussed in Section 6.3.

Simulation of the periodic texture in the micron range demonstrated that slight refractive index variation on the glass surface did not counteract light in-coupling [193]. Instead, periodic rounded and Gaussian crater texture showed the greatest influence and reduced the reflection. Crater dimensions comparable to the wavelength lead to a focused G_{opt} near the AZO interface. Distance of the focus point can further be varied by changing the diameter of the crater. This is an important aspect for the application of the geometry in multi-junction solar cells such as those consisting of amorphous (top-) and microcrystalline (bottom cell). While the spectral range below <700 nm is absorbed by the top cell, a focused behaviour of the range above 800 nm can lead to an increased absorption in the bottom solar cell. Furthermore, the folded absorber layer around the texture increases

the absorber material volume and thus the generated photo-current. This concept allows the use of even thinner absorber layers for both top-and bottom solar cells and has been effectively adopted to solar cells on textured AZO [194]. The experimental realisation of aSi:H/ μ c-aSi:H tandem solar cells on differently textured glass substrates was investigated and discussed in section 6.4.

It should be noted that neither AZO nor solar cell deposition were optimized for the textured substrates. Rather, the deposition parameters were kept constant and the substrates were the only variable in the deposition. The results of solar cells deposited on Type I, II and III textured with varying pulse energy and scribing speed are discussed.

6.2 pin aSi:H solar cells

Figure 6.1 shows SEM cross-section images of aSi:H on AZO coated laser-textured Type II glass. Isotropic growth nature of aSi:H [35] was observed on both periodically (6.1a) and randomly (6.1b) textured substrates. Randomly textured substrates demonstrated folded structures, which is advantageous in increasing the effective volume of the absorber material, while keeping the layer thickness thin. This would be a great advantage in reducing the Staebler-Wronski-effect [13] and retaining the conversion efficiency. Another added advantage of textured glass is reducing solar cells reflection.

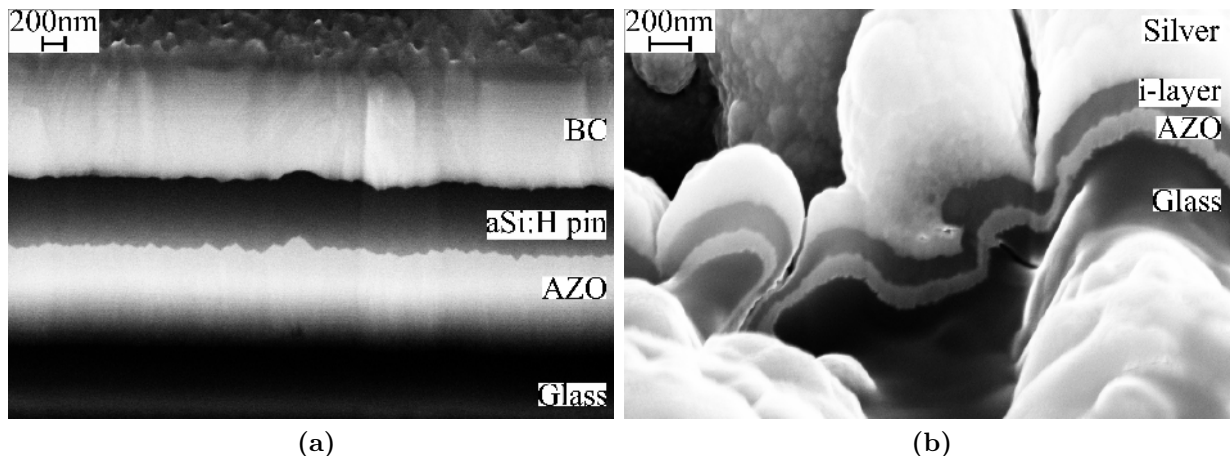


Figure 6.1: SEM cross-section images showing isotropic growth of aSi:H (6.1a) pin structure with about 300 nm thickness deposited on a periodically and (6.1b) and 175 absorber layer on randomly textured AZO coated glass substrate

Figure 6.2 shows decreased reflection of solar cells with increasing texture. Interference fringes were nevertheless evident, thus suggesting the light was not absorbed effectively. Solar cells in the configuration glass (texture), AZO (650 nm), pin (300 nm), Ag showed lower reflection particularly in highly textured substrates as shown in figure 6.2b. The cross-section of periodic, 2000 mm/s in figure 6.2b and random, 1000 mm/s in figure 6.1 surface topologies are shown and provide a better comparison of the solar cells.

The low reflection might be a result of increased effective absorber layer due to the folded structures in highly textured substrates. The effective light in-coupling however also increases the TCO absorption. The reflection fringes position is shifted to longer wavelengths on periodically textured substrates before shifting to shorter wavelengths with increasing textured. The reflection fringes position is shifted to longer wavelengths on periodically textured substrates before shifting to shorter wavelengths with increasing textured. This might be a result of the altered AZO and aSi:H film thickness on the differently textured glass substrates. The changed dispersion of the glass might however also contribute to this effect.

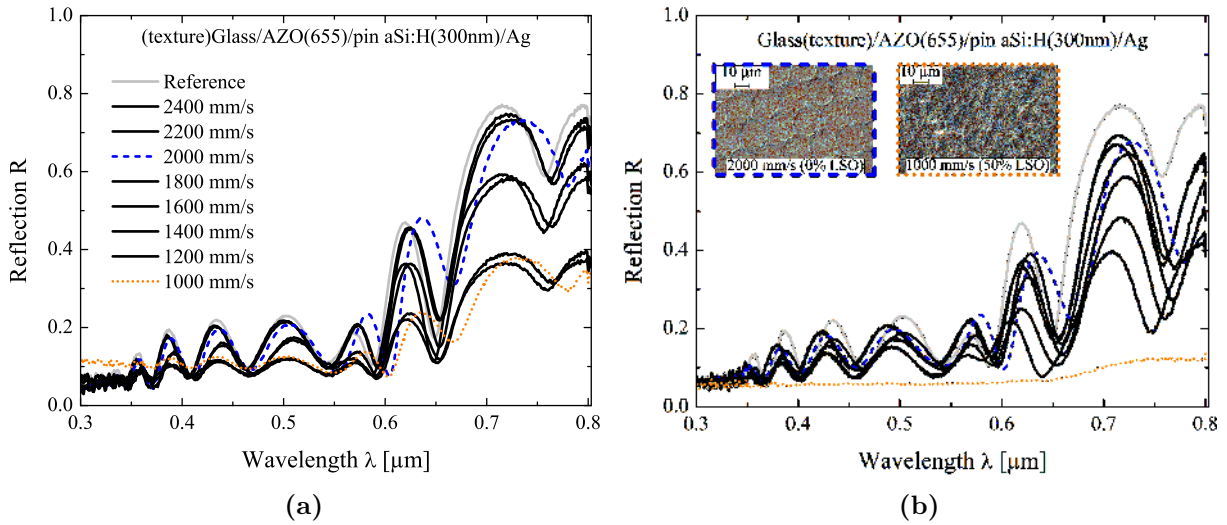


Figure 6.2: Reflection of the pin aSi:H solar cells deposited on the (6.2a) flat and (6.2b) textured side of AZO coated laser-textured Type II glass substrates.

Figure 6.3 shows an example of the EQE and 1-R of pin aSi:H solar cells deposited on textured Type I and III glass. The configuration studied was glass (texture), AZO (1200 nm), p-aSi:H (10 nm), i-aSi:H (250 nm), n-aSi:H (25 nm), AZO (100 nm), Ag (300 nm). Solar cell absorption increased with increasing texture for all investigated glass types. Also, the observed EQE showed less interference fringes with increasing texture. This was particularly true for substrates textured with narrower laser spots. For laser spots with wider diameters, a steep fringe was observed around 650 nm.

This was also observed in the simulation of periodically textured substrates (Chapter (7), section (7.2)). The simulations showed that the fringe reduced with decreasing AZO thickness. Experimental results further showed the fringes reduced with increasing texture. The fringe was thus attributed to variation in AZO film thickness.

Another interesting observation made in Type I was the slightly lower EQE of solar cells on the reference and Type III substrates. Assuming the electrical properties are comparable, this might be due to the more intense texture as suggested by the results discussed in Chapter (4), Section (4.1.3).

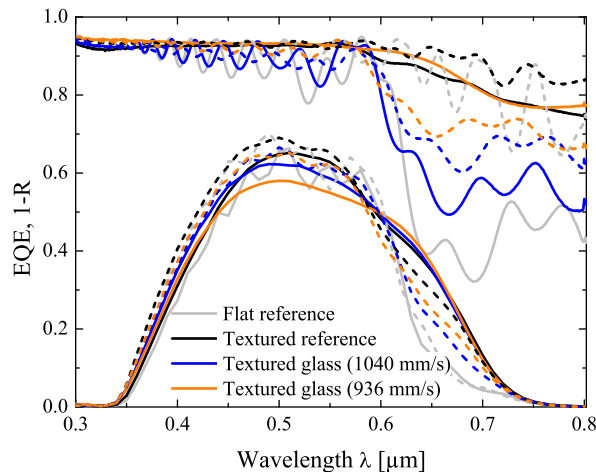


Figure 6.3: EQE of pin aSi:H on Type I (solid lines) and Type III (dashed lines) glass substrates textured with $7\mu\text{m}$ laser spot diameter at different scribing speed

To recall, AFM scans suggested the crater ablated under the same conditions were narrowest in Type I, followed by Type II and III. Crater heights were similarly steepest in Type I ($276.69\text{ nm} \pm 13.74\text{ nm}$), followed by Type II ($140.7\text{ nm} \pm 7.13\text{ nm}$) and III ($136.85\text{ nm} \pm 9.5\text{ nm}$).

It is therefore possible, that parasitic absorption of the substrates and AZO on the intense texture play a major role. Results shown in figure 6.3 are of a batch with a higher AZO film thickness of about $1.2\mu\text{m}$ to allow a better comparison to the wet-chemically textured AZO. Thus a reduction in AZO film thickness would greatly increase the EQE.

Figure 6.4 summarises the measured electrical properties of pin aSi:H solar cells deposited on Type I, II and III glass textured with 20, 12, 9 and $7\mu\text{m}$ laser spot diameter at varying scribing speed (filled symbols). The properties of the textured reference where the AZO is wet-chemically etched are shown by the open symbols. Note that the x-axis is labelled with the laser spot overlap (LSO), as the scribing speeds ν_{max} required to achieve the same overlap with the different laser spot diameter ω_0 are different. For example, to achieve a laser spot overlap of 50% for the 20, 12, 9 and $7\mu\text{m}$ laser spot diameters, scribing speeds of 1000, 600, 450 and 350 mm/s are required, respectively.

Solar cells on textured reference showed higher J_{SC} than the flat reference. Introducing periodic texture on the glass surface slightly improved J_{SC} before deteriorating with increasing texture. V_{OC} , FF and R_{series} showed a gradual decrease with increasing texture and R_{shunt} showed no tendency. The observed η remained steady for periodic texture before decreasing on randomly textured substrates.

Improved optical performance was attributed to increased light scattering of the textured films. Parasitic absorption in the substrate, AZO and Ag back contact however also increased on textured substrates and might explain the observed reduction in J_{SC} . The slightly improved V_{OC} might be a result of improved quality of the hydrogenated amorphous silicon (aSi:H). Finer textures of the textured reference and substrates ablated with

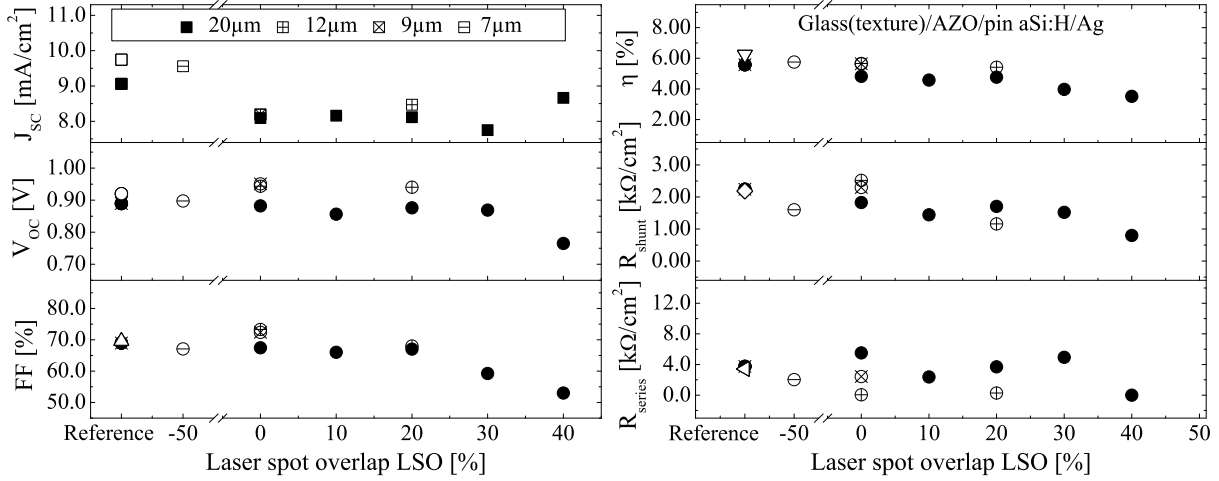


Figure 6.4: Electrical properties of pin aSi:H solar cells on substrates textured with varying laser spot diameters 20, 12, 9 and 7 μm and laser spot overlap (LSO)

narrower spot diameters might be more advantageous for growth.

Another possible explanation might be a reduced energy barrier at the AZO/p interface as a consequence of improved AZO quality. This might be particularly so for the periodically textured substrates, as they are assumed to have improved step coverage. Furthermore, Zinc oxide crystallizes in the wurtzite structure at ambient conditions and tetrahedral coordination of Zn and O atoms result in a polar symmetry along the hexagonal c-axis [195]. Several crystal characteristics and behaviour are a consequence of this polarity including crystal growth, etching, doping and defect generation [195]. Klein et al. report the work function is influenced by the crystallographic orientation [196]. This is an important parameter as it gives an indication of the energy required to extract the charge carriers and is relevant for the AZO/p interface in the solar cell and thus electrical performance.

Furthermore, the volume of the absorber material is expected to increase on textured substrates, particularly on randomly textured substrates showing folded structure. The deteriorated AZO film quality is assumed to be the main cause for the observed poor solar cell electrical properties on highly textured substrates.

6.3 nip aSi:H bifacial solar cells

Randomly textured substrates were suggested for substrate nip configuration and bifacial application mainly due to the opacity. The solar cells investigated had the configuration and film thickness glass(texture) AZO(1200nm), nip(300nm), AZO(200nm). This structure is by no means optimised for the application and merely aimed to demonstrate the potential serving as proof of concept.

Figure 6.5 shows the EQEs and reflection of the nip structure deposited on Type II textured with 7 μm laser spot diameter (ω_0) and at 355 mm/s (50% LSO) in bifacial

application. Measurements carried out were distinguished between the light entering the solar cell from the **front contact (FC)** and **back contact (BC)** AZO side. The former and latter shall also be noted as forward and reverse henceforth. The reference solar cell forward and reverse measurements showed interferences.

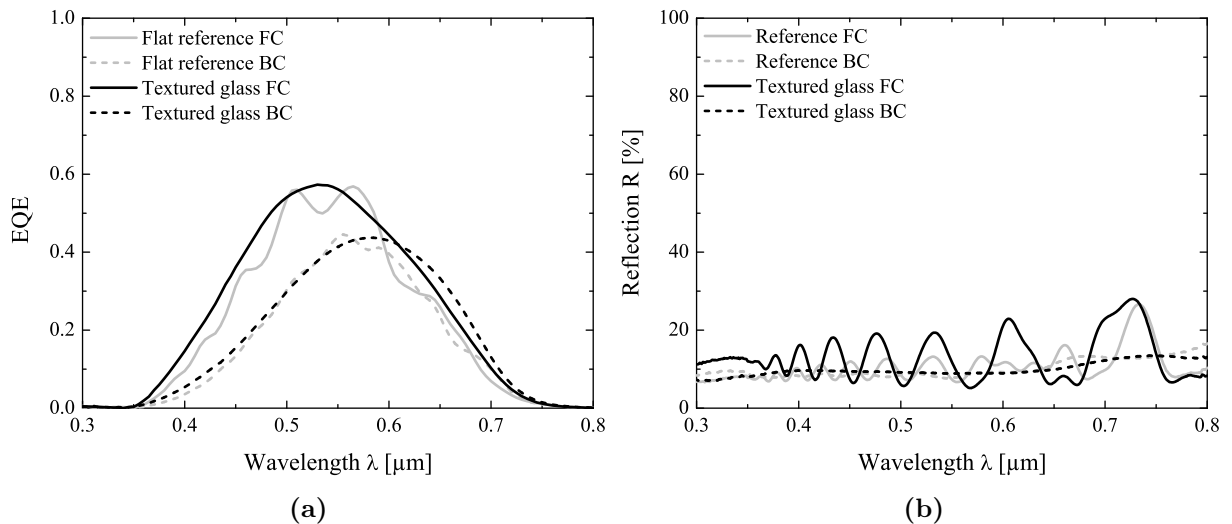


Figure 6.5: Bifacial aSi:H nip solar cells 6.5a EQE and 6.5b reflection measured on a flat reference (grey) in comparison to textured glass (black) scribed at 355 mm/s and 7 μm laser spot diameter with the light penetrating the solar cell from the front contact (solid) and back contact (dashed)

The reverse reflectivity (figure 6.5b) showed less interferences, and lower intensity. This is most likely due to the different AZO film thicknesses of the front (1200 nm) and back contact (200 nm). Forward EQE (figure 6.5a) was however higher than the reverse EQE. This can be attributed to the changed transparency and contributions of the parasitic absorption in the p, n-layers and AZO.

Figure 6.6 shows the electrical properties of the nip solar cells on substrates textured with different laser spot diameters and at a constant laser spot overlap of 50% to achieve a highly random texture. The filled symbols show values measured on a flat reference from co-deposition. Furthermore, the electrical properties of the solar cells deposited on glass substrates textured with $\omega_0 = 7 \mu\text{m}$ are shown for both forward and reverse structure.

The nip solar cells on textured glass substrates showed higher J_{SC} than the flat reference due to the improved light scattering properties. Contrary, V_{OC} , FF, R_{shunt} and consequently η deteriorated. R_{series} , on the other hand, remained similar and suggested that the AZO quality was similar. The reverse measurements showed a higher J_{SC} , most likely due to the reduced AZO (200 nm) parasitic absorption. The back contact AZO further showed a higher series resistance, which was also reflected in the higher R_{series} . V_{OC} and FF remained similar and η was slightly higher.

One main advantage of the application is the gain resulting from the summation of the forward and backward EQE. This proof of concept thus shows great potential for the

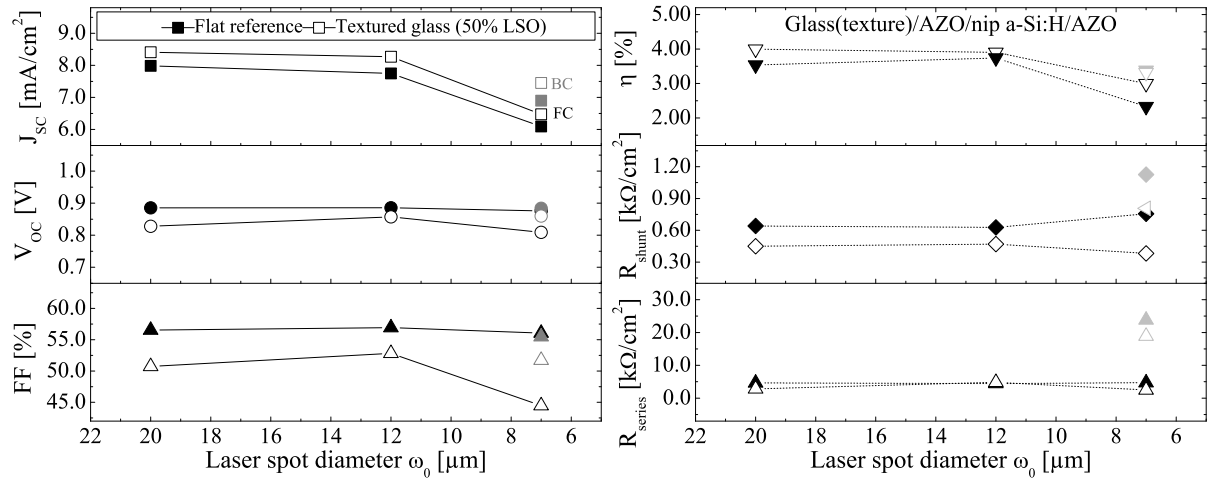


Figure 6.6: Electrical properties of aSi:H nip solar cells (glass/texture/AZO/nip/AZO) on substrates textured with different laser spot diameters 20, 12, 9 and 7 μm at 50 % laser spot overlap (LSO)

application of randomly textured glass substrates for nip and bifacial configuration. Once again, BC AZO is merely the same as the FC deposition parameters, only with a shorter deposition time.

This structure is by no means optimised for the application. Also the measuring was carried out under conditions used for nip and pin with highly reflecting back contacts. These aspects have to be kept in mind when assessing the results. Optimisation of FC and BC AZO deposition conditions are hence expected to enhance the performance.

6.4 pin aSi:H / μ cSi:H tandem solar cells

Another important aspect to be taken into consideration with textured glass substrates is their influence on the growth quality of the absorber layers. While this might not be as important for aSi:H because the material only has a short range, it is detrimental for μ cSi:H. To demonstrate this aspect, the morphology and crystallinity of μ cSi:H solar cells pin solar cells deposited on AZO coated laser-textured glass substrates were assessed and shown in figure 6.7.

SEM cross-section images of pin μ cSi:H are shown for glass substrates coated with 650 nm AZO. The glass were laser textured with a constant $\omega_0 = 20 \mu\text{m}$ and varying ν_{max} and 1000 mm/s (6.7a). The images additionally show sites with cracks to demonstrate their detrimental effect on AZO and subsequently μ cSi:H growth. The crystallinity of μ cSi:H deposited on the flat side of the textured substrates was slightly higher than the reference. This might be due to the reduced effective glass thickness following ablation and thus heat dissipation during PECVD. The crystallinity variation was however limited to $\pm 2.5 \%$. In contrast to this, crystallinity of μ cSi:H deposited on the textured surface decreased with increasing texture by more than 20%.

Folded structures (figure 6.7a) were also observed similar to aSi:H solar cell on ran-

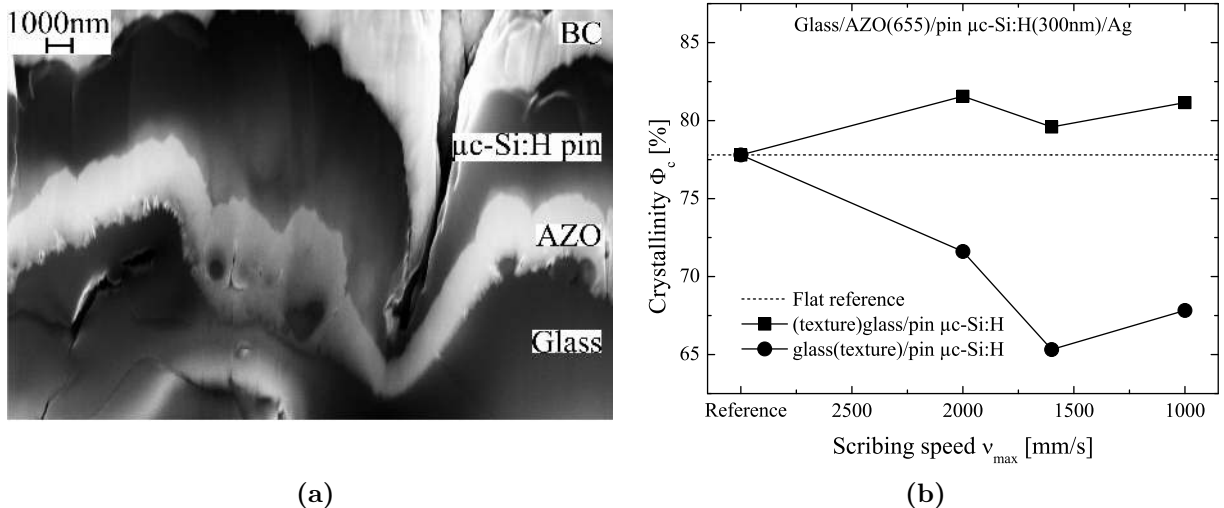


Figure 6.7: SEM cross-section images (6.7a) showing anisotropic growth of pin μ cSi:H on AZO coated highly textured Type II substrates. The image also shows sites of cracks in the glass substrates, which is detrimental for both AZO and μ cSi:H growth. The crystallinity of μ cSi:H (6.7b) on textured substrates

domly textured substrates (figure 6.1b). The significant difference was that the μ cSi:H wall coverage in the valleys was poor. This is detrimental for solar cell performance and could lead to a short circuit. An attempt to deposit thin single-junction μ cSi:H on such highly textured substrates lead to a majority of shunted solar cells.

Figure 6.8 shows the EQE and 1-R of the tandem solar cells consisting of glass (texture), AZO (1200 nm), pin aSi:H/ μ cSi:H (1050 nm), AZO (100 nm), Ag (300 nm) deposited on Type I laser textured with 20 μ m laser spot diameter at different scribing speeds. For a better comparison and quantification of the optical performance, a textured (TCO) reference is also shown. Textured reference showed increased solar cell absorption and a higher EQE throughout the spectrum. The interference fringes and solar cell absorption reduced and increased because of the increased light scattering on randomly textured AZO, respectively. Furthermore, reduced AZO thickness following the wet-chemical etching reduced the AZO parasitic absorption. Similarly, textured glass surfaces increased the solar cell absorption and EQE in comparison to the flat reference. Interference fringes were however still evident, indicating the light was diffused and absorbed effectively.

Figure 6.9 shows the results of the tandem solar cells deposited on Type I laser textured with 7 μ m laser spot diameter at different scribing speeds. The results show that decreasing ω_0 and ν_{max} further enhances the optical performance. This can be attributed to the decreased lateral dimension (D) of the texture with decreasing ω_0 and ν_{max} . Scatterers with lateral dimensions in the range of the wavelengths ($D \approx \lambda$) show a higher scattering efficiency in comparison to larger features ($D \gg \lambda$).

Furthermore, focusing of incident wavelengths by parabolic texture becomes more probable. Simulations of solar cell layers of periodically textured glass substrates with

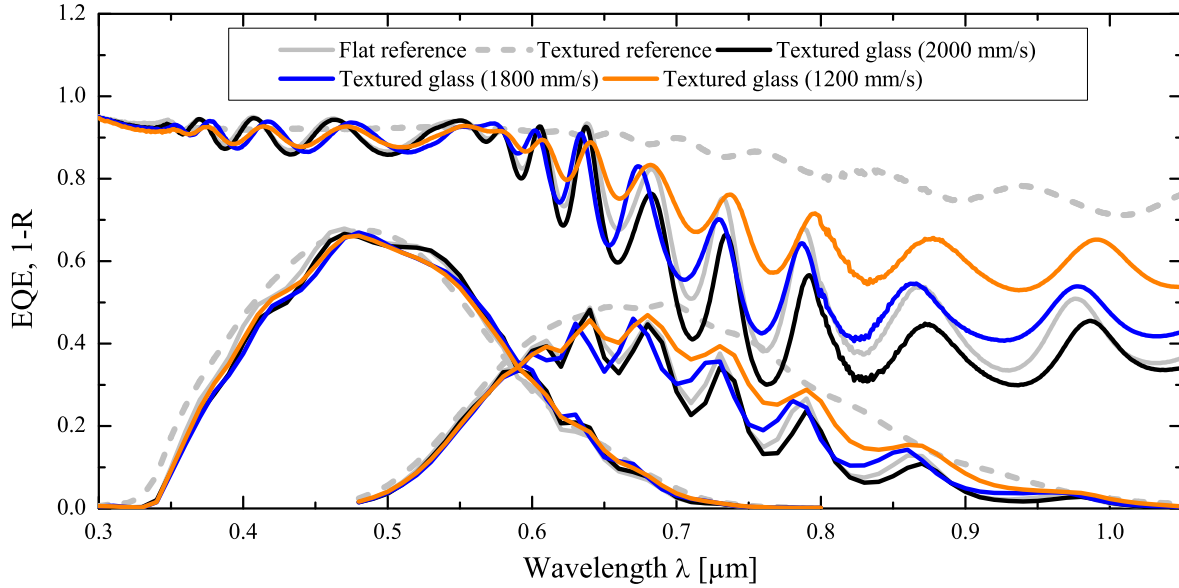


Figure 6.8: EQE and 1-R of tandem pin aSi:H/ μ Cs:H thin-film solar cells on Type I laser textured with 20 μ m laser spot diameter at different scribing speeds

Gaussian and rounded crater in the range of the wavelength ($D=1\mu\text{m}$) showed the focused optical generation rate in the absorber material enhanced the EQE [197]. This aspect was discussed in detail in the simulation Chapter (4), section (4.2). Experimental validation of the concept is shown for solar cells deposited on honey-comb AZO surface [44].

Another possible explanation is the increased surface area following ablation with reducing ν_{max} which leads to an increased effective absorber material covering the surface. The EQE of solar cells on textured glass substrates decreased in the UV region in comparison with the flat and textured reference. This might be due to higher AZO parasitic absorption, which increases with decreasing ω_0 and ν_{max} . Scattered light might effectively be coupled into the AZO layers and the substrate itself. Reducing AZO thickness and optimising deposition parameters can thus be expected to increase the EQE.

Figure 6.10 shows the electrical properties of the tandem solar cells as a function of the laser spot overlap (LSO). The filled symbols represent properties of solar cells on laser-textured substrates and open symbols on wet-chemically etched AZO. The textured reference showed higher J_{SC} and thus higher η in comparison to the flat reference due to the improved light scattering. Introducing a periodic texture on the glass surface improved the J_{SC} and was comparable to the textured reference. Apart from the light scattering, an increased surface area and thus absorber material might be one possible explanation for the improvement.

J_{SC} decreased with increasing texture, which might be due to reduced μ Cs:H crystallinity. V_{OC} and R_{series} did not show great variation and R_{shunt} slightly decreased on textured substrates in comparison to the flat reference. The efficiency η slightly increased with increasing glass texture. The optical and electrical performance of tandem solar

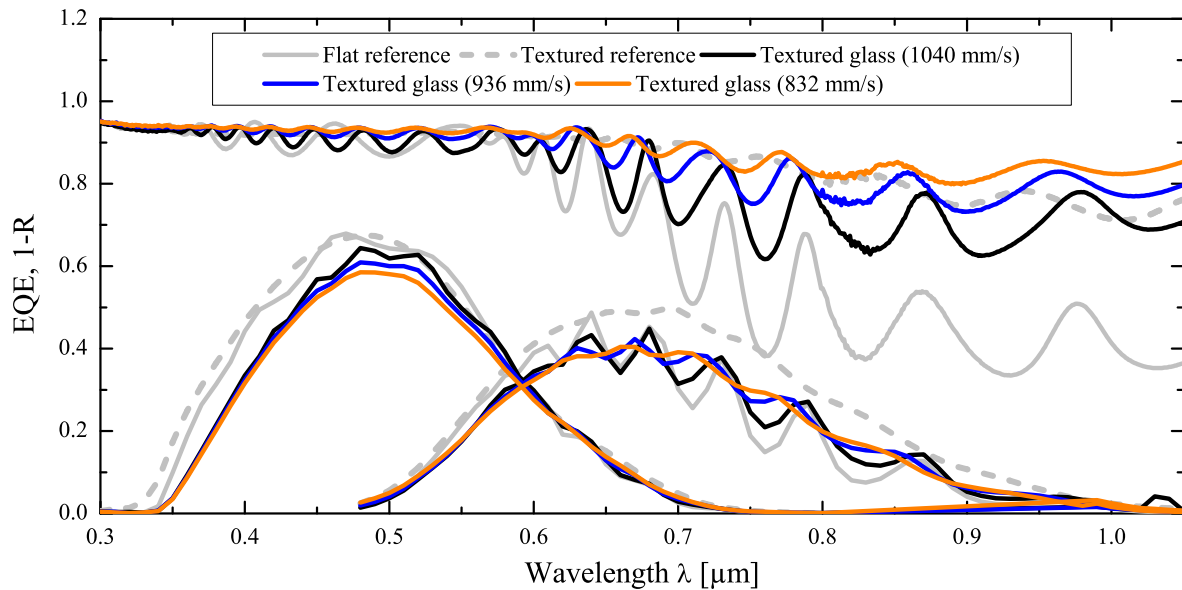


Figure 6.9: EQE and 1-R of tandem pin aSi:H/ μ cSi:H thin-film solar cells on Type I laser textured with 7 μ m laser spot diameter at different scribing speeds

cells on laser-textured substrates were comparable to textured reference. These are significant results because the investigated solar cells had a thick 1200 nm AZO film, which was not optimized for deposition on textured glass substrates. Reduction in AZO film thickness and optimisation of the deposition conditions are thus expected to enhance the performance multi-fold.

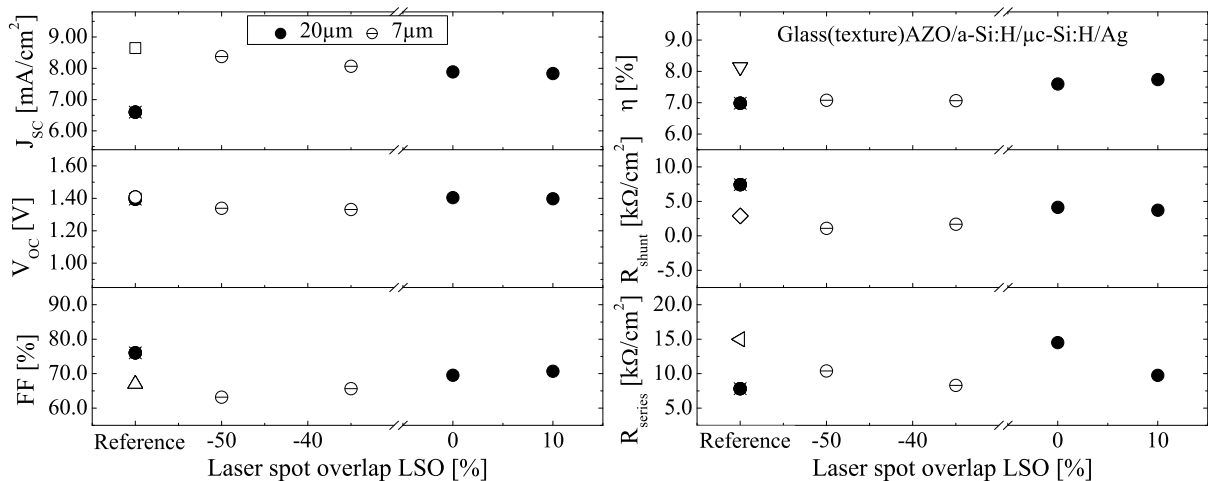


Figure 6.10: Electrical properties of tandem pin aSi:H/ μ cSi:H thin-film solar cells as a function laser spot overlap

In summary, it can be stated that improvement in the optical properties of the solar cell were observed with increasing texture due to reduced reflection and interference fringes. Deterioration in the electrical properties was moderate. Randomly textured substrates ablated with smaller ω_0 showed most improvement, due to the finer texture. It was shown that the low transparency could be compensated by using nip configuration and

particularly for bifacial application. The gain resulting from summation of the EQE from the front and back contact was shown. The highest obtained efficiencies for the different solar cells are listed in table 6.1.

Solar Cell	Texture Glass	η %	V_{OC} mV	J_{SC} mA/cm ²	FF %
pin aSi:H	7 μ m(1040mm/s)	5.80	898	9.56	67
pin aSi:H/ μ cSi:H	7 μ m(1040mm/s)	7.10	1339	8.37	63
nip aSi:H	12 μ m(600mm/s)	3.70	858	8.27	53
nip aSi:H bi-facial FC	7 μ m(355mm/s)	2.30	809	6.48	45
nip aSi:H bi-facial BC	7 μ m(355mm/s)	3.30	860	7.45	52

Table 6.1: Electrical properties of silicon thin-film solar cells on ps laser-textured glass. Values are the highest efficiencies of the solar cells from the first functioning run i.e. unoptimised

The reported values are from the first run with functioning solar cells. The deposition parameters are not optimised for both AZO and solar cells. The performance of solar cells on textured glass and wet-chemically textured reference were comparable. The most important comparison is with optimized solar cells from literature. The efficiencies reported in this study are comparable to literature given in table 2.2. These are significant results because optimizing deposition conditions for textured substrates is expected to enhance the solar cell performance. Experimental optimisation of AZO and silicon thin-film solar cell depositions are out of scope for the investigation. Improvement in solar cell performance by reducing AZO thickness is assessed by numerical modelling in the following Chapter 7.

7 Optimisation of TCO in pin aSi:H

The experimental results indicated that the laser-textured substrates show great potential to compete with the conventional state-of-the-art textured electrodes. Numerical modelling were carried out to demonstrate the optimisation potential for reducing the front contact TCO thickness. The change in the optical losses of the solar cells deposited on the textured glass and front contact are compared.

7.1 Numerical Modelling

7.1.1 Simulation domain

The software Sentaurus TCAD developed by Synopsis was used for 3D finite-difference-time-domain (FDTD) method numerical modelling [132] with the approach validated by Lacombe et al. [133]. Figure 7.1 shows the simulation domains of the layer stacks investigated in this study. Figure (7.1b) shows a 3D superstrate pin solar cell consisting of glass (texture), TCO (960-10 nm), p-aSi:H (10 nm), i-aSi:H (420 nm), n-aSi:H (25 nm), Ag (300 nm). Optical constants of the films determined from experiment [134] and Ag from literature [198] were used as input parameters. 2D cross section of the angular intensity distribution (AID) simulation domain with the layer stack glass/TCO/ambient or i-aSi:H is shown in (7.1c). Simulations in ambient air were comparable to the experiment. The texture was transferred to the glass surface as demonstrated in figure 7.1c (bottom) and the thickness was adjusted to 300 nm to accommodate the roughness height.

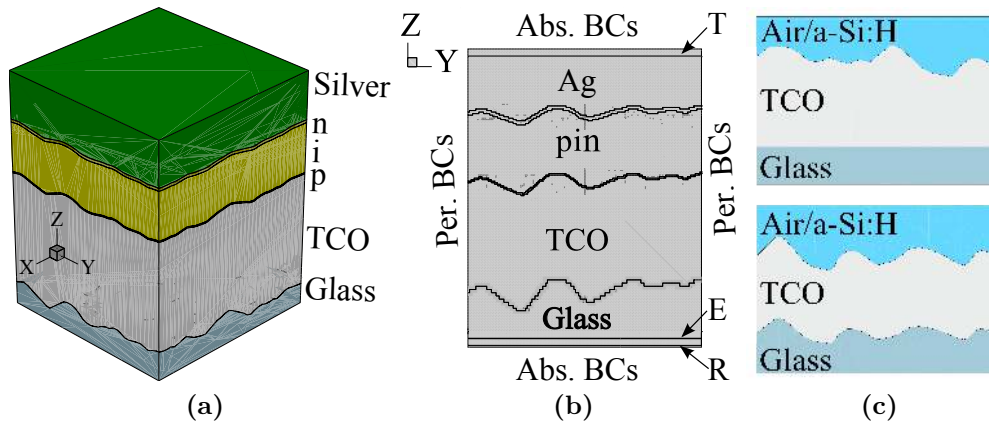


Figure 7.1: Simulation domain of (7.1a) 3D superstrate solar cell showing layer stack, (7.1b) 2D cross-section showing planes and boundary conditions and (7.1c) angular intensity distribution (AID) with textured TCO (top) and glass (bottom) either in ambient or intrinsic silicon aSi:H

Planes were inserted as demonstrated in the 2D cross section in figure 7.1b to detect

the transmitted (T) and reflected (R) amplitude. The excitation plane was placed within the glass substrate to deliver an electromagnetic field (E) source. The absorption in the glass was therefore neglected, and a constant 4% reflection was assumed for the air/glass interface. Periodic (per.) boundary conditions (BCs) were assumed for the vertical sides of the structure and absorbing (abs.) for the horizontal. Coherent, monochromatic harmonic, plane electromagnetic wave with a wavelength λ was applied at normal incidence. The AM1.5G spectrum was used for EQEs and R respectively kept constant at 1000 W/m² for the AID simulations.

7.1.2 Simulated output

Conversion efficiency of the solar cells of $\eta = 1$ was used and electrical losses were not taken into consideration. The photocurrent J_{ph} generated in the respective material was calculated from the simulated optical generation rate G_{opt} by

$$J_{ph}(\lambda) = \frac{q}{A} \int_V G_{opt}(x, y, z, \lambda) dV \quad (7.1)$$

where q is the elementary charge and A the base area of the simulation domain. External quantum efficiency was deduced by

$$EQE = \frac{I_{abs}}{I_i} = \frac{J_{ph} h \cdot c}{I_i q \cdot \lambda} \quad (7.2)$$

where I_{abs} is the absorbed intensity and I_i is the incident intensity.

Apart from the optical generation rate, the stationary electric field and intensity distribution are plotted at the transmission and reflection plane. The electric field amplitude plotted at the transmission plane contains near-field E^n scattering information. To be able to compare the simulated scattering results to the experimentally obtained angular resolved measurements taken at a sample-detector distance of $d=92$ mm (Chapter 3, section 3.3), the far-field (E^f) scattering information is required. Near-to-far-field (NTFF) Fourier transformation (FT) was carried as detailed by Lacombe et al. [128, 133] to obtain the ADI.

7.1.3 Simulation variables

Realistic texture shown in figure 7.2 of commercially available ASAHI U fluorine doped tin oxide SnO₂:F deposited by atmospheric pressure chemical vapour deposition (APCVD) with optimized random pyramidal texture was used. The topology was digitized from experimentally obtained AFM measurements on an area of 10 $\mu\text{m} \times 10 \mu\text{m}$. In contrast to Lacombe et al., the imported surface height profile data points were reduced from 256 \times 256 to 128 \times 128 in the x- and y-direction (figure 7.2). This had the advantage that the structure formation process in the simulation was faster. Simulation results are

nevertheless justified, as they were only compared with each other.

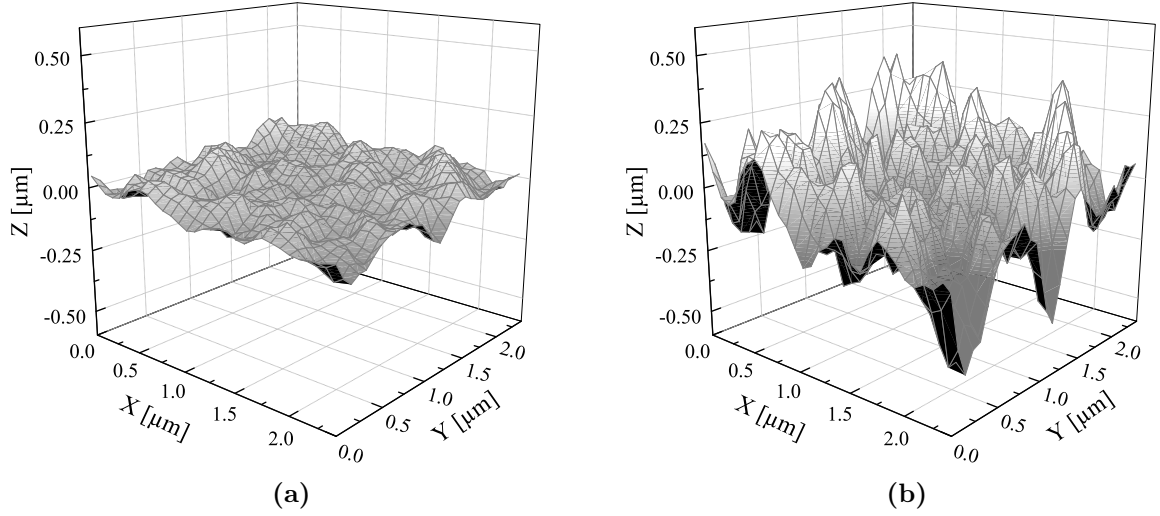


Figure 7.2: Surface topology imported from AFM measurements with figure 7.2a resolution of 128×128 points and figure 7.2b increased texture height

The topology of the imported texture was then varied by changing the aspect ratio. Figure 7.2a shows a section of the reference texture with a roughness $\sigma_{rms}=40$ nm, averaged height $h_1=125$ nm and lateral dimension $D \approx 200$ nm. Increasing the texture height by a factor for example 3.5 in figure 7.2b changed the surface properties to $h_3=440$ nm and $\sigma_{rms}=144$ nm. Further manipulation included increasing the period (not shown).

The following layers were added with slight rounding of the interface. This aimed to achieve a realistic stack observed in experiment and other studies [35–37] as discussed in Chapter 2, Section 2.2. TCO thickness was gradually decreased from 960 nm to 10 nm. For ADI modelling, ambient air was replaced with 300 nm intrinsic amorphous i-aSi:H to give a realistic distribution within the solar cell. Thick i-layer was used to ensure complete absorption of low penetration depth wavelengths. This allows a better assessment of the long wavelengths AID where light scattering is required and investigation of the reflection at the glass/TCO/aSi:H interfaces in the solar cell.

7.2 Results and Discussion

Optical performance of differently textured substrates was assessed by comparing the intrinsic absorber external quantum efficiency (EQE_i) with the solar cell absorption. The latter is approximated by $1-R$ assuming no transmission occurs. Furthermore, the weighted averaged reflection R_w given by

$$R_w = \frac{\int_{\lambda_1}^{\lambda_2} R(\lambda)\phi(\lambda)S(\lambda)d\lambda}{\int_{\lambda_1}^{\lambda_2} \phi(\lambda)S(\lambda) d\lambda} \quad (7.3)$$

was determined for the region $\lambda_1=320$ nm and $\lambda_2=810$ nm using the AM1.5G spectrum, where $\phi(\lambda)$ is the irradiance and $S(\lambda)$ the internal spectral sensitivity of the solar cell.

R_w and J_{ph} are readily used as parameters to assess the effectiveness of antireflection coating [199]. For a better comparison, the percentage increase in J_{ph} in the absorber layers on textured substrates with respect to the flat reference was calculated by

$$\frac{\Delta J_{ph}}{J_{ph}} = \frac{J_{ph}(textured) - J_{ph}(reference)}{J_{ph}(reference)} \quad (7.4)$$

In principle J_{ph} can be approximated to be the short-circuit current density (J_{sc}), since the solar cell is assumed to be ideal without any electrical losses in the intrinsic layer and contribution from the doped layers.

7.2.1 Textured glass substrate

The effect of transferring the texture from the TCO to the glass surface is demonstrated in figure 7.3. No significant deviations were observed in the EQE_i for $\lambda < 600$ nm following the translation because the wavelengths have a low penetration depth. Results however suggested interference fringes and reflection particularly in the near infrared (NIR) region $\lambda > 600$ nm were enhanced. Decreased TCO showed reduced parasitic absorption and reflection in the region $\lambda < 600$ nm. Solar cell absorption increased throughout the spectrum. All in all, these observations suggested that different effects occurred in spectral regions (I) higher and (II) lower than 600 nm.

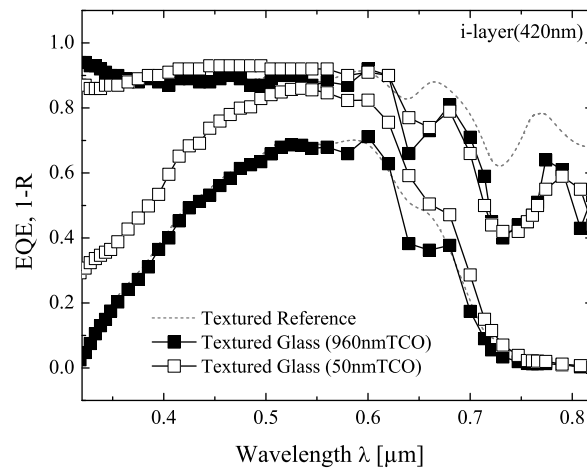


Figure 7.3: Absorption of the solar cells (1-R) and intrinsic absorber layers EQE_i on textured glass substrates with different TCO thickness in comparison to the textured reference

Spectral region (I) Reflection reduction is dominated by antireflection behaviour of the front electrode [16, 26, 39, 45, 55, 194, 199]. This aspect is readily used in thin-film solar cells on textured TCO to implement a refractive index grading at the TCO/i-aSi:H interface. This interface has been identified to deliver the most potential for reflection reduction, due to the high refractive index transition and thus high reflection losses around $>10\%$ [194]. On the other hand, glass/TCO interface is not as crucial, as the reflection is merely around 2%. It is therefore reasonable to assume that the observed antireflection behaviour in this study is to a great extent a consequence of the reduced reflection at the former interface. Antireflection can result from different effects.

On the one hand, the TCO thickness (d_{TCO}) behaves as a single quarter-wavelength antireflection coating for $d_{TCO} = \lambda/4 \cdot n_{TCO}$ provided that $n_{TCO} = \sqrt{n_{glass}n_{aSi:H}}$, where n_{TCO} , n_{glass} , $n_{aSi:H}$ are the refractive indices of TCO, glass and aSi:H, respectively [26, 39, 55, 199]. AR effect can thus be expected to be more profound in the blue and visible region of the spectrum $\lambda < 600$ nm and explain the observed shift to shorter wavelengths with decreasing TCO thickness.

On the other hand, the topology at the interfaces induces an antireflection behaviour [16, 36, 40, 45, 194, 200–202] particularly for wavelengths higher than the lateral dimension D of the texture [36]. The mechanism behind this effect is the formation of an effective medium resulting from the corrugated surface [202]. The refractive index transition is thus graded at the interface and reduces the reflection losses.

Figure 7.4 demonstrates the influence of the antireflection behaviour on J_{ph} for TCO thicknesses < 200 nm. Reflectivity of the solar cells on textured substrates was reduced and the J_{ph} increased compared to the flat reference. Highest gain was observed for the 50 nm TCO thickness with the lowest reflectivity. Further reduction in the electrode thickness did not enhance light in-coupling, but rather promoted reflection in this region.

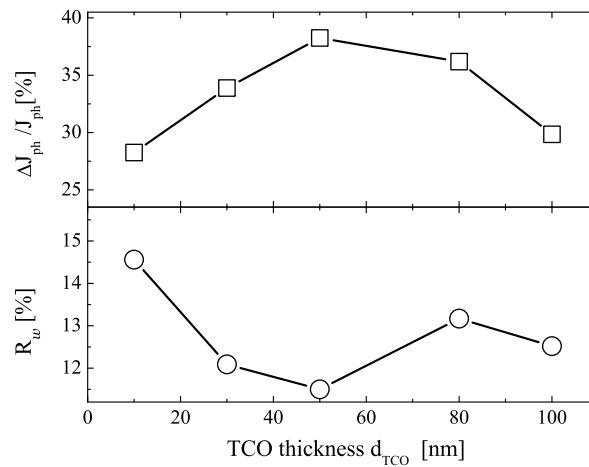


Figure 7.4: Simulated improvement in the photocurrent density J_{ph} and average weighed reflectivity R_w of solar cells on textured glass with 420 nm intrinsic absorber and thin TCO ≤ 100 nm.

Spectral region (II) Apart from the refractive index grading, the texture at the surface randomises the light, preferentially into greater angles to increase the optical path and thus the probability of the light being reflected back at the following interfaces. In spite of the transferred texture, prominent Fabry-Perot interferences were nevertheless observed for $\lambda > 600$ nm.

Similar behaviour was observed in experiment of pin aSi:H Chapter 6, section 6.2 and attributed to the TCO thickness. Isabella et al. observe the effect in pin aSi:H on periodically textured glass substrates [46]. Neubert et al. observe a similar behaviour in micromorph solar cells on textured glass, but with larger craters dimensions (700 nm) [15]. They attribute the interference fringes to the absence of small-scaled roughness features to achieve sufficient scattering [15]. In this simulation study, an optimized random pyramidal texture with various feature scales ($D \approx 200$ nm and $\sigma_{rms} = 40$ nm) was used and interference fringes were nevertheless observed. Intensity of the interference fringes decreased with the TCO thickness.

Another interesting observation in the high wavelength region was the overall reduced solar cell absorption. Reflection was significantly high in comparison to the textured reference. This behaviour was observed in all solar cells on textured glass substrates irrespective of the TCO and i-aSi:H thickness. This was a rather unexpected result, since the parasitic absorption of the silver (Ag) back contact was expected to increase when a texture is introduced at the aSi:H/Ag interface [200, 203, 204]. Highly absorbing metal back contact is normally detrimental to light in-coupling in the NIR region. Increased NIR solar cell reflection however suggests that the aSi:H/Ag parasitic absorption is mitigated.

Changed geometry at the aSi:H/Ag interface was assumed to be partly responsible for this observation. The topology of this interface in the different solar cells was analysed. In particular, optical generation rates G_{opt} in figure 7.5 at the wavelength 640 nm, where prominent interference fringes were observed were studied. The colour bar in the images is set to the maximum intensity of $1.28 \times 10^{-3} \text{ s}^{-1}$, which is observed in the flat reference (not shown) to allow a better comparison of the distribution. High G_{opt} at the aSi:H/Ag interface for all substrates confirmed the studied wavelength reached the back contact. The penetration depth of the $\lambda = 640$ nm was estimated to be $6.37 \mu\text{m}$ and $0.69 \mu\text{m}$ in TCO and i-aSi:H respectively. Consequently, the light was reflected back into the solar cell and standing waves occurred in the thick TCO due to insufficient scattering.

Transferring the texture to the glass surface reduced and broadened the texture height and period at the TCO/aSi:H and aSi:H/Ag interfaces compared to the textured reference, respectively. Reducing the TCO thickness transferred a more defined texture, with an increased height. This was suggested to increase the averaged Ag absorption from 1.18% to 3.06% and minimally influence R_w . However, the results however showed a significant reduction in the TCO parasitic absorption from 31.76% to 7.60%. Increased substrate transparency was made a major contribution to i-aSi:H absorption and J_{ph} enhancement.

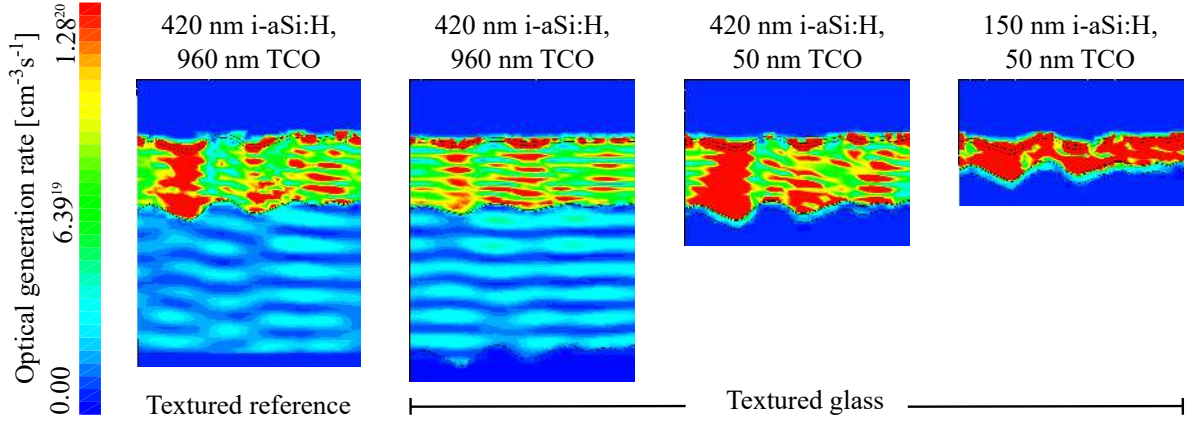


Figure 7.5: Optical generation rate G_{opt} profile at 640 nm wavelength of solar cells on textured substrates with varying TCO and i-aSi:H thickness

Although thick absorber layers provide useful information, it is necessary to investigate state-of-the-art absorber thickness. I-layer thickness was thus reduced to 150 nm, which led to a more evenly distributed G_{opt} profile and reduced J_{ph} . Reduced J_{ph} showed the texture was not optimized for thin absorber layers. Measures of improving light management were thus required.

7.2.2 Light scattering

Studies have demonstrated that an increased light scattering into higher angles correlates linearly with the generated photocurrent in tandem solar cells [68]. While our investigations were carried out for single junction solar cells, these are readily used in multi-junction solar cells. Information of the scattering behaviour is therefore a useful tool in optimizing the light management. Contribution of light scattering to i-aSi:H absorption enhancement was investigated by comparing the AID of the differently textured substrates.

Figure 7.6 shows the AIDs simulated for the wavelength 650 nm. The results comparable to experiment (ambient air) suggested the intensity scattered into lower angles was more affected than in higher angles when the texture was transferred to the glass surface. Changes were attributed to altered angle of incidence and exit at the TCO/air interface [65] compared to the textured reference. Decreasing the TCO thickness reduced the scattered intensity particularly into greater angles. Increased specular peaks (area under $0-5^\circ$) indicate the transmission is increased [205]. This is generally observed for longer wavelengths as λ becomes larger than the scattering texture dimension D [38].

To give a realistic scattering profile within the solar cell, ambient air was replaced with i-aSi:H. The specular portion was reduced due to i-aSi:H absorption and the intensity in all the angles was enhanced. Yablonoitch [39] deduced an intensity enhancement factor of $2n^2$, where n is the refractive index of the material where light propagates. Furthermore, intensity of the scattered light is proportional to $1/\lambda^4$ according to Rayleigh and thus increases with ν^4 [128]. Effective wavelength within a given material with a refractive

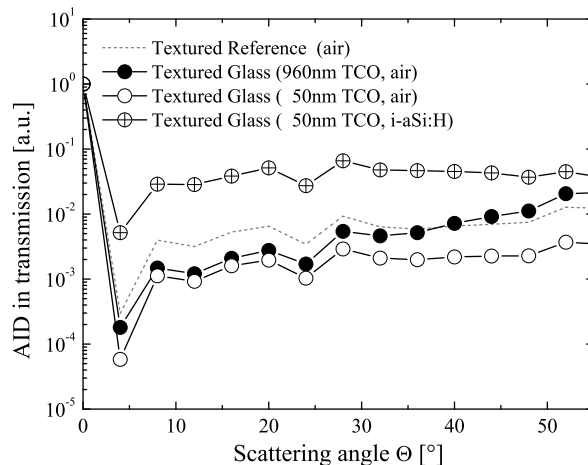


Figure 7.6: Simulated AID at 650 nm wavelength (I) comparing the textured reference with textured glass in ambient air and (II) textured glass coated with 50 nm TCO in air and aSi:H ambient

index n_{mat} however varies and changes the relation to the lateral dimension D . Transferring the texture to the glass surface increases D on the TCO surface and thus the scattering cross-section, particularly in NIR. Topology on the substrate must thus be modified to obtain a favourable texture on the TCO/i-aSi and Si/Ag interfaces.

7.2.3 Modified glass texture

Influence of modifying the glass topology was investigated on state-of-the-art ultra-thin solar cell performance. First, films were added on the textured carrier substrate with slight rounding on subsequent interfaces (h_1). The rounding was then reduced to achieve more defined edges (h_2). Finally, the texture height was increased by a factor of 1.5, 2.5 and 3.5, and thus the aspect ratio. For a better overview, only the results of 3.5 (h_3) are illustrated and discussed. (The textures h_1 and h_3 are shown in figure 7.2b).

Figure 7.7 demonstrates the performance of solar cells on the latter textures. The results demonstrated $\lambda < 500$ nm were effectively absorbed as they have a low penetration depth < 150 nm in the investigated material. Reduced reflection, as a consequence of the antireflective behaviour, was also evident in the thin solar cells. Fabry-Perot interference fringes were however observed to shift to shorter wavelengths, due to the reduced absorber material. A profound interference fringe was thus observed around 550 nm and NIR reflection was much higher than in thicker absorber layers. Increased profile height increased 1-R due to increased averaged TCO and Ag absorption. Increased EQE_i was nevertheless observed which might partly be due to enhanced antireflection behaviour. Another possible explanation is the increased surface area of the texture covered with the thin absorber layer. Increased absorber volume increases J_{ph} .

To sum up it can be stated summarise, the potential of application of state-of-the-art ultra-thin electrodes in silicon thin-film solar cells on realistic textured substrates

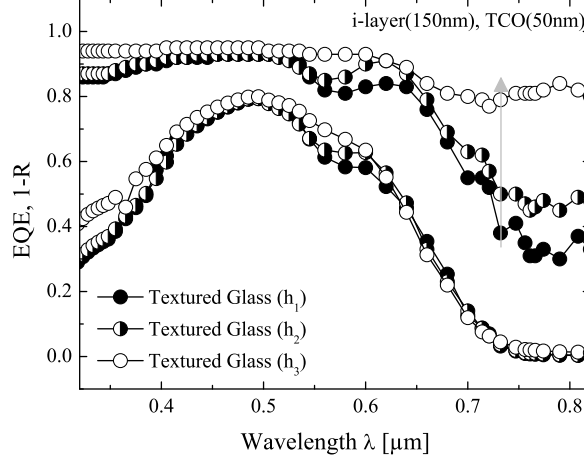


Figure 7.7: Total solar cell absorption and ultra-thin 150 nm intrinsic absorber EQE_i on differently textured glass substrates with 50 nm TCO

was numerically modelled. The results are summarized in table 7.1. The topology of effectively textured TCO was translated to the glass surface. The results showed that NIR parasitic absorption in the metal back contact was reduced compared to the textured reference because of the rounded aSi:H/Ag interface. Changed light scattered showed minor contribution to J_{ph} . Instead, reduced TCO thickness showed a significant influence by increasing the front contact transparency and thus absorption in the i-aSi:H layer. Additionally, an antireflection behaviour of the ultra-thin TCOs was observed for $\lambda < 600$ nm resulting from a graded refractive index at the textured interface and single coating quarter-wavelength.

Sample	d(i-aSi:H) nm	d(TCO) nm	Abs(TCO) nm	Abs(Ag) nm	R_w %	J_{ph} mA/cm ²	$\Delta J_{ph} / J_{ph}$ %
Flat Ref.	420	960	30.16	1.18	15.50	10.70	
Txt. Ref.	420	960	31.55	5.06	7.78	11.80	11.10
Txt. Glass	420	960	31.76	3.06	11.30	11.20	4.90
Txt. Glass	420	50	7.60	5.66	11.50	14.70	38.40
Flat Ref.	150	50	4.64	1.38	21.50	10.00	
Txt. Glass (h_1)	150	50	7.56	5.35	13.50	11.90	19.00
Txt. Glass (h_2)	150	50	7.74	6.78	11.01	12.10	20.80
Txt. Glass (h_3)	150	50	9.22	10.38	5.24	12.50	24.80

Table 7.1: Average weighed reflectivity R_w and the generated photocurrent J_{ph} of solar cells with the corresponding parasitic absorption in the TCO and Ag layers

Defined texture edges and increased texture height increased the antireflection behaviour. Simultaneously, parasitic TCO and Ag absorptions increased. Absorption in the i-aSi:H layer on highly textured nevertheless increased, most likely due to increased surface area and thus absorber material volume. state-of-the-art ultra-thin solar cells with 50 nm TCO and 150 nm i-aSi:H on such highly textured substrates demonstrate superior performance with the highest J_{ph} (12.5 mA/cm²) in comparison to both the flat

and textured reference.

8 Summary and Outlook

Direct picosecond laser ablation was investigated as an alternative to chemical texturing glass substrates for the application in thin-film solar cells. Commercially available aluminoborosilicate with alkali (Type I), earth alkali (Type II) and soda-lime (Type III) glass substrates were textured with varying scribing speed and pulse energy. The findings can be summarised as follows:

- The reference glass composition influences the dimensions of the ablated crater. The degree of texturing was changed from periodic to random by decreasing the scribing speed and pulse energy.
- Highly textured substrates showed broadband light scattering into greater angles in the UV and NIR region. Such textures showed potential to address insufficient NIR scattering of ion beam etched glass substrates with topologies comparable to sputtered and post wet-chemical etched AZO.
- Numerical modelling showed that the refractive index change in Type II highly textured substrates was higher in comparison to the periodically textured samples. Great refractive index ($\Delta n > 0.05$) change on the glass surface increased the reflection in solar cells layer stack. Decreased refractive index showed a higher impact than an increased refractive index.
- Raman analysis of the molecular vibration modes suggested that increased three- and four-fold rings small-fold boroxol rings or alternatively Si-O-Si linkages in Type II were responsible for the reduced refractive index.
- Annealing the textured substrates reduced the structural changes in highly textured substrates. This is an advantage, since the subsequent AZO pre-deposition heating step can also be used to alleviate the laser induced stress and structural modification. It is also possible that both higher temperatures and longer annealing times might further enhance the effect. Further investigations should be directed at analysing whether observed modification before and after annealing are permanent.
- The electrical properties of AZO deposited on periodically and randomly textured substrates improved and deteriorated in comparison to the reference, respectively.
- The surface morphology of glass surface was changed and indicated by increasing phase shift with texture. Increased phase shift is attributed to increasing stiffness of the material, which show a lower thermal expansion coefficient. This is an important

parameter for lattice mismatch and the results suggest highly textured substrates might be highly mismatched. This might be a possible explanation for the high strain and poor electrical properties in AZO. Another major contributor to the AZO properties is suggested to be the improved uniformity of the periodically textured substrates in comparison to the highly textured substrates.

- Performance of unoptimised solar cells on laser-textured glass (table 6.1) were comparable to optimized solar cells from literature (table 2.2). These are significant results because optimizing deposition conditions for textured substrates is expected to enhance the solar cell performance significantly.
- Simulations results showed that the optimal TCO thickness was 50 nm. An antireflection behaviour was observed for $\lambda < 600$ nm resulting from a graded refractive index at the textured interface and single coating quarter-wavelength. State-of-the-art ultra-thin solar cells with 50 nm TCO and 150 nm i-aSi:H on such highly textured substrates demonstrate superior performance with the highest J_{ph} (12.5 mA/cm²) in comparison to both the flat and textured reference (table 7.1).

Future research should be dedicated to identifying the elements in the heat-affected zone of the glass substrates following ablation. This can for example be achieved by X-ray photoelectron (XPS). Moreover, experiments should be dedicated to optimising AZO on textured glass surface to obtain ultra-thin films. The investigations should be directed towards temperature, power and oxygen partial pressure variation [206]. Transparency and conductivity of the films can be optimised by adjusting the oxygen pressure in the deposition process. Oxygen vacancies in AZO lattice act as donors [207] and a high oxygen content leads to Al₂O₃ formation resulting in films with high transparency and low conductivity [208]. Low-oxygen films show the opposite behaviour due to the high free carrier absorption [206–208].

Pin solar cells showed good results, but further reproducibility investigations are required. This applies to all investigated solar cells. Nip solar cells structure must additionally be reconsidered. The used structure consisted of transparent AZO as front and back contact. State-of-the-art nip solar cells used reflecting back contacts. Use of white paint on the highly textured substrates could for example be investigated. Alternatively, laser perforated ultra-thin metal films [209] could be an interesting choice for the back contact to be investigated. For the μ cSi:H solar cells, crystallites must be adjusted for the differently textured substrates.

References

- [1] United Nations (UN). (2013) World population prospects: The 2012 revision volume II: Demographic profiles. Accessed 2015.05.08. [Online]. Available: <http://esa.un.org/unpd/wpp/index.htm>
- [2] United States Energy Information Administration (EIA). (2013) International energy outlook 2013. Accessed 2015.05.08. [Online]. Available: <http://www.eia.gov/forecasts/ieo/>
- [3] ispy publishing. (2013) PV and solar market intelligence report 2013. Accessed 31.03.2014. [Online]. Available: <http://pipelineme.com/media/797151/PV-and-Solar-Market-Intelligence-Report.pdf>
- [4] M. A. Green, K. Emery, Y. Hishikawa, W. Warta, and E. D. Dunlop, “Solar cell efficiency tables (version 44),” *Progress in Photovoltaics: Research and Applications*, vol. 22, no. 7, pp. 701–710, 2014. [Online]. Available: <http://dx.doi.org/10.1002/pip.2525>
- [5] ISE. (2014) Fraunhofer Institut für solare energiesysteme (ise) photovoltaics report 2014. Accessed 2015.05.08. [Online]. Available: <http://www.ise.fraunhofer.de/en/renewable-energy-data/data-and-facts-about-pv>
- [6] Z. Wu, Y. Zhang, K. Ma, Y. Cao, H. Lin, Y. Jia, J. Chen, and H. Li², “Strong visible-light photovoltaic effect in multiferroic $\text{pb}(\text{fe}_{1/2}\text{v}_{1/2})\text{o}_3$ bulk ceramics,” *Physica Status Solidi (RRL)-Rapid Research Letters*, vol. 8, no. 1, pp. 36–39, 2014. [Online]. Available: <http://dx.doi.org/10.1002/pssr.201308259>
- [7] F. Hao, C. C. Stoumpos, D. H. Cao, R. P. H. Chang, and M. G. Kanatzidis, “Lead-free solid-state organic-inorganic halide perovskite solar cells,” *Nature Photonics*, vol. 8, no. 6, pp. 489–494, 2014. [Online]. Available: <http://dx.doi.org/10.1038/nphoton.2014.82>
- [8] J. D. Major, R. E. Treharne, L. J. Phillips, and K. Durose, “A low-cost non-toxic post-growth activation step for CdTe solar cells,” *Nature*, vol. 511, pp. 334–337, 2014. [Online]. Available: <http://dx.doi.org/10.1038/nature13435>
- [9] A. Shah, J. Meier, A. Buechel, U. Kroll, J. Steinhauser, F. Meillaud, H. Schade, and D. Dominé, “Towards very low-cost mass production of thin-film silicon photovoltaic (PV) solar modules on glass,” *Thin Solid Films*, vol. 502, no. 1-2, pp. 292–299, 2006. [Online]. Available: <http://dx.doi.org/10.1016/j.tsf.2005.07.299>

- [10] S. Benagli, D. Borrello, E. Vallat, J. Meier, U. Kroll, J. Hötzel, J. Bailat, J. Steinhauser, M. Marmelo, G. Monteduro, and L. Castens, “High-efficiency amorphous silicon devices on LPCVD-ZnO TCO prepared in industrial KAI TM-M R&D reactor,” in *PVSEC*, no. 24, Hamburg, Germany, 2009, pp. 2293–2298. [Online]. Available: <http://dx.doi.org/10.4229/24thEUPVSEC2009-3BO.9.3>
- [11] H. Sai, K. Saito, N. Hozuki, and M. Kondo, “Relationship between the cell thickness and the optimum period of textured back reflectors in thin-film microcrystalline silicon solar cells,” *Applied Physics Letters*, vol. 102, no. 5, p. 053509, 2013. [Online]. Available: <http://dx.doi.org/10.1063/1.4790642>
- [12] J. Müller, B. Rech, J. Springer, and M. Vaněček, “TCO and light trapping in silicon thin film solar cells,” *Solar Energy*, vol. 77, no. 6, pp. 917–930, 2004. [Online]. Available: <http://dx.doi.org/10.1016/j.solener.2004.03.015>
- [13] A. Kołodziej, “Staebler-Wronski effect in amorphous silicon and its alloys,” *Opto-electronics Review*, vol. 12, no. 1, pp. 21–32, 2004. [Online]. Available: <http://www.wat.edu.pl/review/optor/12%281%2921.pdf>
- [14] M. Kambe, T. Matsui, H. Sai, N. Taneda, K. Masumo, A. Takahashi, T. Ikeda, T. Oyama, M. Kondo, and K. Sato, “Improved light-trapping effect in a-Si:H/ μ c-Si:H tandem solar cells by using high haze SnO₂:F thin films,” in *IEEE PVSC*, vol. 2, no. 34, June 2009, pp. 001 663–001 666. [Online]. Available: <http://dx.doi.org/10.1109/pvsc.2009.5411411>
- [15] S. Neubert, S. Ring, F. Welker, S. Götzenndörfer, F. Ruske, B. Stannowski, R. Schlatmann, and B. Rech, “Very thin, highly-conductive ZnO:Al front electrode on textured glass as substrate for thin-film silicon solar cells,” *Physica Status Solidi (RRL)-Rapid Research Letters*, vol. 8, no. 1, pp. 44–47, 2014. [Online]. Available: <http://dx.doi.org/10.1002/pssr.201308195>
- [16] M. Zeman, O. Isabella, K. Jäger, R. Santbergen, S. Solntsev, M. Topič, and J. Krč, “Advanced light management approaches for thin-film silicon solar cells,” *Energy Procedia*, vol. 15, no. 0, pp. 189–199, 2012, international Conference on Materials for Advanced Technologies 2011, Symposium O. [Online]. Available: <http://dx.doi.org/10.1016/j.egypro.2012.02.022>
- [17] M. Boccard, C. Battaglia, S. Hänni, K. Söderström, J. Escarré, S. Nicolay, F. Meillaud, M. Despeisse, and C. Ballif, “Multiscale transparent electrode architecture for efficient light management and carrier collection in solar cells,” *Nano Letters*, vol. 12, no. 3, pp. 1344–1348, 2012. [Online]. Available: <http://dx.doi.org/10.1021/nl203909u>

- [18] N. Sahraei, S. Venkataraj, P. Vayalakkara, and A. G. Aberle, “Optical absorption enhancement in amorphous silicon films and solar cell precursors using the aluminum-induced glass texturing method,” *International Journal of Photoenergy*, vol. 2014, p. 6, 2014. [Online]. Available: <http://dx.doi.org/10.1155/2014/842891>
- [19] G. Jo, M. Choe, S. Lee, W. Park, Y. H. Kahng, and T. Lee, “The application of graphene as electrodes in electrical and optical devices,” *Nanotechnology*, vol. 23, no. 11, p. 112001, 2012. [Online]. Available: <http://stacks.iop.org/0957-4484/23/i=11/a=112001>
- [20] A. Hongsingthong, A. Aino, P. Sichanugrist, M. Konagai, H. Kuramochi, R. Akiike, H. Iigusa, K. Utsumi, and T. Shibusami, “Development of novel Al-doped zinc oxide films fabricated on etched glass and their application to solar cells,” *Japanese Journal of Applied Physics*, vol. 51, no. 10S, p. 10NB09, 2012. [Online]. Available: <http://dx.doi.org/10.1143/JJAP.51.10NB09>
- [21] Q. Zhou, W. Yang, F. He, R. Stoian, R. Hui, and G. Cheng, “Femtosecond multi-beam interference lithography based on dynamic wavefront engineering,” *Optics Express*, vol. 21, no. 8, pp. 9851–9861, 2013. [Online]. Available: <http://dx.doi.org/10.1364/OE.21.009851>
- [22] A. Arriola, A. Rodriguez, N. Perez, T. Tavera, M. J. Withford, A. Fuerbach, and S. M. Olaizola, “Fabrication of high quality sub-micron Au gratings over large areas with pulsed laser interference lithography for SPR sensors,” *Optical Materials Express*, vol. 2, no. 11, pp. 1571–1579, 2012. [Online]. Available: <http://dx.doi.org/10.1364/ome.2.001571>
- [23] X. Zhao and Y. C. Shin, “Femtosecond laser drilling of high-aspect ratio microchannels in glass,” *Applied Physics A*, vol. 104, no. 2, pp. 713–719, 2011. [Online]. Available: <http://dx.doi.org/10.1007/s00339-011-6326-z>
- [24] D. Moore, M. Rahman, D. Dowling, P. McNally, and D. Brabazon, “Laser machined macro and micro structures on glass for enhanced light trapping in solar cells,” *Applied Physics A*, vol. 110, no. 3, pp. 661–665, 2013, *Appl. Phys. A*. [Online]. Available: <http://dx.doi.org/10.1007/s00339-012-7147-4>
- [25] M. Kauf, R. Patel, and J. Bovatsek, “High speed processing for microelectronics and photovoltaics,” *Laser Technik Journal*, vol. 6, no. 1, pp. 33–37, 2009. [Online]. Available: <http://dx.doi.org/10.1002/latj.200990006>
- [26] T. Söderström, “Single and multi-junction thin film silicon solar cells for flexible photovoltaics,” Ph.D. dissertation, Universite de Neuchatel, 2009. [Online]. Available: <http://infoscience.epfl.ch/record/135702>

- [27] T. Razykov, C. Ferekides, D. Morel, E. Stefanakos, H. Ullal, and H. Upadhyaya, “Solar photovoltaic electricity: Current status and future prospects,” *Solar Energy*, vol. 85, no. 8, pp. 1580–1608, 2011, progress in Solar Energy 1. [Online]. Available: <http://dx.doi.org/10.1016/j.solener.2010.12.002>
- [28] J. Meier, S. Dubail, R. Platz, P. Torres, U. Kroll, J. A. Selvan, N. P. Vaucher, C. Hof, D. Fischer, H. Keppner, R. Flückiger, A. Shah, V. Shklover, and K.-D. Ufert, “Towards high-efficiency thin-film silicon solar cells with the “micromorph” concept,” *Solar Energy Materials and Solar Cells*, vol. 49, pp. 35–44, 1997. [Online]. Available: [http://dx.doi.org/10.1016/S0927-0248\(97\)00173-6](http://dx.doi.org/10.1016/S0927-0248(97)00173-6)
- [29] T. C. M. Müller, E. Moulin, and U. Aeberhard, “Improvement of hydrogenated microcrystalline (*μc*-si:h) single junction solar cells with upconverter at rear side.” *Energy Procedia*, vol. 10, no. 0, pp. 76–82, 2011, european Materials Research Society ConferenceSymp. Advanced Inorganic Materials and Concepts for Photovoltaics. [Online]. Available: <http://dx.doi.org/10.1016/j.egypro.2011.10.156>
- [30] P. Würfel, *Physics of Solar Cells: From Principles to New Concepts*. Wiley-VCH Verlag GmbH, 2007, ch. Basic Structure of Solar Cells, pp. 109–136. [Online]. Available: <http://dx.doi.org/10.1002/9783527618545.ch6>
- [31] J. Löffler, “Transparent conductive oxides for thin-film silicon solar cells,” Ph.D. dissertation, University of Utrecht, 2004. [Online]. Available: <http://dspace.library.uu.nl/handle/1874/2165>
- [32] M. Berginski, J. Hüpkes, M. Schulte, G. Schöpe, H. Stiebig, B. Rech, and M. Wuttig, “The effect of front ZnO:Al surface texture and optical transparency on efficient light trapping in silicon thin-film solar cells,” *Journal of Applied Physics*, vol. 101, no. 7, p. 074903, 2007. [Online]. Available: <http://dx.doi.org/10.1063/1.2715554>
- [33] J. Hüpkes, J. Owen, E. Bunte, H. Zhu, S. Pust, J. Worbs, and G. Jost, “New texture etching of zinc oxide: Tunable light trapping for si thin film solar cells,” in *PVSEC*, no. 25, Valencia, Spain, 2010, pp. 3224–3227. [Online]. Available: <http://dx.doi.org/10.4229/25thEUPVSEC2010-3AV.2.25>
- [34] J. I. Owen, J. Hüpkes, H. Zhu, E. Bunte, and S. E. Pust, “Novel etch process to tune crater size on magnetron sputtered ZnO:Al,” *Physica Status Solidi (A)*, vol. 208, no. 1, pp. 109–113, 2011. [Online]. Available: <http://dx.doi.org/10.1002/pssa.201026164>
- [35] S. Geißendörfer, M. Vehse, T. Voss, J.-P. Richters, B. Hanke, K. von Maydell, and C. Agert, “Integration of n-doped ZnO nanorod structures as novel light-trapping concept in amorphous thin film silicon solar cells,” *Solar Energy*

- Materials and Solar Cells*, vol. 111, no. 0, pp. 153–159, 2013. [Online]. Available: <http://dx.doi.org/10.1016/j.solmat.2012.12.042>
- [36] O. Isabella, A. Campa, M. Heijna, W. Soppe, R. van Erven, R. Franken, H. Borg, and M. Zeman, “Diffraction gratings for light trapping in thin-film silicon solar cells,” in *PVSEC*, vol. 2, no. 23, May 2008, pp. 1527–1532 Vol.2. [Online]. Available: <http://dx.doi.org/10.4229/23rdEUPVSEC2008-3AV.1.48>
- [37] V. Jovanov, X. Xu, S. Shrestha, M. Schulte, J. Hüpkes, and D. Knipp, “Predicting the interface morphologies of silicon films on arbitrary substrates: Application in solar cells,” *ACS Applied Materials & Interfaces*, vol. 5, no. 15, pp. 7109–7116, 2013. [Online]. Available: <http://dx.doi.org/10.1021/am401434y>
- [38] T. Rother, *Electromagnetic Wave Scattering on Nonspherical Particles*, ser. Springer Series in Optical Sciences. Springer Berlin Heidelberg, vol. 145. [Online]. Available: http://dx.doi.org/10.1007/978-3-642-00704-0_1
- [39] E. Yablonovitch, “Statistical ray optics,” *Journal of the Optical Society of America*, vol. 72, no. 7, pp. 899–907, Jul 1982. [Online]. Available: <http://dx.doi.org/10.1364/JOSA.72.000899>
- [40] O. Deparis, J. P. Vigneron, O. Agustsson, and D. Decroupet, “Optimization of photonics for corrugated thin-film solar cells,” *Journal of Applied Physics*, vol. 106, 2009. [Online]. Available: <http://dx.doi.org/10.1063/1.3253755>
- [41] P. Bühlmann, J. Bailat, D. Dominé, A. Billet, F. Meillaud, A. Feltrin, and C. Ballif, “In situ silicon oxide based intermediate reflector for thin-film silicon micromorph solar cells,” *Applied Physics Letters*, vol. 91, no. 14, p. 143505, 2007. [Online]. Available: <http://dx.doi.org/10.1063/1.2794423>
- [42] D. Dominé, P. Buehlmann, J. Bailat, A. Billet, A. Feltrin, and C. Ballif, “Optical management in high-efficiency thin-film silicon micromorph solar cells with a silicon oxide based intermediate reflector,” *Physica Status Solidi (RRL)-Rapid Research Letters*, vol. 2, no. 4, pp. 163–165, 2008. [Online]. Available: <http://dx.doi.org/10.1002/pssr.200802118>
- [43] K. Söderström, F.-J. Haug, J. Escarré, O. Cubero, and C. Ballif, “Photocurrent increase in n-i-p thin film silicon solar cells by guided mode excitation via grating coupler,” *Applied Physics Letters*, vol. 96, no. 21, p. 213508, 2010. [Online]. Available: <http://dx.doi.org/10.1063/1.3435481>
- [44] R.-E. Nowak, S. Geißendörfer, K. Chakanga, M. Juilfs, N. Reininghaus, M. Vehse, K. von Maydell, and C. Agert, “Optimizing folded silicon

- thin-film solar cells on ZnO honeycomb electrodes,” *IEEE Journal of Photovoltaics*, vol. 5, no. 2, pp. 479–486, March 2015. [Online]. Available: <http://dx.doi.org/10.1109/JPHOTOV.2014.2388079>
- [45] B. Lipovšek, M. Cvek, Čampa A., J. Krč, and M. Topič, “Analysis and optimisation of periodic interface textures in thin-film silicon solar cells,” in *PVSEC*, no. 25, Valencia, Spain, September 2010, pp. 3120–3123. [Online]. Available: <http://dx.doi.org/10.4229/25thEUPVSEC2010-3AV.1.81>
- [46] O. Isabella, S. Solntsev, D. Caratelli, and M. Zeman, “3-D optical modeling of thin-film silicon solar cells on diffraction gratings,” *Progress in Photovoltaics: Research and Applications*, vol. 21, no. 1, pp. 94–108, 2013. [Online]. Available: <http://dx.doi.org/10.1002/pip.1257>
- [47] A. Naqavi, K. Söderström, F.-J. Haug, V. Paeder, T. Scharf, H. P. Herzig, and C. Ballif, “Understanding of photocurrent enhancement in real thin film solar cells: towards optimal one-dimensional gratings,” *Optics Express*, vol. 19, no. 1, pp. 128–140, Jan 2011. [Online]. Available: <http://dx.doi.org/10.1364/OE.19.000128>
- [48] N. Sahraei, S. Venkataraj, A. G. Aberle, and M. Peters, “Optimum feature size of randomly textured glass substrates for maximum scattering inside thin-film silicon solar cells,” in *Proc. SPIE*, vol. 8981, 2014, pp. 89 811D–89 811D–8. [Online]. Available: <http://dx.doi.org/10.1117/12.2036349>
- [49] P. I. Widenborg and A. G. Aberle, “Polycrystalline silicon thin-film solar cells on AIT-textured glass superstrates,” *Advances in OptoElectronics*, vol. 2007, 2007. [Online]. Available: <http://dx.doi.org/10.1155/2007/24584>
- [50] H. Taniguchi, H. Sannomiya, K. Kajiwara, K. Nomoto, Y. Yamamoto, K. Hiyoshi, H. Kumada, M. Murakami, and T. Tomita, “Amorphous silicon solar cell on textured tempered glass substrate prepared by sandblast process,” *Solar Energy Materials and Solar Cells*, vol. 49, pp. 101–106, 1997. [Online]. Available: [http://dx.doi.org/10.1016/S0927-0248\(97\)00182-7](http://dx.doi.org/10.1016/S0927-0248(97)00182-7)
- [51] W. Zhang, U. W. Paetzold, M. Meier, A. Gordijn, J. Hüpkes, and T. Merdzhanova, “Thin-film silicon solar cells on dry etched textured glass,” *Energy Procedia*, vol. 44, no. 0, pp. 151–159, 2014, proceedings of E-MRS Spring Meeting 2013 Symposium D Advanced Inorganic Materials and Structures for Photovoltaics 27-31 May 2013, Strasbourg, France. [Online]. Available: <http://dx.doi.org/10.1016/j.egypro.2013.12.022>
- [52] W. Zhang, E. Bunte, J. Worbs, H. Siekmann, J. Kirchhoff, A. Gordijn, and J. Hüpkes, “Rough glass by 3d texture transfer for silicon thin film solar cells,”

- Physica Status Solidi (C)*, vol. 7, no. 3-4, pp. 1120–1123, 2010. [Online]. Available: <http://dx.doi.org/10.1002/pssc.200982773>
- [53] M. A. Munshi and H. Weman, “Advances in semiconductor nanowire growth on graphene,” *Physica Status Solidi (RRL)-Rapid Research Letters*, vol. 7, no. 10, pp. 713–726, 2013. [Online]. Available: <http://dx.doi.org/10.1002/pssr.201308010>
- [54] M. A. Gluba, D. Amkreutz, G. V. Troppenz, J. Rappich, and N. H. Nickel, “Embedded graphene for large-area silicon-based devices,” *Applied Physics Letters*, vol. 103, no. 7, p. 073102, 2013. [Online]. Available: <http://dx.doi.org/10.1063/1.4818461>
- [55] Y. Zhao, F. Chen, Q. Shen, and L. Zhang, “Light-trapping design of graphene transparent electrodes for efficient thin-film silicon solar cells,” *Applied Optics*, vol. 51, no. 25, pp. 6245–6251, 2012. [Online]. Available: <http://dx.doi.org/10.1364/AO.51.006245>
- [56] V. R. Bhardwaj, E. Simova, P. B. Corkum, D. M. Rayner, C. Hnatovsky, R. S. Taylor, B. Schreder, M. Kluge, and J. Zimmer, “Femtosecond laser-induced refractive index modification in multicomponent glasses,” *Journal of Applied Physics*, vol. 97, no. 8, p. 083102, 2005. [Online]. Available: <http://dx.doi.org/10.1063/1.1876578>
- [57] N. Reininghaus, M. Kellermann, K. von Maydell, and C. Agert, “Effects of process parameters on $\mu\text{c-Si:H}_1 - x\text{Ge}_x\text{:H}$ solar cells performance and material properties,” *EPJ Photovoltaics*, vol. 6, p. 65301, 2015. [Online]. Available: <http://dx.doi.org/10.1051/epjpv/2015002>
- [58] G. Bugnon, G. Parascandolo, S. Hänni, M. Stuckelberger, M. Charrière, M. Despeisse, F. Meillaud, and C. Ballif, “Silicon oxide buffer layer at the p-i interface in amorphous and microcrystalline silicon solar cells,” *Solar Energy Materials and Solar Cells*, vol. 120, Part A, pp. 143 – 150, 2014. [Online]. Available: <http://www.sciencedirect.com/science/article/pii/S092702481300442X>
- [59] G. Binnig, C. F. Quate, and C. Gerber, “Atomic force microscope,” *Physical Review Letters*, vol. 56, pp. 930–933, 1986. [Online]. Available: <http://dx.doi.org/10.1103/PhysRevLett.56.930>
- [60] J. Patterson and B. Bailey, *Solid-State Physics*. Springer Berlin Heidelberg, 2010. [Online]. Available: <http://dx.doi.org/10.1007/978-3-642-02589-10>
- [61] D. Bosbach, A. Putnis, U. Bismayer, and B. Güttler, “An AFM study on ferroelastic domains in lead phosphate $\text{Pb}_3(\text{PO}_4)_2$,” *Journal of Physics:*

- Condensed Matter*, vol. 9, no. 40, p. 8397, 1997. [Online]. Available: <http://dx.doi.org/10.1088/0953-8984/9/40/007>
- [62] Nanosurf, *Operating Instructions, Mobile S, Version 2.0*, 2009.
- [63] B. Bhushan, *Surface Roughness Analysis and Measurement Techniques*. CRC Press, 2000. [Online]. Available: <http://dx.doi.org/10.1201/9780849377877.ch2>
- [64] D. Nečas and P. Klapetek, “Gwyddion: an open-source software for SPM data analysis,” *Central European Journal of Physics*, vol. 10, pp. 181–188, 2012. [Online]. Available: <http://dx.doi.org/10.2478/s11534-011-0096-2>
- [65] M. Schulte, “Streuverhalten von texturierten TCO-Substraten in Silizium-Dünnschichtsolarzellen,” Ph.D. dissertation, RWTH Aachen, Paderborn, 2009. [Online]. Available: http://publications.rwth-aachen.de/record/51110/files/Schulte_Melanie.pdf
- [66] P. van Nijnatten, “An automated directional reflectance/transmittance analyser for coating analysis,” *Thin Solid Films*, vol. 442, no. 1, pp. 74–79, 2003, selected papers from the 4th International Conference on Coatings on Glass. [Online]. Available: [http://dx.doi.org/10.1016/S0040-6090\(03\)00947-7](http://dx.doi.org/10.1016/S0040-6090(03)00947-7)
- [67] K. Jäger, O. Isabella, R. A. C. M. M. van Swaaij, and M. Zeman, “Angular resolved scattering measurements of nano-textured substrates in a broad wavelength range,” *Measurement Science and Technology*, vol. 22, no. 10, p. 105601, 2011. [Online]. Available: <http://dx.doi.org/10.1088/0957-0233/22/10/105601>
- [68] W. Dewald, “Lichtmanagement in silizium-Dünnschichtsolarzellen,” Ph.D. dissertation, Justus-Liebig-Universität Gießen, 2013. [Online]. Available: <http://geb.uni-giessen.de/geb/volltexte/2013/9584/>
- [69] H. Fujiwara, *Spectroscopic Ellipsometry*. John Wiley & Sons, Ltd, 2007. [Online]. Available: <http://dx.doi.org/10.1002/9780470060193>
- [70] R. E. Nowak, “Investigation of opto-electronical properties of DC magnetron sputtered ZnO:Al films with respect to the layer thickness, annealing temperature and resistance inhomogeneity,” Master’s thesis, Carl-von-Ossietzky University Oldenburg, 2011. [Online]. Available: <http://oops.uni-oldenburg.de/id/eprint/1218>
- [71] G. Choong, E. Vallat-Sauvain, X. Multone, L. Fesquet, U. Kroll, and J. Meier, “Measurements of Raman crystallinity profiles in thin-film microcrystalline silicon solar cells,” *Journal of Physics D: Applied Physics*, vol. 46, no. 23, p. 235105, 2013. [Online]. Available: <http://stacks.iop.org/0022-3727/46/i=23/a=235105>

- [72] O. Madani Ghahfarokhi, K. von Maydell, and C. Agert, “Enhanced passivation at amorphous/crystalline silicon interface and suppressed Schottky barrier by deposition of microcrystalline silicon emitter layer in silicon heterojunction solar cells,” *Applied Physics Letters*, vol. 104, no. 11, p. 113901, 2014. [Online]. Available: <http://scitation.aip.org/content/aip/journal/apl/104/11/10.1063/1.4868726>
- [73] P. Larkin, *Chapter 2-Basic Principles*, P. Larkin, Ed. Oxford: Elsevier, 2011. [Online]. Available: <http://dx.doi.org/10.1016/B978-0-12-386984-5.10002-3>
- [74] W. Demtröder, *Experimentalphysik 3*, ser. Springer-Lehrbuch. Springer Berlin Heidelberg, 2010. [Online]. Available: <http://dx.doi.org/10.1007/978-3-642-03911-9>
- [75] S. Fuhrmann, “Druckabhängigkeit der topologischen Heterogenität von Gläsern,” Ph.D. dissertation, Friedrich-Alexander-Universität Erlangen-Nürnberg, 2013. [Online]. Available: <https://opus4.kobv.de/opus4-fau/frontdoor/index/index/docId/3629>
- [76] G. D’Angelo, G. Carini, C. Crupi, M. Koza, G. Tripodo, and C. Vasi, “Boson peak in alkaline borate glasses: Raman spectroscopy, neutron scattering, and specific-heat measurements,” *Physical Review B*, vol. 79, p. 014206, Jan 2009. [Online]. Available: <http://link.aps.org/doi/10.1103/PhysRevB.79.014206>
- [77] R. Shuker and R. W. Gammon, “Raman-scattering selection-rule breaking and the density of states in amorphous materials,” *Physical Review Letters*, vol. 25, pp. 222–225, Jul 1970. [Online]. Available: <http://link.aps.org/doi/10.1103/PhysRevLett.25.222>
- [78] F. L. Galeener and P. N. Sen, “Theory for the first-order vibrational spectra of disordered solids,” *Physical Review B*, vol. 17, pp. 1928–1933, Feb 1978. [Online]. Available: <http://link.aps.org/doi/10.1103/PhysRevB.17.1928>
- [79] F. Holtz, J.-M. Béný, B. O. Mysen, and M. Pichavant, “High-temperature Raman spectroscopy of silicate and aluminosilicate hydrous glasses: Implications for water speciation,” *Chemical Geology*, vol. 128, no. 1, pp. 25–39, 1996. [Online]. Available: [http://dx.doi.org/10.1016/0009-2541\(95\)00161-1](http://dx.doi.org/10.1016/0009-2541(95)00161-1)
- [80] S. Yannopoulos, K. Andrikopoulos, and G. Ruocco, “On the analysis of the vibrational boson peak and low-energy excitations in glasses,” *Journal of Non-Crystalline Solids*, vol. 352, no. 42, pp. 4541–4551, 2006. [Online]. Available: <http://dx.doi.org/10.1016/j.jnoncrysol.2006.02.164>
- [81] B. Cochain, D. Neuville, G. Henderson, O. Pinet, and P. Richet, “Determination of iron redox ratio in borosilicate glasses and melts from Raman spectra,” in *proc.*

- ATALANTE*, vol. 4, Montpellier, France, 2008, pp. 11–17. [Online]. Available: www.iaea.org/inis/collection/NCLCollectionStore/_Public/40/034/40034702.pdf
- [82] A. D. Muro, N. Métrich, M. Mercier, D. Giordano, D. Massare, and G. Montagnac, “Micro-Raman determination of iron redox state in dry natural glasses: Application to peralkaline rhyolites and basalts,” *Chemical Geology*, vol. 259, no. 1, pp. 78–88, 2009, experimental techniques for the study of hydrothermal fluids and silicate melts. [Online]. Available: <http://dx.doi.org/10.1016/j.chemgeo.2008.08.013>
- [83] P. Ricciardi, “Raman spectroscopy for the non destructive characterization of ancient pottery, porcelain and mosaic glass,” Ph.D. dissertation, Università degli studi di Firenze, 2008.
- [84] M. Wojdyr, “Fityk: a general-purpose peak fitting program,” *Journal of Applied Crystallography*, vol. 43, no. 5-1, pp. 1126–1128, 2010. [Online]. Available: <http://dx.doi.org/10.1107/S0021889810030499>
- [85] Y. Waseda, E. Matsubara, and K. Shinoda, *X-Ray Diffraction Crystallography*. Springer Berlin Heidelberg, 2011. [Online]. Available: <http://dx.doi.org/10.1007/978-3-642-16635-8>
- [86] J. G. Lu, Z. Z. Ye, Y. J. Zeng, L. P. Zhu, L. Wang, J. Yuan, B. H. Zhao, and Q. L. Liang, “Structural, optical, and electrical properties of (zn,al)o films over a wide range of compositions,” *Journal of Applied Physics*, vol. 100, no. 7, p. 073714, 2006. [Online]. Available: <http://dx.doi.org/10.1063/1.2357638>
- [87] A. K. Zak, W. A. Majid, M. Abrishami, and R. Yousefi, “X-ray analysis of ZnO nanoparticles by Williamson–Hall and size–strain plot methods,” *Solid State Sciences*, vol. 13, no. 1, pp. 251–256, 2011. [Online]. Available: <http://dx.doi.org/10.1016/j.solidstatesciences.2010.11.024>
- [88] T. Ungár, “Characterization of nanocrystalline materials by x-ray line profile analysis,” *Journal of Materials Science*, vol. 42, no. 5, pp. 1584–1593, 2007. [Online]. Available: <http://dx.doi.org/10.1007/s10853-006-0696-1>
- [89] S. Rahmane, M. Djouadi, M. Aida, N. Barreau, B. Abdallah, and N. H. Zoubir, “Power and pressure effects upon magnetron sputtered aluminum doped ZnO films properties,” *Thin Solid Films*, vol. 519, no. 1, pp. 5–10, 2010. [Online]. Available: <http://dx.doi.org/10.1016/j.tsf.2010.06.063>
- [90] S. Singh, T. Ganguli, R. Kumar, R. Srinivasa, and S. Major, “Substrate temperature dependence of growth mode, microstructure and optical properties of highly oriented zinc oxide films deposited by reactive sputtering,” *Thin Solid Films*, vol. 517, no. 2, pp. 661–669, 2008. [Online]. Available: <http://dx.doi.org/10.1016/j.tsf.2008.07.040>

- [91] C. Charpentier, P. Prod'homme, I. Maurin, M. Chaigneau, and P. Roca i Cabarrocas, "X-ray diffraction and Raman spectroscopy for a better understanding of ZnO:Al growth process," *EPJ Photovoltaics*, vol. 2, p. 25002, 2011. [Online]. Available: <http://dx.doi.org/10.1051/epjpv/2011026>
- [92] V. Mote, Y. Purushotham, and B. Dole, "Williamson-Hall analysis in estimation of lattice strain in nanometer-sized ZnO particles," *Journal of Theoretical and Applied Physics*, no. 6, 2012. [Online]. Available: <http://dx.doi.org/10.1186/2251-7235-6-6>
- [93] M. Jaboyedoff, B. Kubler, and P. Thelin, "An empirical scherrer equation for weakly swelling mixed-layer minerals, especially illite-smectite," *Clay Minerals*, vol. 34, no. 4, pp. 601–617, 1999. [Online]. Available: <http://claymin.geoscienceworld.org/content/34/4/601.abstract>
- [94] D. Rusu, G. Rusu, and D. Luca, "Structural characteristics and optical properties of thermally oxidized zinc films," *Acta Physica Polonica A*, vol. 119, no. 6, 2011. [Online]. Available: <http://info.ifpan.edu.pl/APP/>
- [95] A. Alkahlout, N. Al Dahoudi, I. Grobelsek, M. Jilavi, and P. de Oliveira, "Synthesis and characterization of aluminum doped zinc oxide nanostructures via hydrothermal route," *Journal of Materials*, vol. 2014, p. 235638, 2014. [Online]. Available: <http://dx.doi.org/10.1155/2014/235638>
- [96] R. Cebulla, R. Wendt, and K. Ellmer, "Al-doped zinc oxide films deposited by simultaneous rf and dc excitation of a magnetron plasma: Relationships between plasma parameters and structural and electrical film properties," *Journal of Applied Physics*, vol. 83, no. 2, pp. 1087–1095, 1998. [Online]. Available: <http://dx.doi.org/10.1063/1.366798>
- [97] Z. Yun, W. Yue, W. Peng-Fei, L. Hong-Yu, and W. Shou-Yu, "Optical and mechanical properties of transparent conductive al-doped ZnO films deposited by the sputtering method," *Chinese Physics Letters*, vol. 29, no. 3, p. 038103, 2012. [Online]. Available: <http://stacks.iop.org/0256-307X/29/i=3/a=038103>
- [98] Y. Guo, "Raman spectroscopy of glasses with high and broad Raman gain in the boson peak region," Ph.D. dissertation, University of Central Florida, 2006. [Online]. Available: <http://purl.fcla.edu/fcla/etd/CFE0001322>
- [99] W. H. Zachariasen, "The atomic arrangement in glass," *Journal of the American Chemical Society*, vol. 54, no. 10, pp. 3841–3851, 1932. [Online]. Available: <http://dx.doi.org/10.1021/ja01349a006>

- [100] S. Kojima and M. Kodama, “Boson peak of lithium and cesium borate glass studied by Raman scattering,” *IOP Conference Series: Materials Science and Engineering*, vol. 18, no. 11, p. 112004, 2011. [Online]. Available: <http://dx.doi.org/10.1088/1757-899X/18/11/112004>
- [101] O. Koroleva, L. Shabunina, and V. Bykov, “Structure of borosilicate glass according to Raman spectroscopy data,” *Glass and Ceramics*, vol. 67, no. 11-12, pp. 340–342, 2011. [Online]. Available: <http://dx.doi.org/10.1007/s10717-011-9293-0>
- [102] Monika, M. Falconieri, S. Baccaro, G. Sharma, K. S. Thind, and D. P. Singh, “Role of aluminium oxide in the structure of heavy metal oxide borosilicate glasses,” *Physica Status Solidi (A)*, vol. 209, no. 8, pp. 1438–1444, 2012. [Online]. Available: <http://dx.doi.org/10.1002/pssa.201228027>
- [103] Schott. Product properties, borofloat. Accessed 6.01.2014. [Online]. Available: <http://www.schott.com/borofloat/german/attribute/index.html>
- [104] S. V. Raman, “The effect of mixed modifiers on nuclear waste glass processing, leaching, and Raman spectra,” *Journal of Materials Research*, vol. 13, pp. 8–15, 1998. [Online]. Available: <http://dx.doi.org/10.1557/JMR.1998.0002>
- [105] T. Hupprich, “Raman-spektroskopische Untersuchungen an Alkali- und Erdalkalisilicatgläsern bei hohen temperaturen,” Ph.D. dissertation, Johannes Gutenberg-Universität, 2001. [Online]. Available: <http://archimed.uni-mainz.de/pub/2001/0028/>
- [106] Corning. (2014) Material information, Eagle XG. Accessed 6.01.2014. [Online]. Available: <http://www.corning.com/displaytechnologies/en/products/eaglexg/index.aspx>
- [107] Saint-Gobain. Glass properties, glazing manual. Accessed 6.01.2014. [Online]. Available: <http://nordic.saint-gobain-glass.com/b2c/default.asp>, <http://www.saint-gobain-sekurit.com/glazingcatalouge/glass-properties>
- [108] E. Irene, “SiO₂ based MOSFETS: Film growth and Si-SiO₂ interface properties,” in *High Dielectric Constant Materials*, ser. Springer Series in Advanced Microelectronics, H. Huff and D. Gilmer, Eds. Springer Berlin Heidelberg, 2005, vol. 16, pp. 45–90. [Online]. Available: http://dx.doi.org/10.1007/3-540-26462-0_3
- [109] A. Ben-Yakar and R. L. Byer, “Femtosecond laser ablation properties of borosilicate glass,” *Journal of Applied Physics*, vol. 96, no. 9, pp. 5316–5323, 2004. [Online]. Available: <http://dx.doi.org/10.1063/1.1787145>

- [110] M. Brown and C. Arnold, “Fundamentals of laser-material interaction and application to multiscale surface modification,” in *Laser Precision Microfabrication*, ser. Springer Series in Materials Science, K. Sugioka, M. Meunier, and A. Piqué, Eds. Springer Berlin Heidelberg, 2010, vol. 135, pp. 91–120. [Online]. Available: http://dx.doi.org/10.1007/978-3-642-10523-4_4
- [111] H. Helvajian, “Process control in laser material processing for the micro and nanometer scale domains,” in *Laser Precision Microfabrication*, ser. Springer Series in Materials Science, K. Sugioka, M. Meunier, and A. Piqué, Eds. Springer Berlin Heidelberg, 2010, vol. 135, pp. 1–34. [Online]. Available: http://dx.doi.org/10.1007/978-3-642-10523-4_1
- [112] L. Lewis and D. Perez, “Theory and simulation of laser ablation—from basic mechanisms to applications,” in *Laser Precision Microfabrication*, ser. Springer Series in Materials Science, K. Sugioka, M. Meunier, and A. Piqué, Eds. Springer Berlin Heidelberg, 2010, vol. 135, pp. 35–61. [Online]. Available: http://dx.doi.org/10.1007/978-3-642-10523-4_2
- [113] H. Niino, “Hybrid laser processing of transparent materials,” in *Laser Precision Microfabrication*, ser. Springer Series in Materials Science, K. Sugioka, M. Meunier, and A. Piqué, Eds. Springer Berlin Heidelberg, 2010, vol. 135, pp. 293–310. [Online]. Available: http://dx.doi.org/10.1007/978-3-642-10523-4_12
- [114] M. D. Perry, B. C. Stuart, P. S. Banks, M. D. Feit, V. Yanovsky, and A. M. Rubenchik, “Ultrashort-pulse laser machining of dielectric materials,” *Journal of Applied Physics*, vol. 85, no. 9, pp. 6803–6810, 1999. [Online]. Available: <http://dx.doi.org/10.1063/1.370197>
- [115] A. Ben-Yakar, A. Harkin, J. Ashmore, R. L. Byer, and H. A. Stone, “Thermal and fluid processes of a thin melt zone during femtosecond laser ablation of glass: the formation of rims by single laser pulses,” *Journal of Physics D: Applied Physics*, vol. 40, no. 5, p. 1447, 2007. [Online]. Available: <http://dx.doi.org/10.1088/0022-3727/40/5/021>
- [116] U. Eppelt, S. Russ, C. Hartmann, M. Sun, C. Siebert, and W. Schulz, “Diagnostic and simulation of ps-laser glass cutting,” in *ICALEO*, no. 31. Anaheim, California, USA: LIA, 2012. [Online]. Available: <http://publica.fraunhofer.de/documents/N-221410.html>
- [117] B. Struve, *Einführung in die Lasertechnik*. VDE, 2009.
- [118] J. Chan, T. Huser, S. Risbud, and D. Krol, “Modification of the fused silica glass network associated with waveguide fabrication using femtosecond laser

- pulses,” *Applied Physics A*, vol. 76, no. 3, pp. 367–372, 2003. [Online]. Available: <http://dx.doi.org/10.1007/s00339-002-1822-9>
- [119] K. Chakanga, O. Siepmann, K. von Maydell, and C. Agert, “Simulation and experimental validation of superposition scattering structures for efficient light trapping in thin film silicon solar cells,” in *PVSEC*, no. 28, Paris, France, 2013, pp. 2684–2688. [Online]. Available: <http://dx.doi.org/10.4229/28thEUPVSEC2013-3DV.1.32>
- [120] S. Quan, J. Hong-Bing, L. Yi, Z. Yong-Heng, Y. Hong, and G. Qi-Huang, “Relaxation of dense electron plasma induced by femtosecond laser in dielectric materials,” *Chinese Physics Letters*, vol. 23, no. 1, p. 189, 2006. [Online]. Available: <http://stacks.iop.org/0256-307X/23/i=1/a=055>
- [121] L. Jiang and H.-L. Tsai, “A plasma model combined with an improved two-temperature equation for ultrafast laser ablation of dielectrics,” *Journal of Applied Physics*, vol. 104, no. 9, p. 093101, 2008. [Online]. Available: <http://dx.doi.org/10.1063/1.3006129>
- [122] M. Sun, U. Eppelt, S. Russ, C. Hartmann, C. Siebert, J. Zhu, and W. Schulz, “Laser ablation mechanism of transparent dielectrics with picosecond laser pulses,” in *Proc. SPIE*, vol. 8530, 2012, pp. 853 007–853 007–10. [Online]. Available: <http://dx.doi.org/10.1117/12.976062>
- [123] N. G. Semaltianos, W. Perrie, V. Vishnyakov, R. Murray, C. J. Williams, S. P. Edwardson, G. Dearden, P. French, M. Sharp, S. Logothetidis, and K. G. Watkins, “Nanoparticle formation by the debris produced by femtosecond laser ablation of silicon in ambient air,” *Materials Letters*, vol. 62, no. 14, pp. 2165–2170, 2008. [Online]. Available: <http://dx.doi.org/10.1016/j.matlet.2007.11.087>
- [124] A. Ben-Yakar, R. L. Byer, A. Harkin, J. Ashmore, H. A. Stone, M. Shen, and E. Mazur, “Morphology of femtosecond-laser-ablated borosilicate glass surfaces,” *Applied Physics Letters*, vol. 83, no. 15, pp. 3030–3032, 2003. [Online]. Available: <http://dx.doi.org/10.1063/1.1619560>
- [125] J. Tamayo and R. Garcia, F.a, “Effects of elastic and inelastic interactions on phase contrast images in tapping-mode scanning force microscopy,” *Applied Physics Letters*, vol. 71, no. 16, pp. 2394–2396, 1997. [Online]. Available: <http://dx.doi.org/10.1063/1.120039>
- [126] H.-S. Ahn, S. Chizhik, A. Dubravin, V. Kazachenko, and V. Popov, “Application of phase contrast imaging atomic force microscopy to tribofilms on DLC

- coatings,” *Wear*, vol. 249, no. 7, pp. 617–625, 2001. [Online]. Available: [http://dx.doi.org/10.1016/S0043-1648\(01\)00694-9](http://dx.doi.org/10.1016/S0043-1648(01)00694-9)
- [127] J. B. Lonzaga, S. M. Avanesyan, S. C. Langford, and J. T. Dickinson, “Color center formation in soda-lime glass with femtosecond laser pulses,” *Journal of Applied Physics*, vol. 94, no. 7, pp. 4332–4340, 2003. [Online]. Available: <http://dx.doi.org/10.1063/1.1603962>
- [128] E. Hecht, *Optik*. München: Oldenbourg, 2009.
- [129] K. Mishchik, A. Ferrer, A. R. de la Cruz, A. Mermillod-Blondin, C. Mauclair, Y. Ouerdane, A. Boukenter, J. Solis, and R. Stoian, “Photoinscription domains for ultrafast laser writing of refractive index changes in BK7 borosilicate crown optical glass,” *Optical Materials Express*, vol. 3, no. 1, pp. 67–85, Jan 2013. [Online]. Available: <http://dx.doi.org/10.1364/OME.3.000067>
- [130] D. Wortmann, M. Ramme, and J. Gottmann, “Refractive index modification using fs-laser double pulses,” *Optics Express*, vol. 15, no. 16, pp. 10 149–10 153, 2007. [Online]. Available: <http://dx.doi.org/10.1364/oe.15.010149>
- [131] A. Streltsov, J. Dickinson, R. Grzybowski, D. Harvey, S. Logunov, A. Ozturk, J. Sutherland, and M. Potuzak, “Laser texturing of doped borosilicate glasses,” in *Proc. SPIE*, vol. 7584, San Francisco, California, USA, 2010, pp. 75 840S–75 840S–12. [Online]. Available: <http://dx.doi.org/10.1117/12.840689>
- [132] A. Taflove and S. Hagness, *Computational Electrodynamics: The Finite-Difference Time-Domain Method*. Artech House, 2005.
- [133] J. Lacombe, O. Sergeev, K. Chakanga, K. von Maydell, and C. Agert, “Three dimensional optical modeling of amorphous silicon thin film solar cells using the finite-difference time-domain method including real randomly surface topographies,” *Journal of Applied Physics*, vol. 110, no. 2, p. 023102, 2011. [Online]. Available: <http://dx.doi.org/10.1063/1.3610516>
- [134] C. Walder, “Effiziente optische modellierung von silizium-dünnschicht-solarzellenkombination von transfer-matrix-methode und strahlverfolgungsalgorithmus basierend auf dem integralen haze,” Master’s thesis, Carl-von-Ossietszky University Oldenburg, 2011.
- [135] M. H. Bhat, I. Peral, J. R. Copley, and C. A. Angell, “The boson peak in melt-formed and damage-formed glasses: A defect signature?” *Journal of Non-Crystalline Solids*, vol. 352, no. 42, pp. 4517–4524, 2006. [Online]. Available: <http://dx.doi.org/10.1016/j.jnoncrysol.2006.03.119>

- [136] A. I. Chumakov, G. Monaco, A. Monaco, W. A. Crichton, A. Bosak, R. Ruffer, A. Meyer, F. Kargl, L. Comez, D. Fioretto, H. Giefers, S. Roitsch, G. Wortmann, M. H. Manghnani, A. Hushur, Q. Williams, J. Balogh, K. Parliński, P. Jochym, and P. Piekarczyk, "Equivalence of the boson peak in glasses to the transverse acoustic van hove singularity in crystals," *Physical Review Letters*, vol. 106, p. 225501, May 2011. [Online]. Available: <http://dx.doi.org/10.1103/PhysRevLett.106.225501>
- [137] T. Chuvaeva, O. Dymshits, V. Petrov, M. Tsenter, A. Shashkin, A. Zhilin, and V. Golubkov, "Low-frequency Raman scattering of magnesium aluminosilicate glasses and glass-ceramics," *Journal of Non-Crystalline Solids*, vol. 282, no. 2, pp. 306–316, 2001. [Online]. Available: [http://dx.doi.org/10.1016/S0022-3093\(01\)00314-3](http://dx.doi.org/10.1016/S0022-3093(01)00314-3)
- [138] B. Mantisi, S. Adichtchev, S. Sirotkin, L. Rafaely, L. Wondraczek, H. Behrens, C. Marcenat, N. V. Surovtsev, A. Pillonnet, E. Duval, B. Champagnon, and A. Mermet, "Non-debye normalization of the glass vibrational density of states in mildly densified silicate glasses," *Journal of Physics: Condensed Matter*, vol. 22, no. 2, p. 025402, 2010. [Online]. Available: <http://stacks.iop.org/0953-8984/22/i=2/a=025402>
- [139] H. Shintani and H. Tanaka, "Universal link between the boson peak and transverse phonons in glass," *Nature Materials*, vol. 7, no. 11, pp. 870–877, Nov. 2008. [Online]. Available: <http://dx.doi.org/10.1038/nmat2293>
- [140] F. L. Galeener, A. J. Leadbetter, and M. W. Stringfellow, "Comparison of the neutron, Raman, and infrared vibrational spectra of vitreous SiO₂, GeO₂, and BeF₂," *Physical Review B*, vol. 27, pp. 1052–1078, 1983. [Online]. Available: <http://link.aps.org/doi/10.1103/PhysRevB.27.1052>
- [141] S. P. Best, R. J. H. Clark, C. L. Hayward, and R. Withnall, "Polarized single-crystal Raman spectroscopy of danburite, CaB₂Si₂O₈," *Journal of Raman Spectroscopy*, vol. 25, no. 7-8, pp. 557–563, 1994. [Online]. Available: <http://dx.doi.org/10.1002/jrs.1250250717>
- [142] C. Gautam, A. Yada, V. Mishra, and K. Vikram, "Synthesis, IR and Raman spectroscopic studies of (Ba,Sr)TiO₃ borosilicate glasses with addition of La₂O₃," *Open Journal of Inorganic Non-metallic Materials*, vol. 2, no. 4, pp. 47–54, 2012. [Online]. Available: <http://dx.doi:10.4236/ojinm.2012.24005>
- [143] B. Dwivedi and B. Khanna, "Cation dependence of Raman scattering in alkali borate glasses," *Journal of Physics and Chemistry of Solids*, vol. 56, no. 1, pp. 39–49, 1995. [Online]. Available: [http://dx.doi.org/10.1016/0022-3697\(94\)00130-8](http://dx.doi.org/10.1016/0022-3697(94)00130-8)

- [144] A. Mermet, N. V. Surovtsev, E. Duval, J. F. Jal, J. Dupuy-Philon, and A. J. Dianoux, "Inelastic neutron and Raman scattering of poly(methyl methacrylate): Nanostructure of polymer glasses," *Europhysics Letters*, vol. 36, no. 4, p. 277, 1996. [Online]. Available: <http://dx.doi.org/10.1209/epl/i1996-00222-0>
- [145] IUPAC, *IUPAC. Compendium of Chemical Terminology*, second edition ed., ser. the "Gold Book". Blackwell Scientific Publications, Oxford, 2006. [Online]. Available: <http://dx.doi.org/10.1351/goldbook>
- [146] F. A. Seifert, B. O. Mysen, and D. Virgo, "Three-dimensional network structure of quenched melts (glass) in the systems $\text{SiO}_2\text{-NaAlO}_2$, $\text{SiO}_2\text{-CaAlO}_4$ and $\text{SiO}_2\text{-MgAl}_2\text{O}_4$," *American Mineralogist*, vol. 67, no. 7-8, pp. 696–717, 1982. [Online]. Available: <http://ammin.geoscienceworld.org/content/67/7-8/696.short>
- [147] B. O. Mysen, L. W. Finger, D. Virgo, and F. A. Seifert, "Curve-fitting of Raman spectra of silicate glasses," *American Mineralogist*, vol. 67, no. 7-8, pp. 686–695, 1982. [Online]. Available: <http://ammin.geoscienceworld.org/content/67/7-8/686.short>
- [148] T. Furukawa and W. B. White, "Raman spectroscopy of heat-treated $\text{B}_2\text{O}_3\text{-SiO}_2$ glasses," *Journal of the American Ceramic Society*, vol. 64, no. 8, pp. 443–447, 1981. [Online]. Available: <http://dx.doi.org/10.1111/j.1151-2916.1981.tb09893.x>
- [149] D. Manara, A. Grandjean, and D. Neuville, "Advances in understanding the structure of borosilicate glasses: A Raman spectroscopy study," *American Mineralogist*, vol. 94, no. 5-6, pp. 777–784, 2009. [Online]. Available: <http://dx.doi.org/10.2138/am.2009.3027>
- [150] M. Dussauze, V. Rodriguez, A. Lipovskii, M. Petrov, C. Smith, K. Richardson, T. Cardinal, E. Fargin, and E. I. Kamitsos, "How does thermal poling affect the structure of soda-lime glass?" *The Journal of Physical Chemistry C*, vol. 114, no. 29, pp. 12 754–12 759, 2010. [Online]. Available: <http://dx.doi.org/10.1021/jp1033905>
- [151] D. Neuville and L. Cormier, "Structure of $\text{Na}_2\text{O-CaO-Al}_2\text{O}_3\text{-SiO}_2$ glasses using Raman spectroscopy," in *Proc. Glass Odyssey*, no. 6, Montpellier, France, 02-06. June, 2002.
- [152] W. Konijnendijk and J. Stevels, "The structure of borosilicate glasses studied by Raman scattering," *Journal of Non-Crystalline Solids*, vol. 20, no. 2, pp. 193–224, 1976. [Online]. Available: [http://dx.doi.org/10.1016/0022-3093\(76\)90132-0](http://dx.doi.org/10.1016/0022-3093(76)90132-0)
- [153] H. Li, P. Hrma, J. D. Vienna, M. Qian, Y. Su, and D. E. Smith, "Effects of Al_2O_3 , B_2O_3 , Na_2O , and SiO_2 on nepheline formation in borosilicate glasses: chemical and

- physical correlation,” *Journal of Non-Crystalline Solids*, vol. 331, no. 1, pp. 202–216, 2003. [Online]. Available: <http://dx.doi.org/10.1016/j.jnoncrysol.2003.08.082>
- [154] A. Osipov and L. Osipova, “Structure of glasses and melts in the $\text{Na}_2\text{O}-\text{B}_2\text{O}_3$ system from high-temperature Raman spectroscopic data: I. influence of temperature on the local structure of glasses and melts,” *Glass Physics and Chemistry*, vol. 35, no. 2, pp. 121–131, 2009. [Online]. Available: <http://dx.doi.org/10.1134/S1087659609020011>
- [155] L. Cormier, O. Majérus, D. R. Neuville, and G. Calas, “Temperature-induced structural modifications between alkali borate glasses and melts,” *Journal of the American Ceramic Society*, vol. 89, no. 1, pp. 13–19, 2006. [Online]. Available: <http://dx.doi.org/10.1111/j.1551-2916.2005.00657.x>
- [156] P. McMillan, “Structural studies of silicate glasses and melts-applications and limitations of Raman spectroscopy,” *American Mineralogist*, vol. 69, no. 7-8, pp. 622–644, 1984. [Online]. Available: <http://ammin.geoscienceworld.org/content/69/7-8/622.short>
- [157] C. S. Baidoc, “Study of some structural and physical properties of some B_2O_3 based glasses containing Ag_2O and 3D ions,” Ph.D. dissertation, Babeş-Bolyai University, 2011. [Online]. Available: http://doctorat.ubbcluj.ro/sustinerea_publica/rezumat/2012/fizica/Baidoc_Sergiu_En.pdf
- [158] C. Gautam, A. K. Yadav, and A. K. Singh, “A review on infrared spectroscopy of borate glasses with effects of different additives,” *ISRN Ceramics*, vol. 2012, no. 428497, p. 17, 2012. [Online]. Available: <http://dx.doi.org/10.5402/2012/428497>
- [159] E. I. Kamitsos, M. A. Karakassides, and G. D. Chryssikos, “Vibrational spectra of magnesium-sodium-borate glasses. 2. Raman and mid-infrared investigation of the network structure,” *The Journal of Physical Chemistry*, vol. 91, no. 5, pp. 1073–1079, 1987. [Online]. Available: <http://dx.doi.org/10.1021/j100289a014>
- [160] D. Maniu, I. Ardelean, T. Iliescu, S. Cinta, and O. Cozar, “Raman spectroscopic investigations of the oxide glass system $(1-x)(3\text{B}_2\text{O}_3 \cdot \text{K}_2\text{O})x\text{MO}$ ($\text{MO}=\text{V}_2\text{O}_5$ or CuO),” *Journal of Molecular Structure*, vol. 410-411, no. 0, pp. 291–294, 1997, molecular Spectroscopy and Molecular Structure 1996. [Online]. Available: [http://dx.doi.org/10.1016/S0022-2860\(96\)09674-3](http://dx.doi.org/10.1016/S0022-2860(96)09674-3)
- [161] G. Padmaja and P. Kistaiah, “Infrared and Raman spectroscopic studies on alkali borate glasses: Evidence of mixed alkali effect,” *The Journal of Physical Chemistry A*, vol. 113, no. 11, pp. 2397–2404, 2009, pMID: 19235995. [Online]. Available: <http://dx.doi.org/10.1021/jp809318e>

- [162] C. N. Santos, D. De Sousa Meneses, P. Echegut, D. R. Neuville, A. C. Hernandez, and A. Ibanez, “Structural, dielectric, and optical properties of yttrium calcium borate glasses,” *Applied Physics Letters*, vol. 94, no. 15, p. 151901, 2009. [Online]. Available: <http://dx.doi.org/10.1063/1.3115796>
- [163] A. de Pablos-Martín, D. Ristic, S. Bhattacharyya, T. Höche, G. Mather, M. O. Ramírez, S. Soria, M. Ferrari, G. Righini, L. Bausá, A. Durán, and M. Pascual, “Effects of TmF_3 additions on the crystallization of LaF_3 nanocrystals in oxyfluoride glasses: Optical characterization and up-conversion,” *Journal of the American Ceramic Society*, vol. 96, no. 2, pp. 447–457, 2013. [Online]. Available: <http://dx.doi.org/10.1111/jace.12120>
- [164] G. Özen, A. Aydinli, S. Cenk, and A. Sennaroglu, “Effect of composition on the spontaneous emission probabilities, stimulated emission cross-sections and local environment of Tm^{3+} in $\text{TeO}_2\text{-WO}_3$ glass,” *Journal of Luminescence*, vol. 101, no. 4, pp. 293–306, 2003. [Online]. Available: [http://dx.doi.org/10.1016/S0022-2313\(02\)00572-0](http://dx.doi.org/10.1016/S0022-2313(02)00572-0)
- [165] P. F. McMillan and R. L. Remmele, “Hydroxyl sites in SiO_2 glass; a note on infrared and Raman spectra,” *American Mineralogist*, vol. 71, no. 5-6, pp. 772–778, 1986. [Online]. Available: <http://ammin.geoscienceworld.org/content/71/5-6/772.short>
- [166] A. M. Efimov and V. G. Pogareva, “IR absorption spectra of vitreous silica and silicate glasses: The nature of bands in the 1300 to 5000 cm^{-1} region,” *Chemical Geology*, vol. 229, no. 1, pp. 198–217, 2006, physics, Chemistry and Rheology of Silicate Melts and Glasses. [Online]. Available: <http://dx.doi.org/10.1016/j.chemgeo.2006.01.022>
- [167] P. McMillan, “A Raman spectroscopic study of glasses in the system CaO-MgO-SiO_2 ,” *American Mineralogist*, vol. 69, no. 7-8, pp. 645–659, 1984. [Online]. Available: <http://ammin.geoscienceworld.org/content/69/7-8/645.short>
- [168] T. Furukawa, K. E. Fox, and W. B. White, “Raman spectroscopic investigation of the structure of silicate glasses. III. Raman intensities and structural units in sodium silicate glasses,” *The Journal of Chemical Physics*, vol. 75, no. 7, pp. 3226–3237, 1981. [Online]. Available: <http://dx.doi.org/10.1063/1.442472>
- [169] X. Q. Yan, W. J. Li, T. Goto, and M. W. Chen, “Raman spectroscopy of pressure-induced amorphous boron carbide,” *Applied Physics Letters*, vol. 88, no. 13, p. 131905, 2006. [Online]. Available: <http://dx.doi.org/10.1063/1.2189826>
- [170] M. Berginski, J. Huepkes, W. Reetz, B. Rech, and M. Wutting, “Recent development on surface-textured ZnO:Al films prepared by sputtering for thin-film

- solar cell application,” *Thin Solid Films*, vol. 516, no. 17, pp. 5836–5841, 2008. [Online]. Available: <http://dx.doi.org/10.1016/j.tsf.2007.10.029>
- [171] A. Abdolazadeh Ziabari and S. M. Rozati, “Carrier transport and bandgap shift in n-type degenerate ZnO thin films: The effect of band edge nonparabolicity,” *Physica B: Condensed Matter*, vol. 407, no. 23, pp. 4512–4517, 2012. [Online]. Available: <http://dx.doi.org/10.1016/j.physb.2012.08.024>
- [172] K. Ellmer, A. Klein, and B. Rech, Eds., *Transparent Conductive Zinc Oxide*, ser. Springer Series in Materials Science. Springer Berlin Heidelberg, 2008, vol. 104. [Online]. Available: <http://dx.doi.org/10.1007/978-3-540-73612-7>
- [173] F. van de Pol, F. Blom, and T. Popma, “R.f. planar magnetron sputtered ZnO films i: Structural properties,” *Thin Solid Films*, vol. 204, no. 2, pp. 349–364, 1991. [Online]. Available: [http://dx.doi.org/10.1016/0040-6090\(91\)90074-8](http://dx.doi.org/10.1016/0040-6090(91)90074-8)
- [174] H. Geng, *Semiconductor Manufacturing Handbook*. McGraw Hill Professional, Access Engineering, 2005. [Online]. Available: http://accessengineeringlibrary.com/browse/semiconductor-manufacturing-handbook/p2000ccd499713_1001
- [175] M. Nie, “Growth and morphology evolution of semiconducting oxides and sulfides prepared by magnetron sputtering,” Ph.D. dissertation, Technische Universität Berlin, 2015. [Online]. Available: <https://opus4.kobv.de/opus4-tuberlin/frontdoor/index/index/docId/6142>
- [176] J. A. Venables, *Introduction to Surface and Thin Film Processes*. Cambridge University Press, 2000. [Online]. Available: <http://dx.doi.org/10.1017/CBO9780511755651>
- [177] P. Yu and M. Cardona, *Fundamentals of Semiconductors*, ser. Graduate Texts in Physics. Springer Berlin Heidelberg, 2010. [Online]. Available: <http://dx.doi.org/10.1007/978-3-642-00710-1>
- [178] O. Kluth, G. Schöpe, J. Hüpkes, C. Agashe, J. Müller, and B. Rech, “Modified Thornton model for magnetron sputtered zinc oxide: film structure and etching behaviour,” *Thin Solid Films*, vol. 442, no. 1, pp. 80–85, 2003. [Online]. Available: [http://dx.doi.org/10.1016/S0040-6090\(03\)00949-0](http://dx.doi.org/10.1016/S0040-6090(03)00949-0)
- [179] H. E. Swanson, U. States., and N. B. of Standards., *Standard x-ray diffraction powder patterns*. Washington, DC: U.S. Dept. of Commerce, National Bureau of Standards : For sale by the Supt. of Docs., U.S. G.P.O., 1953.
- [180] X. Jiang, C. L. Jia, and B. Szyszka, “Manufacture of specific structure of aluminum-doped zinc oxide films by patterning the substrate surface,” *Applied*

- Physics Letters*, vol. 80, no. 17, pp. 3090–3092, 2002. [Online]. Available: <http://dx.doi.org/10.1063/1.1473683>
- [181] N. Sommer, S. Götzendörfer, F. Köhler, M. Ziegner, and J. Hüpkas, “Influence of deposition conditions and substrate morphology on the electrical properties of sputtered ZnO:Al grown on texture-etched glass,” *Thin Solid Films*, vol. 568, no. 0, pp. 25–30, 2014. [Online]. Available: <http://dx.doi.org/10.1016/j.tsf.2014.07.045>
- [182] Ü. Özgür, Y. I. Alivov, C. Liu, A. Teke, M. A. Reshchikov, S. Doğan, V. Avrutin, S.-J. Cho, and H. Morkoç, “A comprehensive review of ZnO materials and devices,” *Journal of Applied Physics*, vol. 98, no. 4, p. 041301, 2005. [Online]. Available: <http://dx.doi.org/10.1063/1.1992666>
- [183] R. D. Shannon, “Revised effective ionic radii and systematic studies of interatomic distances in halides and chalcogenides,” *Acta Crystallographica Section A*, vol. 32, no. 5, pp. 751–767, Sep 1976. [Online]. Available: <http://dx.doi.org/10.1107/S0567739476001551>
- [184] A. Wells, *Structural Inorganic Chemistry*, 4th ed. Oxford: Clarendon Press, 1975.
- [185] X. F. Fan, H. D. Sun, Z. X. Shen, J.-L. Kuo, and Y. M. Lu, “A first-principle analysis on the phase stabilities, chemical bonds and band gaps of wurtzite structure A_xZn_{1-x} alloys ($A = Ca, Cd, Mg$),” *Journal of Physics: Condensed Matter*, vol. 20, no. 23, p. 235221, 2008. [Online]. Available: <http://dx.doi.org/10.1088/0953-8984/20/23/235221>
- [186] L. E. Sutton and M. R. Truter, Eds., *Molecular Structure by Diffraction Methods*, ser. SPR-Molecular Structure by Diffraction Methods. The Royal Society of Chemistry, 1978, vol. 6. [Online]. Available: <http://dx.doi.org/10.1039/9781847556790>
- [187] Z. L. Pei, C. Sun, M. H. Tan, J. Q. Xiao, D. H. Guan, R. F. Huang, and L. S. Wen, “Optical and electrical properties of direct-current magnetron sputtered ZnO:Al films,” *Journal of Applied Physics*, vol. 90, no. 7, pp. 3432–3436, 2001. [Online]. Available: <http://dx.doi.org/10.1063/1.1398070>
- [188] N. Kılınç, L. Arda, S. Öztürk, and Z. Z. Öztürk, “Structure and electrical properties of Mg-doped ZnO nanoparticles,” *Crystal Research and Technology*, vol. 45, no. 5, pp. 529–538, 2010. [Online]. Available: <http://dx.doi.org/10.1002/crat.200900662>
- [189] A. Stadler, “Transparent conducting oxides-an up-to-date overview,” *Materials*, vol. 5, no. 4, pp. 661–683, 2012. [Online]. Available: <http://dx.doi.org/10.3390/ma5040661>

- [190] T. Smy, S. Dew, and R. Joshi, "Modeling 3d effects of substrate topography on step coverage and film morphology of thin metal films," *Thin Solid Films*, vol. 415, no. 1, pp. 32–45, 2002. [Online]. Available: [http://dx.doi.org/10.1016/S0040-6090\(02\)00502-3](http://dx.doi.org/10.1016/S0040-6090(02)00502-3)
- [191] Q. Liping, C. Changchun, Y. Yintang, Y. Xinhai, and S. Chunlei, "Strain effects on band structure of wurtzite ZnO: a gga+u study," *Journal of Semiconductors*, vol. 35, no. 7, p. 073004, 2014. [Online]. Available: <http://stacks.iop.org/1674-4926/35/i=7/a=073004>
- [192] S. T. Tan, B. J. Chen, X. W. Sun, W. J. Fan, H. S. Kwok, X. H. Zhang, and S. J. Chua, "Blueshift of optical band gap in ZnO thin films grown by metal-organic chemical-vapor deposition," *Journal of Applied Physics*, vol. 98, no. 1, p. 013505, 2005. [Online]. Available: <http://dx.doi.org/10.1063/1.1940137>
- [193] K. Chakanga, O. Siepmann, O. Sergeev, S. Geißendörfer, K. von Maydell, and C. Agert, "Laser textured substrates for light in-coupling in thin-film solar cells," in *Proc. SPIE*, vol. 8967, 2014, pp. 89671C–89671C–11. [Online]. Available: <http://dx.doi.org/10.1117/12.2037830>
- [194] R.-E. Nowak, M. Vehse, O. Sergeev, T. Voss, M. Seyfried, K. von Maydell, and C. Agert, "ZnO nanorods with broadband antireflective properties for improved light management in silicon thin-film solar cells," *Advanced Optical Materials*, vol. 2, no. 1, pp. 94–99, 2014. [Online]. Available: <http://dx.doi.org/10.1002/adom.201300455>
- [195] L. P. Schuler, "Properties and characterisation of sputtered ZnO," Ph.D. dissertation, University of Canterbury. Electrical and Computer Engineering, 2008. [Online]. Available: <http://hdl.handle.net/10092/1900>
- [196] A. Klein, C. Körber, A. Wachau, F. Säuberlich, Y. Gassenbauer, S. Harvey, D. E. Proffit, and T. O. Mason, "Transparent conducting oxides for photovoltaics: Manipulation of fermi level, work function and energy band alignment," *Materials*, vol. 3, no. 11, pp. 4892–4914, 2010. [Online]. Available: <http://dx.doi.org/10.3390/ma3114892>
- [197] K. Chakanga, O. Siepmann, O. Sergeev, S. Geißendörfer, K. von Maydell, and C. Agert, "Laser textured substrates for light in-coupling in thin-film solar cells," *Journal of Photonics for Energy*, vol. 4, no. 1, p. 044598, 2014. [Online]. Available: <http://dx.doi.org/10.1117/1.JPE.4.044598>
- [198] R. Schropp and M. Zeman, *Amorphous and Microcrystalline Silicon Solar Cells:*

- Modeling, Materials and Device Technology*. Springer-Verlag, Berlin, 1998. [Online]. Available: <http://dx.doi.org/10.1007/978-1-4615-5631-2>
- [199] A. Mahdjoub and L. Zighed, “New designs for graded refractive index antireflection coatings,” *Thin Solid Films*, vol. 478, no. 1, pp. 299–304, 2005. [Online]. Available: <http://dx.doi.org/10.1016/j.tsf.2004.11.119>
- [200] S. Solntsev, O. Isabella, D. Caratelli, and M. Zeman, “Thin-film silicon solar cells on 1-D periodic gratings with nonconformal layers: Optical analysis,” *IEEE Journal of Photovoltaics*, vol. 3, no. 1, pp. 46–52, Jan. 2013. [Online]. Available: <http://dx.doi.org/10.1109/jphotov.2012.2220123>
- [201] A. Čampa, O. Isabella, R. van Erven, P. Peeters, H. Borg, J. Krč, M. Topič, and M. Zeman, “Optimal design of periodic surface texture for thin-film a-Si:H solar cells,” *Progress in Photovoltaics: Research and Applications*, vol. 18, no. 3, pp. 160–167, 2010. [Online]. Available: <http://dx.doi.org/10.1002/pip.940>
- [202] V. E. Ferry, M. A. Verschuuren, H. B. T. Li, E. Verhagen, R. J. Walters, R. I. Schropp, H. A. Atwater, and A. Polman, “Light trapping in ultrathin plasmonic solar cells,” *Optics Express*, vol. 18, no. S2, pp. A237–A245, 2010. [Online]. Available: <http://dx.doi.org/10.1364/OE.18.00A237>
- [203] M. Vaněček, J. Springer, A. Poruba, O. Kluth, T. Repmann, B. Rech, N. Wyrsh, J. Meier, and A. Shah, “Light trapping and optical losses in microcrystalline si and micromorph solar cells,” in *WCPEC*, vol. 2, no. 3, Osaka, Japan, 2003, pp. 1527–1532. [Online]. Available: <http://ieeexplore.ieee.org/stamp/stamp.jsp?tp=&arnumber=1306218&isnumber=28993>
- [204] J. Springer, A. Poruba, and M. Vaněček, “Improved three-dimensional optical model for thin-film silicon solar cells,” *Journal of Applied Physics*, vol. 96, no. 9, pp. 5329–5337, 2004. [Online]. Available: <http://dx.doi.org/10.1063/1.1784555>
- [205] K. Jäger, O. Isabella, L. Zhao, and M. Zeman, “Light scattering properties of surface-textured substrates,” *Physica Status Solidi (C)*, vol. 7, no. 3-4, pp. 945–948, 2010. [Online]. Available: <http://dx.doi.org/10.1002/pssc.200982695>
- [206] O. Madani Ghahfarokhi, K. Chakanga, S. Geißendörfer, O. Sergeev, K. von Maydell, and C. Agert, “DC-sputtered ZnO:Al as transparent conductive oxide for silicon heterojunction solar cells with $\mu\text{c-Si:H}$ emitter,” *Progress in Photovoltaics: Research and Applications*, pp. 1099–159X, 2014. [Online]. Available: <http://dx.doi.org/10.1002/pip.2570>

- [207] A. Janotti and C. G. Van de Walle, “Oxygen vacancies in ZnO,” *Applied Physics Letters*, vol. 87, no. 12, p. 122102, 2005. [Online]. Available: <http://dx.doi.org/10.1063/1.2053360>
- [208] R. Jaramillo and S. Ramanathan, “Kelvin force microscopy studies of work function of transparent conducting ZnO:Al electrodes synthesized under varying oxygen pressures,” *Solar Energy Materials and Solar Cells*, vol. 95, no. 2, pp. 602–605, 2011. [Online]. Available: <http://dx.doi.org/10.1016/j.solmat.2010.09.025>
- [209] M. Theuring, V. Steenhoff, S. Geißendörfer, M. Vehse, K. von Maydell, and C. Agert, “Laser perforated ultrathin metal films for transparent electrode applications,” *Optics Express*, vol. 23, no. 7, pp. A254–A262, 2015. [Online]. Available: <http://dx.doi.org/10.1364/OE.23.00A254>

List of publications

Journal articles

- [1] K. Chakanga, O. Siepmann, O. Sergeev, S. Geißendörfer, K. von Maydell, and C. Agert, “Laser textured substrates for light in-coupling in thin-film solar cells,” *Journal of Photonics for Energy*, vol. 4, no. 1, p. 044598, 2014. [Online]. Available: <http://dx.doi.org/10.1117/1.JPE.4.044598>
- [2] —, “Textured substrates for light in-coupling in thin-film solar cells,” *SPIE Newsroom*, vol. 8967, pp. 89 671C–89 671C–11, 2014. [Online]. Available: <http://dx.doi.org/10.1117/2.1201403.005357>
- [3] O. Madani Ghahfarokhi, K. Chakanga, S. Geißendörfer, O. Sergeev, K. von Maydell, and C. Agert, “DC-sputtered ZnO:Al as transparent conductive oxide for silicon heterojunction solar cells with $\mu\text{c-Si:H}$ emitter,” *Progress in Photovoltaics: Research and Applications*, vol. 23, no. 10, pp. 1340–1352, 2015. [Online]. Available: <http://dx.doi.org/10.1002/pip.2570>
- [4] H. Volkmer and K. Chakanga, “Enhancing resilience through energy efficiency: Experience from tajikistan,” *Boiling Point*, vol. 61, pp. 2 – 4, 2013. [Online]. Available: <http://www.hedon.info/BP61EnhancingEnergyEfficiencyInTajikistan>
- [5] A. D. Sio, K. Chakanga, O. Sergeev, K. von Maydell, J. Parisi, and E. von Hauff, “ITO-free inverted polymer solar cells with ZnO:Al cathodes and stable top anodes,” *Solar Energy Materials and Solar Cells*, vol. 98, no. 0, pp. 52 – 56, 2012. [Online]. Available: <http://www.sciencedirect.com/science/article/pii/S0927024811005800>
- [6] R.-E. Nowak, S. Geißendörfer, K. Chakanga, M. Juilfs, N. Reininghaus, M. Vehse, K. von Maydell, and C. Agert, “Optimizing folded silicon thin-film solar cells on ZnO honeycomb electrodes,” *IEEE Journal of Photovoltaics*, vol. 5, no. 2, pp. 479–486, March 2015. [Online]. Available: <http://dx.doi.org/10.1109/JPHOTOV.2014.2388079>
- [7] J. Lacombe, O. Sergeev, K. Chakanga, K. von Maydell, and C. Agert, “Three dimensional optical modeling of amorphous silicon thin film solar cells using the finite-difference time-domain method including real randomly surface topographies,” *Journal of Applied Physics*, vol. 110, no. 2, p. 023102, 2011. [Online]. Available: <http://dx.doi.org/10.1063/1.3610516>

Conference contributions

- [1] K. Chakanga, O. Siepmann, O. Sergeev, S. Geißendörfer, K. von Maydell, and C. Agert, “Laser textured substrates for light in-coupling in thin-film solar cells,” in *Proc. SPIE*, vol. 8967, 2014, pp. 89671C–89671C–11. [Online]. Available: <http://dx.doi.org/10.1117/12.2037830>
- [2] K. Chakanga, O. Siepmann, K. von Maydell, and C. Agert, “Simulation and experimental validation of superposition scattering structures for efficient light trapping in thin film silicon solar cells,” in *PVSEC*, no. 28, Paris, France, 2013, pp. 2684–2688. [Online]. Available: <http://dx.doi.org/10.4229/28thEUPVSEC2013-3DV.1.32>
- [3] K. Chakanga, J. Lacombe, K. von Maydell, and C. Agert., “Textured TCO for light-trapping in amorphous silicon thin film solar cells: Simulative approach,” in *DPG, Poster*, 2011.
- [4] K. Chakanga, J. Lacombe, K. von Maydell, and C. Agert, “Texturing of ZnO films on glass for use as a light-scattering layer in micromorphous silicon thin film solar cells,” in *DPG, Poster*, 2010.
- [5] O. Madani Ghahfarokhi, K. Chakanga, O. Sergeev, K. von Maydell, and C. Agert, “Investigation of AZO as TCO for heterojunction solar cells,” in *PVSEC*, no. 28, Paris, France, 2013, pp. 1928–1931. [Online]. Available: <http://dx.doi.org/10.4229/28thEUPVSEC2013-2DV.3.32>
- [6] J. Lacombe, K. Chakanga, S. Geißendörfer, K. Von Maydell, and C. Agert, “Optical modeling of light trapping in thin film silicon solar cells using the FDTD method,” in *IEEE PVSC*, no. 35, 2010, pp. 001 535–001 539. [Online]. Available: <http://dx.doi.org/10.1109/PVSC.2010.5617030>
- [7] M. Theuring, J. Lacombe, K. Chakanga, R. Hünig, K. Huska, M. Vehse, K. von Maydell, U. Lemmer, and C. Agert, “Computational investigation of silicon thin film solar cells with grating structures fabricated by holographic lithography,” in *Proc. SPIE*, vol. 8438, 2012, pp. 84381Q–84381Q–8. [Online]. Available: <http://dx.doi.org/10.1117/12.921799>
- [8] J. Lacombe, O. Sergeev, K. Chakanga, K. von Maydell, and C. Agert, “Three dimensional optical modeling of amorphous thin film solar cells including real randomly surface topographies,” in *E-MRS*, 2011.
- [9] S. Geißendörfer, J. Lacombe, K. Chakanga, K. Von Maydell, and C. Agert, “2D-simulation amorpher und mikrokristalliner Silizium-Dünnschichtsolarzellen,” in *DPG, Poster*, 2011, pp. 001 535–001 539.

- [10] W. Dewald, C. Feser, R. Nowak, K. Chakanga, O. Sergeev, V. Sittinger, and K. v. Maydell, “Light trapping in a-Si:H/ μ c-Si:H tandem solar cells on differently textured TCOs,” in *PVSEC*, 2012. [Online]. Available: <http://dx.doi.org/10.4229/27thEUPVSEC2012-3DV.2.42>

Acknowledgements

This thesis would not have been possible without supervision and help from colleagues, friends and family. Thank you

- Prof. Dr. Carsten Agert for the opportunity to conduct the research at Next-Energy
- Prof. Dr. Ulrich Teubner from the University of Applied Sciences Emden/Leer
- Professor Dr. Jürgen Parisi for making the collaboration with the EHF group possible
- Dr. Karsten von Maydell for the supervision, calmness and diplomatic manner of conflict management. Thank you for the tolerance and optimism throughout the stressful years.
- The German Federal Environmental Foundation (DBU) for funding the PhD project and for the possibility to be part of the organisation, which is committed to a sustainable future. I have met many wonderful and inspiring people through the organisation. In particular,
 - Dr. Maximilian Hempel for the supervision and uncomplicated solutions to all forms of problems, whether research based, financial or conflicts.
 - Dr. Hedda Schlegel-Starmann for the encouragement and assistance throughout the stipend time and possibility to be part of the alumni network.
 - Christina Bush and Heike Stock for the friendly, helpful and organised communication.
 - Alexandra Seibt and scholarship holders from numerous seminars with fruitful discussions and networking possibilities.
- PV group at Next-Energy
 - Oleg Seergev for SEM and EDX images
 - Nies Reininghaus, Stephan Geißendörfer, Martin Kellermann, Ulf Kirstein and Clemens Feser for recipes and deposition of solar cells
 - Peter Klement, Nies Reininghaus, Alex Neumüller, Regina Nowak, Cordula Walder, Volker Steenhoff, Stephan Geißendörfer, Ben Hanke, Ortwin Siepmann, Martin Vehse and Omid Ghahfarokhi Madani for proof reading various scientific publications.

ACKNOWLEDGEMENTS

- Peter Klement and Ulf Kirsten for the wonderful office atmosphere. I definitely “put a ring on it”.
- Gabrielle Janson, Antja Schweitzer, Kristina Borzutzki for always having time to listen to various concerns. I always enjoyed our serious first world problems discussions.
- Ortwin Siepman for the assistance with laser texturing, maintenance of the 3DMM laser-setup and relaxed manner of solving problems. Jens Sürig-Morieng for assistance and custom made solutions.
- Colleagues at Next-Energy in other departments for the harmonious working environment. Lidiya Komsiyiska, Carolina Nunes Kirchner and Jan grosse Austing from the Energy Storage Division for the constructive criticism and discussions about my work.
- Former Next-Energy colleague Jürgen Lacombe for the introduction to TCAD and assistance with simulations.
- EHF group members at the Carl-von-Ossietzky University of Oldenburg for the collaboration and assistance with various measurement techniques. Dr. Antonietta De Sio for collaboration and Peter Michalowski for the assistance with the XRD measurements.
- My family and friends for the support, in particular my parents Moses and Estella Chakanga for making my education possible.
- Last but not least, my husband Hauke Holst for the unconditional love, support, endurance and sacrifices on my behalf.

Erklärung

Hiermit erkläre ich, dass ich die vorliegende Dissertation selbstständig verfasst und nur die angegebenen Hilfsmittel benutzt habe. Die Arbeit wurde weder in ihrer Gesamtheit noch in Teilen einer anderen wissenschaftlichen Hochschule zur Begutachtung in einem Promotionsverfahren vorgelegt.

Unterschrift, Ort und Datum

Kambulakwao Chakanga

🏠 Herbartstrasse 14, 26122 Oldenburg

📞 (+49) 151 233 64 337 • 📠 (+49) 441 30 916 30

✉️ Kambulakwao.Chakanga@gmail.com • 🌐 KambulakwaoChakanga

Personal Details

Date of Birth 16.04.1983
Nationality Zambian
Marital Status Married

University Education

- 10.2010–12.2015 **Doctorate in the field of physics**
Carl von Ossietzky University of Oldenburg, Germany
NEXT ENERGY EWE Research Centre for Energy Technology e.V., Oldenburg
„Laser texturing glass substrates for light in-coupling in silicon thin-film solar cells“
Scholarship from the German Federal Environmental Foundation
Best Student Poster Award, SPIE Conference 2014, San Francisco, USA
- 07.2012–10.2012 Internship, GIZ, Poverty-Oriented Basic Energy Services, Eschborn
- 10.2010–03.2012 Doctorate prerequisites
- 10.2008–09.2010 **Master of Science Postgraduate Program Renewable Energy**
Carl von Ossietzky University of Oldenburg, Germany
NEXT ENERGY EWE Research Centre for Energy Technology e.V., Oldenburg
„Texturing ZnO:Al films on glass for the use as a light-scattering layer in micromorph silicon thin-film solar cells“
- 02.2009–04.2009 Internship, Energy & Meteosystems, Oldenburg
- 10.2005–09.2008 **Bachelor of Science Biology**
Carl von Ossietzky University of Oldenburg, Germany
„Is the primary visual cortex involved in non-sensory processes?“
STOM Scholarship from the University of Oldenburg
- 04.2005–09.2005 **German language test for admission to university**
Carl von Ossietzky University of Oldenburg
- 01.2004–01.2005 **Biology and Chemistry without degree**
University of Namibia

International Experience

- 01.2015–11.2015 Travelling: Scandinavia, Baltic States, Europe and South America
- 01.2003–01.2004 Au-pair, Dötlingen, Germany

School Education

- 01.1995–12.2002 Deutsche Höhere Privatschule (DHPS) Windhoek
- 01.1993–12.1994 Gammams Primary School, Windhoek, Namibia
- 01.1988–12.1992 Dola Hill Primary School, Ndola, Zambia